IMPROVED FIDELITY OF TRIANGULATION SENSOR MEASUREMENTS IN OPTICAL INSPECTION

by

MILAD HOSSEINPOUR

A dissertation submitted to the faculty of
The University of North Carolina at Charlotte
in partial fulfillment of the requirements
for the degree of Doctor of Philosophy in
Mechanical Engineering

Charlotte

2022

Approved by:

Dr. Edward P. Morse

Dr. Jimmie Miller

Dr. Wesley Williams

Dr. Robert Cox

ABSTRACT

MILAD HOSSEINPOUR. Improved Fidelity of Triangulation Sensor Measurements in Optical Inspection. (Under the direction of Dr. EDWARD P. MORSE)

With the evolution of gear design requirements for new applications, classical gear inspection based on a time-consuming line-oriented tactile measurement must be replaced with a more rapid, areal inspection that can capture complex modern gear modifications. Triangulation-based optical instruments provide a promising path to meet new gear metrology demands with respect to access to the gear flanks and having sufficient speed and accuracy. In triangulation sensor measurement, the image position of a laser line strip on the sensor is analyzed to find the measured geometry. This image of the line on the sensor is calculated through a peak detection algorithm that produces a 'ridge line,' which is the line in the x-y sensor domain with the highest light intensity.

The physics of optical measurement dictates that speckles and scattered light exist during an optical inspection. As a result, when a triangulation sensor is used, the deflection of the scattered light may cause inaccurate peak detection and, therefore, large form deviations in the reconstructed (measured) geometry. In addition, multiple light reflections that influence point calculations from an optical measurement must be detected, eliminated, or remedied. This research provides an improved mathematical approach to ridge line detection in each sensor frame, to detect the peak position of that frame even more accurately. This algorithm is used to measure four reference geometries to evaluate its influence on point clouds from surface measurements when compared to the embedded (OEM) algorithm.

This dissertation offers the improved profile fidelity of triangulation sensor measurements for optical inspection by developing a novel mathematical approach and replacing the original row-by-row peak detection algorithm by the proposed frame-by-frame algorithm. It can be used in the future closed-loop control process where the new gear production processes require fast-optical measurement and evaluation processes to trace back from the produced gear geometry to the manufacturing process. This can be achieved by equipping the manufacturing machine with suitable optical measuring devices, an appropriate evaluation strategy, and an inline inspection.

ACKNOWLEDGMENTS

First and foremost, I would like to express my deepest appreciation to Prof. Edward P. Morse for all his help, advice, and support over these five years. He is the one who encouraged me to pursue my Ph.D. at the University of North Carolina at Charlotte. He also introduced me to the field of metrology and later mentored me to become a researcher. Not only did he not leave me alone in an overwhelming situation when my previous advisor had to leave the college, but he also offered me an interesting research project. The project titled "Advanced Nanometer-class Coordinate Measuring Machine" or ANCMM, funded by NASA through the SBIR (Small Business Innovation Research) program. His broad vision, intelligence, and friendly personality have always inspired me. It is a tremendous honor to be one of his doctoral students. I also need to sincerely appreciate NASA and OptiPro Systems, the primary recipient of the funding, for having confidence in me and for supporting me over my permanent residency process.

I would love to thank Prof. F. Gert Goch, who motivated me to focus my research on gear metrology, specifically on developing a fast optical measurement of cylindrical gears. He trusted me by offering a two-year Nikon Corporation-funded industrial project. He also broadened my industrial perspective by assigning me various duties, including solving many complex measuring tasks requested from several regional industrial enterprises at the Siemens Large Scale Manufacturing Laboratory. Thanks to his consistent financial support from the Energy Production & Infrastructure Center, I could make impressive progress toward earning my Ph.D. I must thank Nikon Corporation at Tokyo, Japan support over the project, especially I value the insights and guidance Mr. Nakano Sumito provided.

I would like to express my appreciation to Prof. Jimmie Miller. From his lectures, I learned a lot about precision metrology, particularly the measurement of machine tools for evaluating and correcting geometric errors. He made the metrology principles more visible and understandable through laboratory experiments. I can never forget his dedication and support that are still going on during the current ANCMM project.

I thank Prof. Wesley Williams, who supported me indirectly while publishing a conference paper and directly during my permanent residency process at its most difficult time. I appreciate the opportunity to work with you on one part of the "Evaluation of a coaxial multi-stage magnetic gear" research project.

Special thanks go to Prof. Robert Cox, who kindly accepted to serve as the Graduate Faculty Representative.

I am sincerely thankful for the support from the American Gear Manufacturers Association (AGMA) through their scholarships for three academic years, which made a lot of opportunities possible for me in the past three years.

I am grateful to Dr. Yue Peng, who taught me how to operate the large Coordinate Measuring Instrument "Leitz PMMF" and a new 6-axes optical instrument "Nikon-HN3030" and how to work with the software platforms "Quindos" and "HN Metrology" running these measuring devices. Her efforts to educate the next generation of ME graduate students cannot be forgiven.

Center for Precision Metrology (CPM) and the Energy Production and Infrastructure Center (EPIC) at UNC Charlotte have my gratitude for providing a great environment, facilities, and financial support to promote precision metrology. My thanks and appreciation go to the current and previous MEES, EPIC, and CPM staff members, Mrs. Tracy Beauregard, Lori Brown, Jennifer Chastain, and Mr. Brian Dutterer.

Finally, I would love to say how grateful I am for my wonderful family's unwavering love and support during this difficult time, especially the past three years since my father's passing. Words are not enough to describe how inspiring they have been for me. Among thousands of their lessons, my lovely mom taught me the lessons of liberty, liberalism, and dedication to others. My dear dad taught me not to give up but to keep on. My beloved sister has been my role model throughout my education and simultaneously has always supported the family.

DEDICATION

To My Lovely Brave People and Their Meaningful Message

WOMAN LIFE FREEDOM

زن زندگی آزادی

CONTENTS

LIST OF TABLES

LIST OF FIGURES

NOMENCLATURE

X	X-axis of a Cartesian coordinate system
Y	Y-axis of a Cartesian coordinate system
Z	Z-axis of a Cartesian coordinate system
U	U axis of a curvilinear coordinate system
V	V axis of a curvilinear coordinate system
D	D axis of a curvilinear coordinate system
u	surface parametric coordinate of point P of the U axis
v	surface parametric coordinate of point P of the V axis
P_m	measured point of a gear feature
ρ_m	ρ coordinate of Pm in cylindrical coordinate system
φ_m	φ coordinate of Pm in cylindrical coordinate system
z_m	z coordinate of Pm in Cartesian coordinate system
ρ	radial distance from origin to the projection of point P on the X-Y plane
t	transverse
n	normal
r_b	base radius of the flank origin
$\emptyset_b$	polar angle of the origin
β_b	base helix angle
C	helix coefficient
$Ev\alpha$	involute function
α	pressure angle
α_t	transverse pressure angle at reference circle
ξ	roll angle of the involute
h	flank direction
P	a mathematical point
b	face width
L_α	profile evaluation length
L_β	helix evaluation length
β	helical angle at reference circle
η	space width half angle at reference circle
η_b	space width half angle of base circle

$\left\|\overrightarrow{d_{lot}}\right\|$	plump line distance
$\overrightarrow{d_{lot}}$	deviation vector in the surface normal direction
$\overrightarrow{d_{proj}}$	deviation vector projected to the surface normal direction, N
$\left\|\overrightarrow{d_{proj}}\right\|$	magnitude of the deviation vector $\overrightarrow{d_{proj}}$
d_{Euklid}	Euclidean distance
$C_{H\alpha}^{A}$	areal profile slope modification
$C_{H\beta}^{A}$	areal helix slope modification
C_{α}^{A}	areal profile crowning modification
C_{β}^{A}	areal helix crowning modification
$f_{H\alpha}^{A}$	areal profile slope deviation
$f_{H\beta}^{A}$	areal helix slope deviation
F_{pi}^{A}	areal individual cumulative pitch deviation
ff_mean	areal form deviation
p	p term index of 1D Chebyshev polynomial of variable x
q	term index of 1D Chebyshev polynomial of variable y
μm	micrometer
nm	nanometer
$X\text{-}Detector$	X-axis of a sensor coordinate system
$Y\text{-}Detector$	Y-axis of a sensor coordinate system
x	X coordinate of measured intensity on X-Detector
y	Y coordinate of measured intensity on Y-Detector
ξ	local coordinate on the ridge line
X_{loc}	X-axis of a local coordinate system on the ridge line
Y_{loc}	Y-axis of a local coordinate system on the ridge line
X_c	X coordinate of a measured intensity on the ridge line
Y_c	Y coordinate of a measured intensity on the ridge line
φ	rotational angle from X-Detector to X_{loc}
a_i	coefficients describing the ridge line profile in quadratic ridge line
b_i	coefficients describing the intensity distribution over each sensor row in quadratic ridge line

s_j	coefficients describing the ridge line profile (s_1, s_2, s_3, s_4) and coefficients describing the intensity distribution over each sensor row (s_5, s_6) or the solution of the iterative optimization $(\vec{s} = (s_1, s_2, s_3, s_4, s_5, s_6))$
$s_{j,0}$	initial optimization solution $(\overrightarrow{s_0} = \left(s_{1,0}, s_{2,0}, s_{3,0}, s_{4,0}, s_{5,0}, s_{6,0}\right)$
Δs_j	Solution change of the iterative optimization $(\overrightarrow{\Delta s} = (\Delta s_1, \Delta s_2, \Delta s_3, \Delta s_4, \Delta s_5, \Delta s_6))$
I_a	model-based intensity of a point on the sensor
I_m	measured intensity
d_i	residual between the measured and the model-based intensity for the ith measured intensity
Q	objective function
Q_k	objective function at the kth iteration
$f_{i,k}$	non-linear term in the nominators of the ith equation in the system of equations at the kth iteration
$g_{i,k}$	linearized $f_{i,k}$ with respect to $\Delta s_{i,k}$
A_{ij}	coefficients of Δs_j in the five linear equations
B_i	constant values in the five linear equations
C_k	constant vector in the rearranged five linear equations (= - $\overrightarrow{B_i}$) at the kth iteration
M_k	Matrix of A_{ij} coefficients at the kth iteration
$\overrightarrow{\Delta s_k}$	vector of solution changes at the kth iteration
Y_{UNCC}	modified Y-positions of the ridge line using UNCC optimization algorithm on the sensor coordinate
$Y_{fminsearch}$	modified Y-positions of the ridge line using the fminsearch MATLAB function on the sensor coordinate
M_i	a repeated term in the M_k matrix $(M_i = -y_i + a_0 + a_1 x_i + a_2 {x_i}^2)$ for the ith measured intensity
N_i	a repeated term in the M_k matrix $(N_i = I_{m,i} - (b_0 - b_2 {M_i}^2)$ for the ith measured intensity
n	total count of measured intensities

LIST OF ABREVIATIONS

CNC	Computer numerical control
GMI	Gear Measuring Instruments
CMM	Coordinate Measuring Machines
1D	One dimension
2D	Two-dimension
3D	Three-dimension
L#	Left flank number
R#	Right flank number
WES	Wind Energy Systems
NC	Numerically controlled
IFP	Interference fringe pattern
CCD	Charge-coupled device
CAD	Computer-aided design
UNCC	University of North Carolina at Charlotte
RMS	Root mean square
CSV	Comma separated value
CSY/CS	Coordinate System
ISO	International Organization for Standardization
VDI	Verein Deutscher Ingenieure

1 CHAPTER 1: INTRODUCTION

1.1 Motivation and background

Gears are the crucial elements of power transmission systems whose efficiency is determined by the quality of their gears. Gears have a wide range of applications, from wind energy applications to automotive industries. Over the past decades, the functional properties of transmission systems, including generated noise, vibration, transmission capacity, lifetime, and weight, have been enhanced dramatically due to improved gear geometry [1]. Many efforts have been made on different aspects of gear manufacturing from cutting to the finishing stage, to achieve more repeatable, reliable, and efficient techniques in precision gear manufacturing to meet quality grade requirements [2-5]. Precision gear manufacturing needs to accurately capture gear surface features. Advancements in gear design and manufacturing over the past few decades require more robust gear metrology in terms of reliability and evaluation speed with a higher accuracy level. Therefore, manufacturing precision gears requires precision metrology to control the gear geometry in size and shape. Before the 1970s, when CNC technology had not been invented for the metrology purpose, gear metrology had been performed by manual gauging and electro-mechanical instruments. However, CNC-based contact methods made a paradigm shift in gear metrology which are still state-of-the-art techniques with high accuracy dominating in the industry. In the design and manufacturing stage of many gear applications, the gear flank follows an involute profile that requires tight tolerancing in the range of single-digit micrometers [6]. Conventionally, gears are measured by Gear Measuring Instruments (GMI) or tactile Coordinate Measuring Machines (CMM) [1,7,8]. Although they are able to measure gear tooth shape with a micrometer level accuracy, the technology is limited in speed due to the tactile nature of the measurement. Basically, classical gear measurement is based on two characteristic lines on both flanks of only four teeth oriented approximately 90 degrees apart [9,24]. One is a profile line in a transverse plane, and the other is a lead line in a pitch cylinder. Clearly, two lines per flank only for a limited number of teeth cannot extensively represent the entire gear surface. Lotze et al. offered an analytical full 3D substitute gear model for helical and spur gears to use the measuring capability of Coordinate Measuring Machines (CMM) to be extended to gear evaluation [9]. They used three independent parameters, i.e., the base radius of the flank origin r_b, polar angle of the origin $\emptyset_b$, and base helix angle β_b to analytically model the nominal gear flank. Their work initiated the fundamentals of using CMM in gear inspection. In contrast with the conventional cross-section method, this method did not require capturing points exactly on a transverse plane for profile testing or pitch cylinder for lead testing as described in the standards. However, the points could be measured at any arbitrary coordinates. This gave remarkable flexibility and accuracy for the gear measurement and evaluation using a CMM. Flank modifications could also be added to the model using some additional geometrical parameters. However, gear deviation parameters were only limited to those of the predefined parameters in the mathematical model.

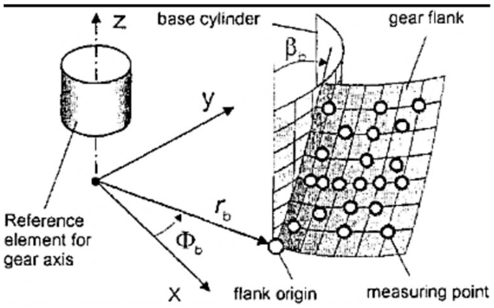

$$F(\alpha,\zeta)=\begin{pmatrix}x\\ y\\ z\end{pmatrix}=\begin{pmatrix} r_b\sec\alpha\cos[\varphi_{b0}+C\,\zeta-h\,Ev\alpha]\\ r_b\sec\alpha\sin[\varphi_{b0}+C\,\zeta-h\,Ev\alpha]\\ \zeta\end{pmatrix} \qquad (1)$$

with

$C=\tan(\beta_b)/r_b$	helix coefficient
$Ev(\alpha)=\tan(\alpha)-\alpha$	involute function
r_b	base radius
α, ζ	Gaussian surface parameters (pressure angle, axis co-ordinate)
h	flank direction ($h=\pm1$ for left- and right-hand flank)

Figure 1.1: Substitute gear flank and measuring points. Mathematical equation correlates nominal geometrical parameters with Cartesian coordinates [after 9]

In the high volume production of automotive gears, the environmental situation, including the temperature behavior of machine tools and tool wear affecting the precision of production, remains constant; therefore, a random sample seems to be a rational strategy to save inspection time [10]. Consequently, the time-consuming tactile measurement requires a random inspection, especially when it comes to the high volume production of mid-size gears.

In addition, geometrical modifications such as slope and crowning are intentionally added to the nominal involute of modern gear flanks in automotive and wind energy transmission systems to enhance their functionality in terms of generated noise, transmitted power, vibration, and lifetime [11]. On the other hand, there are some undesired deviations from the nominal involute which are an inevitable result of the manufacturing process. Those deviations include but are not limited to distortion and twist caused mainly by heat treatment process and continuous generating grinding [1]. However, the above-mentioned analytical model suffered from the lack of any parameters describing flank modifications and deviations which have seemed to be highly demanding and inevitable, especially over recent decades as the automotive industry and renewable energy are growing rapidly.

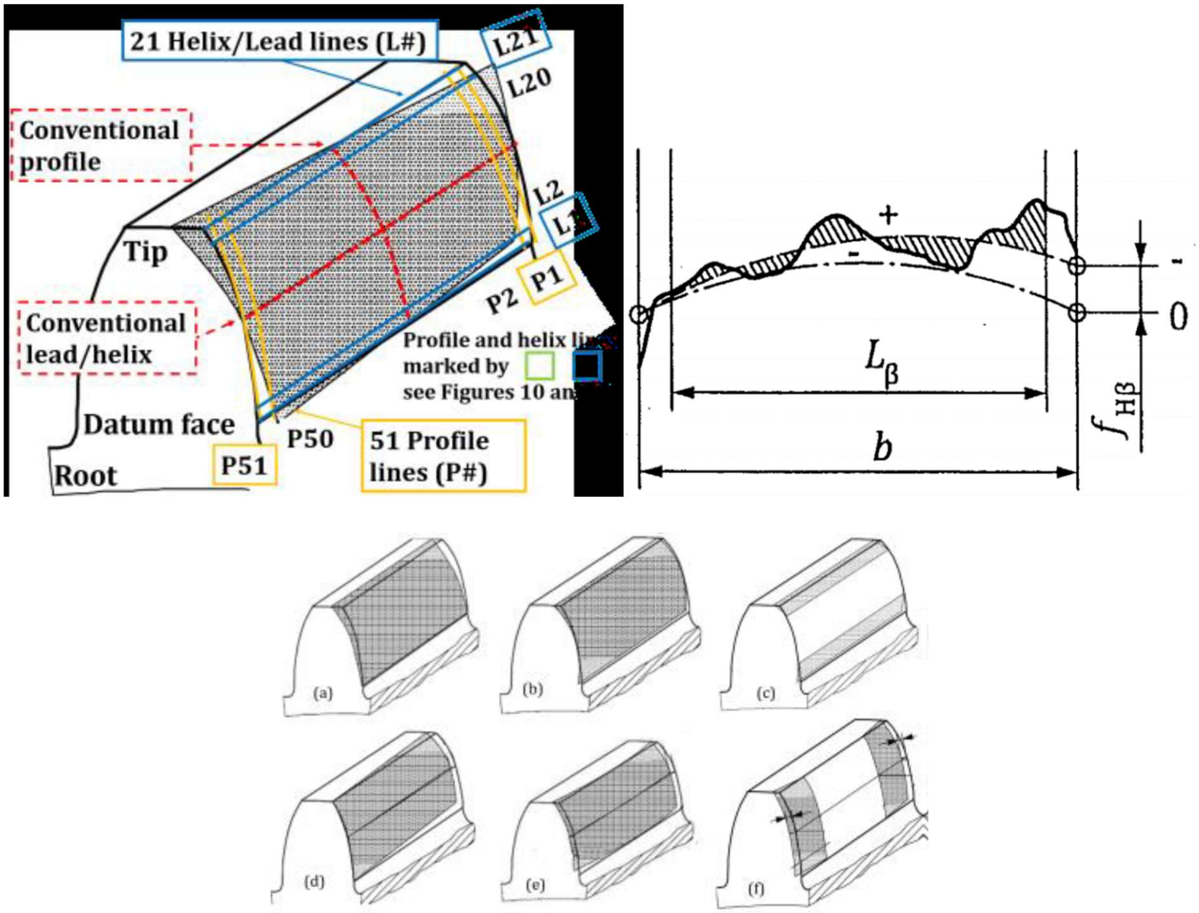

Figure 1.2: Gear flank with modification/deviation of involute helical gears [after 11, 12]
a) Profile slope b) Profile crowning c) Tip and root relief d) Lead slope e) Lead crowning f) End reliefs

However, those desired modifications and undesired deviations cannot be captured when a line-oriented approach is used in which a few lines represent the entire gear flank. All the above-mentioned reasons can support the argument that a comprehensive measurement is required to capture the 3D feature of gear flanks to feed the manufacturing section with holistic information about the measured gears. This can improve the assessment of the measured gears and the gear manufacturing process.

A set of explicit equations were introduced by Guenther et al. to add a nominal description of helical gear modifications to the nominal gear flank in 2D. The equations comprised profile slope modification, profile crowning modification, helix slope modification, and helix crowning modification [13]. During the initial gear manufacturing process, these deviations can intentionally be added to the gear flank to compensate later for the negative effect of undesired manufacturing deviations caused predominantly by the subsequent heat treatment process and continuous generating grinding [3]. Also, adding modifications in the finishing stage of manufacturing can provide a smooth meshing between mating gears under various loading conditions. The modifications can reduce stress concentration and, as a result, wear damage on the meshing area of mating gears leading to a substantial increase in the gear's lifetime. Mechanical components' fatigue life under dynamic loads is exponentially proportional to the applied load. The modification can play a promising role in specifically Wind Energy Systems (WES), where developing robust gearbox technology that requires relatively little maintenance is essential. Therefore, it seems crucial to qualitatively evaluate and control the desired modifications and undesired deviations to reach a sufficient quality level of manufactured gears and to control the manufacturing process as well.

Goch discussed the current challenges that modern numerically controlled (NC) measuring instruments encountered when the only available standards and guidelines were the conventional probing and evaluation along the prescribed cross-section lines [1]. Gear alignment and mounting were considered the first problem when a tactile probe was supposed to precisely scan the standardized profiles. A mechanical alignment together with a numerical compensation could only partially fulfill those requirements. Secondly, the non-contact optical devices could scan several tens of thousands points in a few seconds, reflecting helpful information of the flank topography; however, the lack of comprehensive standards covering the entire gear flank would waste the majority of the captured information. Unavoidable gear modifications, on the other hand, due to the growing demand for higher gear drives' functional properties, would require a significant change in the evaluation rules and conditions. Hence, he proposed a self-contained mathematical model of the flank surface, including a geometry description of nominal points along with their normal directions. This could remove the requirement of measuring points along specific profiles; instead, all the 3D measured points could be utilized in evaluating the gear. This model could also provide an iterative numerical alignment to reach a 3D coordinate transformation of the entire measured points to meet the conformance alignment requirements. Following the mentioned alignment and selecting the measured point clouds in a tight region along the conventional evaluation tracks, there would be an acceptable agreement between the new and traditional evaluation results. Given the mathematical model and normal unit vector of the nominal surface [13], he showed that the Plumb line distance is dependent on the actual coordinates of the gear flank. Thus, d_{lot} is independent of the position of the corresponding nominal point to any measured point, which is considered a significant advantage of this method. Due to its analytical nature, this method could also drive the deviation values at the presence of superimposed flank modifications. His work significantly contributed to areal evaluation methods in future gear metrology.

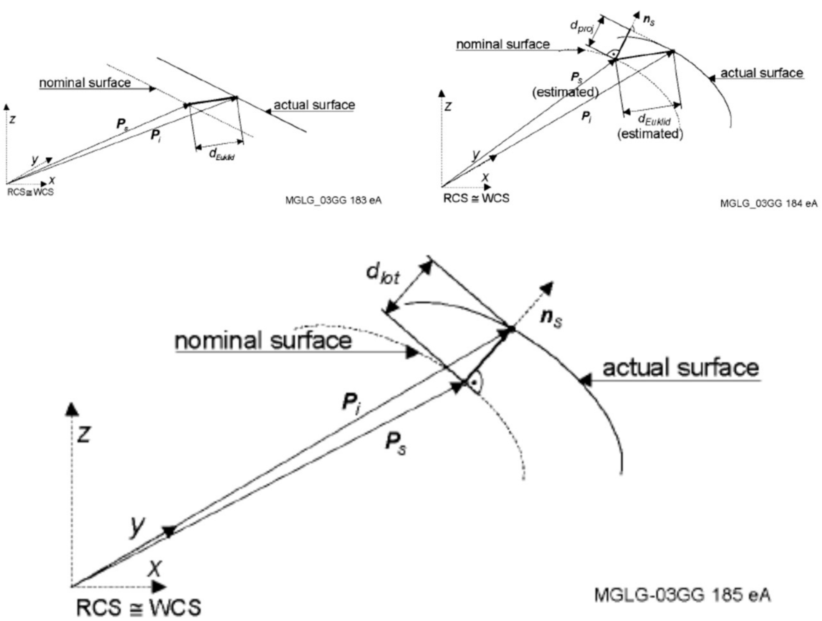

$$d_{lot} = \frac{r}{\left|n_{Evol}\right|} \cdot \left(\begin{array}{l} \sqrt{\frac{s_i^{\,2}}{r^2} - 1} - \operatorname{atan}\left(\sqrt{\frac{s_i^{\,2}}{r^2} - 1} \right) - \\ - \gamma_i + \eta_b + z_i \cdot \tan(\beta) / r_t \end{array} \right)$$

Figure 1.3: Three various deviations between the measured point and the nominal geometry [after 14, 15]
a) Euclidean distance d_{Euklid} b) Projected distance d_{Proj} c) Plumb line distance d_{lot}

Ni et al. dealt with current major challenges in gear metrology, including a lack of areal information of gear flank, complex flank modifications, and improved closed-loop control of the manufacturing process [12]. Following the prementioned Plumb line distance concept, they presented implicit equations describing a full 3D gear geometry for both sides of all gear teeth. An areal description of the flank surface named the areal distance map was defined independent of the nominal geometry of the flank containing all flank modifications and deviation parameters.

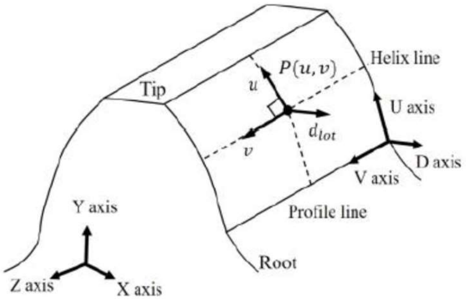

$$d_{\mathrm{lot}} = \frac{r_{\mathrm{b}}}{\sqrt{1+(\tan\alpha_{\mathrm{t}}\tan\beta)^2}}\left\{\sqrt{\frac{\rho_{\mathrm{m}}^2}{r_{\mathrm{b}}^2}-1}-\arctan\left(\sqrt{\frac{\rho_{\mathrm{m}}^2}{r_{\mathrm{b}}^2}-1}\right)-\varphi_{\mathrm{m}}+\frac{\pi}{2|z|}-\tan\alpha_{\mathrm{t}}+\alpha_{\mathrm{t}}+z_{\mathrm{m}}\frac{\tan\beta\cos\alpha_{\mathrm{t}}}{r_{\mathrm{b}}}\right\}$$

Figure 1.4: Local UV coordinates commensurate with the description of flank modifications
Plumb line distance equation for helical gears [after 12]

They proposed a meaningful revision to the conventional line-oriented standard parameters. Furthermore, using the orthogonal characteristics of Chebyshev polynomials, a robust evaluation method was proposed in which gear deviation parameters can directly be extracted from an areal distance map.

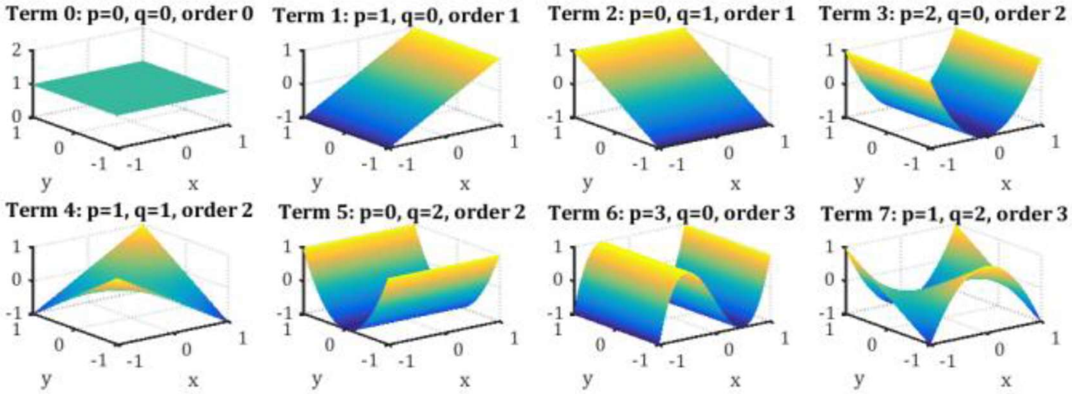
Term 0: p=0, q=0, order 0
Term 1: p=1, q=0, order 1
Term 2: p=0, q=1, order 1
Term 3: p=2, q=0, order 2
Term 4: p=1, q=1, order 2
Term 5: p=0, q=2, order 2
Term 6: p=3, q=0, order 3
Term 7: p=1, q=2, order 3

Figure 1.5: First eight terms of 2D Chebyshev polynomials [after 12]

They performed simulation techniques for various types of point distributions to obtain areal parameters out of simulated data points. Later, they successfully verified the evaluation method by measuring a gear artifact and comparing line-oriented with area-oriented parameters. The maximum relative deviation between the areal method and the conventional certified one was about 1.5 micrometers which was within the measurement uncertainty. The developed areal distance map initiated a fundamental change in gear evaluation algorithms in future studies and applications of gear metrology. It expanded a holistic gear assessment in the gear production industry.

As discussed earlier, a holistic measurement cannot be achieved in a reasonable time when the measurement technology is restricted to widely used tactile measurement. This deficiency highlights the emerging need for an essential shift in the measurement and inspection strategy for transmission gears. It is exactly where an alternative non-contact measurement approach can compensate for these drawbacks and introduce a fast assessment approach. A non-contact measurement can always be realized using an optical instrument; however, the measurement reliability is a challenging factor to agree with the required accuracy grade. Nonetheless, due to the high measurement speed and high-resolution measured point clouds, optical methods are becoming more of industrial interest for mass production.

1.2 Instrument Evaluation

A gear measuring instrument and an involute artifact are conventionally used to control the standard of quality gears. The standard calibration of the involute artifact, on the other hand, is insufficiently accurate. Takeoka et al. adopted a straightforward approach for measuring the involute artifact using a laser interferometer with a laser beam diameter of 6 µm and measurement resolution of 158 nm (a quarter of the laser wavelength) [16]. The impacts of the surface condition of the measured item and the influence of the driving of the artifact were addressed in the essential experiments shown in their proposed measuring device. It was verified that the suggested approach was capable of measuring the profile form deviation of an involute tooth flank and had the potential to measure an involute artifact with an ultraprecise level.

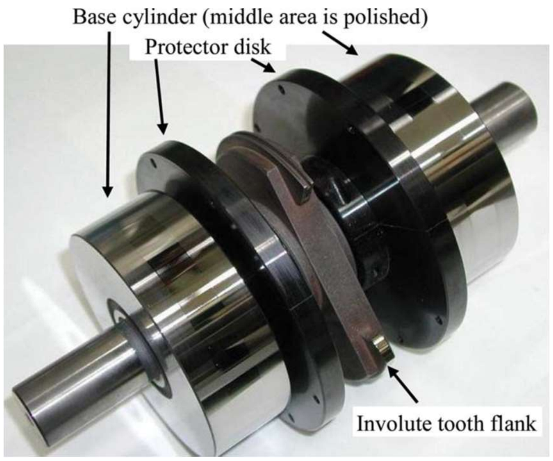

Figure 1.6: Involute artifact with base cylinder [after 16]

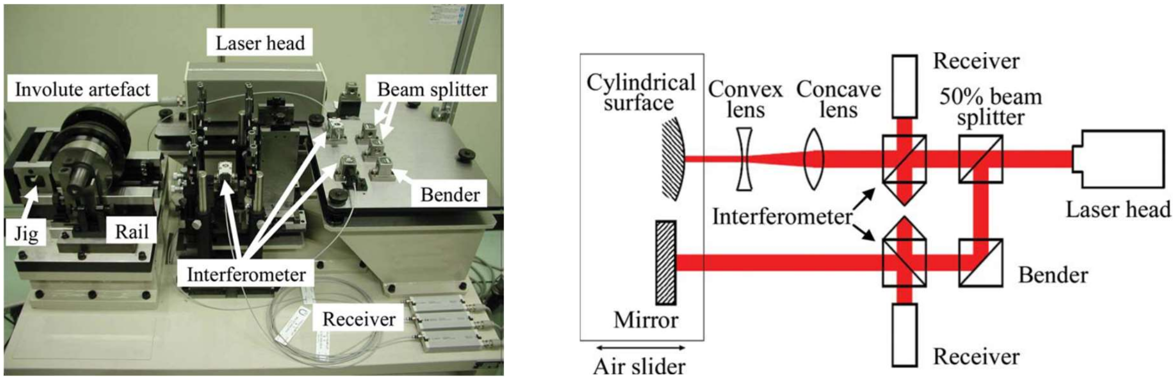

Figure 1.7: Takeoka et al.'s setup for involute artifact measurement using laser interferometry [after 16]

As illustrated in Figure 8, Fang et al. established a laser interferometric setup to measure the flank surface of helical cylindrical gears [17]. With enhanced equipment, the oblique-incidence-based approach was expanded from measuring spur gears to helical gears. They offered a ray-tracing-based approach for simulating interference fringe patterns (IFPs) while using a two-path interferometer to measure gear tooth flanks. There were two phases involved in this simulation process. The profile of an IFP was created in the first stage by ray tracing within the interferometer's object path. The profile of an IFP was then illuminated by interference fringes in the second stage. Simulations of two spur involute gears were conducted to assess the accuracy of the simulation, and the simulated IFPs were confirmed using an actual two-path interferometer established on an optical bench.

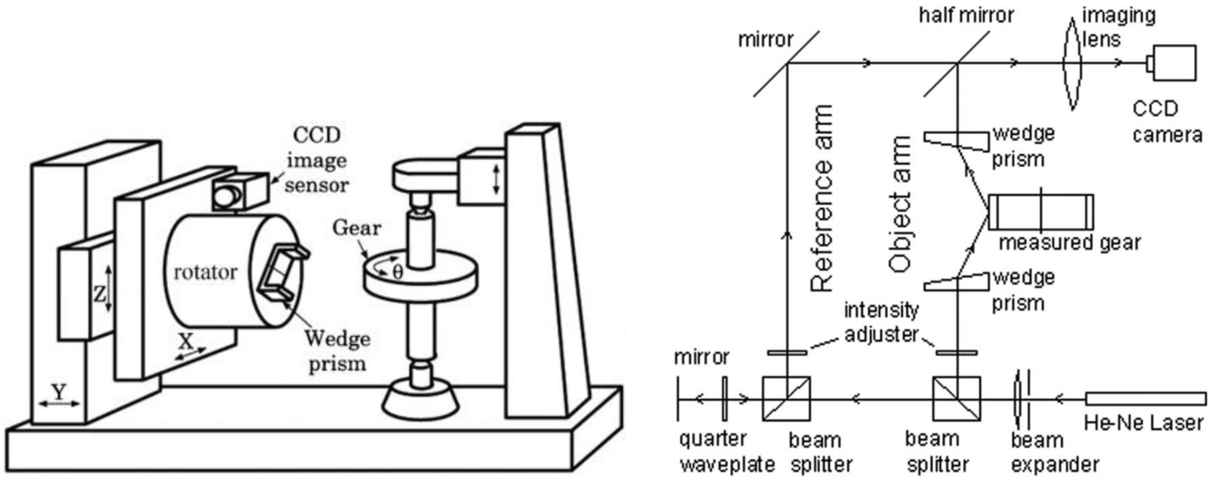

Figure 1.8: Instrument arrangement and schematic representation of the two-path interferometric system [after 17]

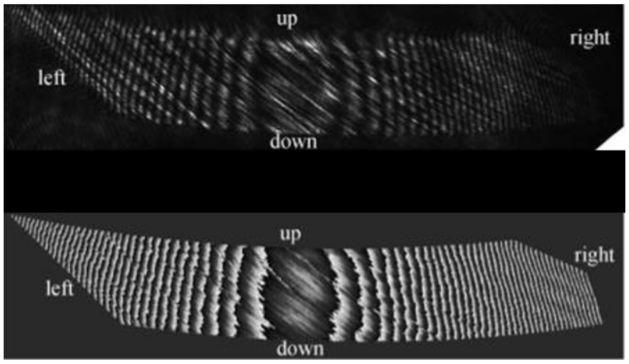

Figure 1.9: Results of measured flank using laser interferometry [after 17]

Goch stated that many triangulation-based optical instruments satisfying gear metrology demands could provide sufficient accessibility to gear flanks, speed, and accuracy [1]. In contrast, minor accessibility of gear flanks in interferometry-based measurements could make them unsatisfactory measurement methods, despite their potential to achieve the highest accuracy level.

The gear profile was measured using a phase-shift optical triangulation approach by Lu et al., which benefited from comprehensive information, speed, and non-contact nature [18]. The technology had successfully exhibited comparative measuring accuracy greater than 1 µm and resolution of about 0.1 µm while inspecting a 2 cm^2 region. The optical system's measurement findings were in good accordance with those from a mechanical probe on a coordinate measuring machine. It was also fair to realize a few teeth per second measuring speed. Different factors that affected measurement accuracy and potential remedies were examined. They, however, did not offer any standard metrics to be used in gear production metrology.

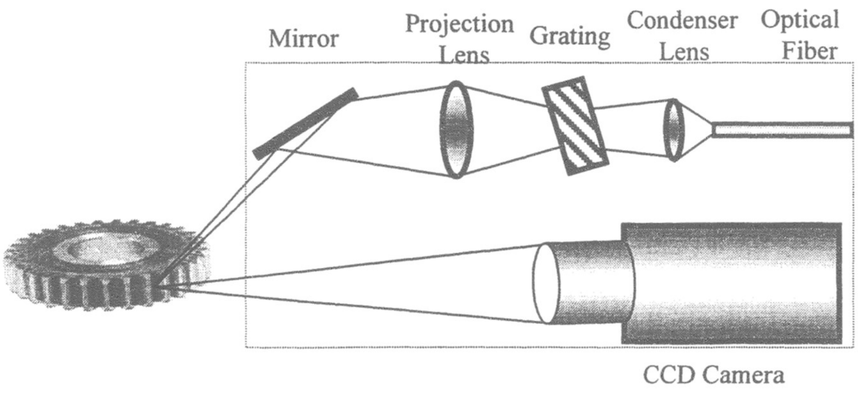

Figure 1.10: Stretch of gear measurement using Phase-shift optical triangulation [after 18]

Optical instruments equipped with a light section triangulation sensor are commonly used to enable data acquisition of dense point clouds on each gear flank in a reasonable time to capture surface topography. A laser beam is emitted from a laser source, passing through a focus lens to project the surface to be measured. Then the reflected scattered light passing through a collection lens is focused onto a photosensitive detector to form an image. The position of the image on the pixels of the detector is then analyzed to find the target's distance to the instrument [19]. This technique is called triangulation because the emitted beam, the reflected light, and the detector form a triangulation.

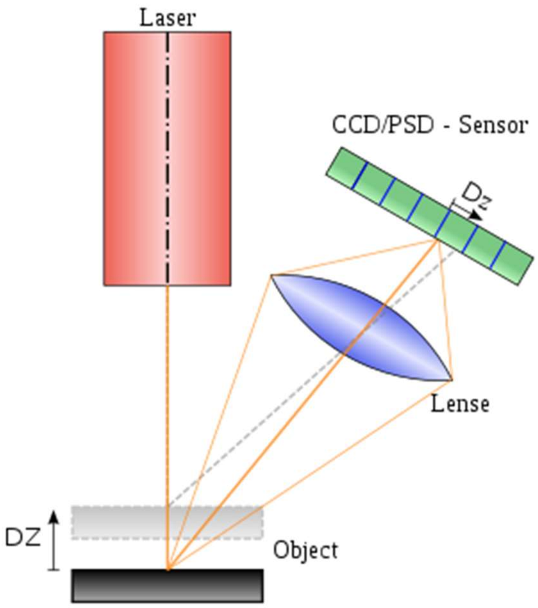

Figure 1.11: Principle of laser line triangulation [after 20]

The line structured light sensor based on point-to-point triangulation principles can also accurately be used for distance measurement. Structured light is emitted to the 3D surface to be measured, and the reflected light from other perspectives than that of the emitter is captured on a photosensitive detector. The distorted reflected light on the detectors can be used to measure the geometrical features of the surface. The significant advantages of this method are high precision, high speed, and an anti-interference nature.

The structured light technique was used first to measure a helical gear by Peters et al. [21]. They illuminated a gear flank by a structured light pattern. The distorted reflected pattern was captured by a CCD camera. Then a calibrated algorithm transferred the registered pattern along with system design data into 3D coordinates of the measured flank. They could reach the resolution on the order of 1 micrometer for a few square centimeters measuring area. The maximum deviation between the measured data and the theoretical curve did not exceed 10 micrometers.

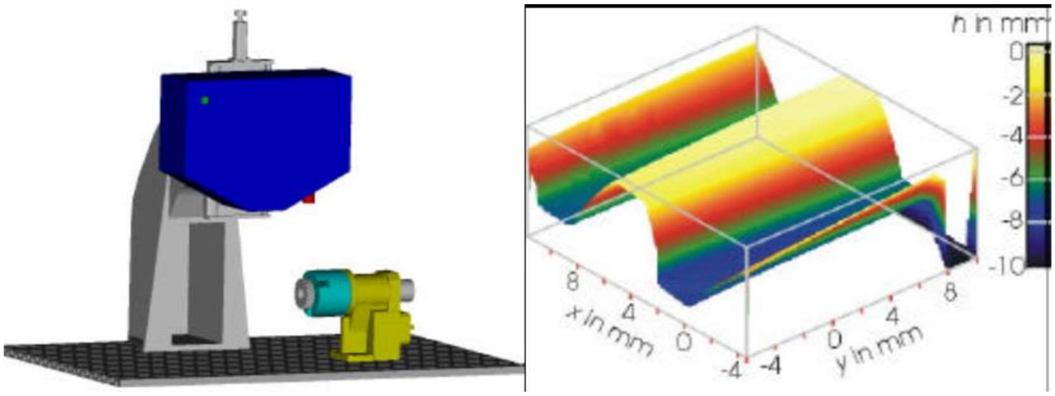

Figure 1.12: gear measurement using structured light pattern: a) Hardware setup b) Result of areal measurement [after 21]

Using a structured light pattern, Leopold et al. developed a test instrument and its supporting software to measure the entire gear flank in less than a square centimeter [22]. Fringe patterns were projected to a tooth flank, and a CCD camera recorded the distorted light due to interaction between the projected stripes and the measured surface. Their device consisted of a CCD camera as a detector and a commercially available LCD as a fringe projector which made them able to use phase correct measurements with sinusoidal fringe patterns. The sequence of the fringe pattern was used aiming at higher accuracy and a better measuring range. They recorded 10 micrometers as the best resolution achieved in the measurement area.

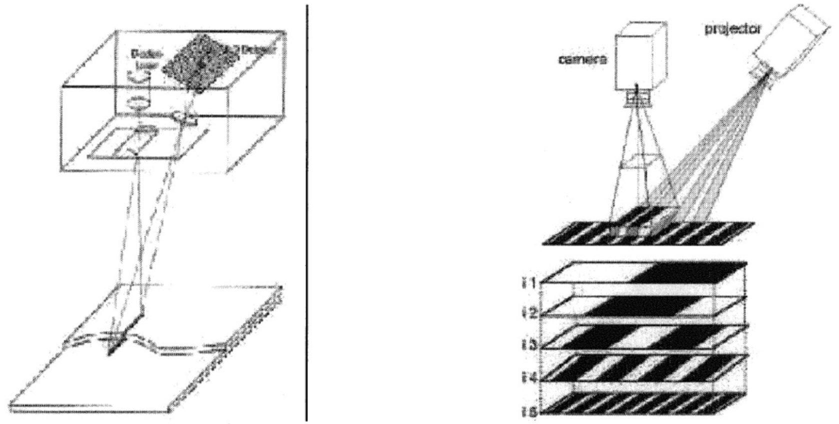

Fig. 1: Principles of Triangulation

Fig. 2: Fringe Projection

Figure 1.13 A) Principles of triangulation B) Fringe projection [after 22]

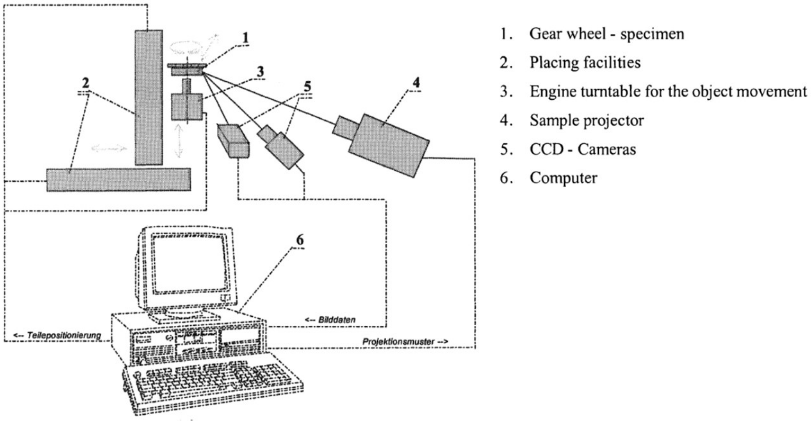

Figure 1.14: Components of Leopold et al.'s optical system [after 22]

Kumar et al. took advantage of reverse engineering in measuring gear surfaces using a 3D laser scanner [23]. They used the K-mean method and a proposed MATLAB algorithm to reconstruct the 3D coordinates of the scanned surface. This method used a noise-free scanned point cloud as the input to compute the K-mean neighbors of the points in order to regenerate the tooth profile. Although they could improve the distance sensitivity by several orders of magnitude, they did not quantitatively mention how accurately they could reconstruct the gear surface.

The Moiré method was established by Chen et al. to optically measure a gear tooth surface. A halogen lamp was used as a light source, an autocollimator was used to provide a collimated beam, and the collimated beam passing through two linear gratings formed Moiré fringes to illuminate the flank surface. The recorded fringes on a CCD camera were later used by their developed computer code to reconstruct the contour of the gear tooth surface. Then the reconstructed data were compared to the data from a Coordinate Measuring Machine as a reference to verify the results.

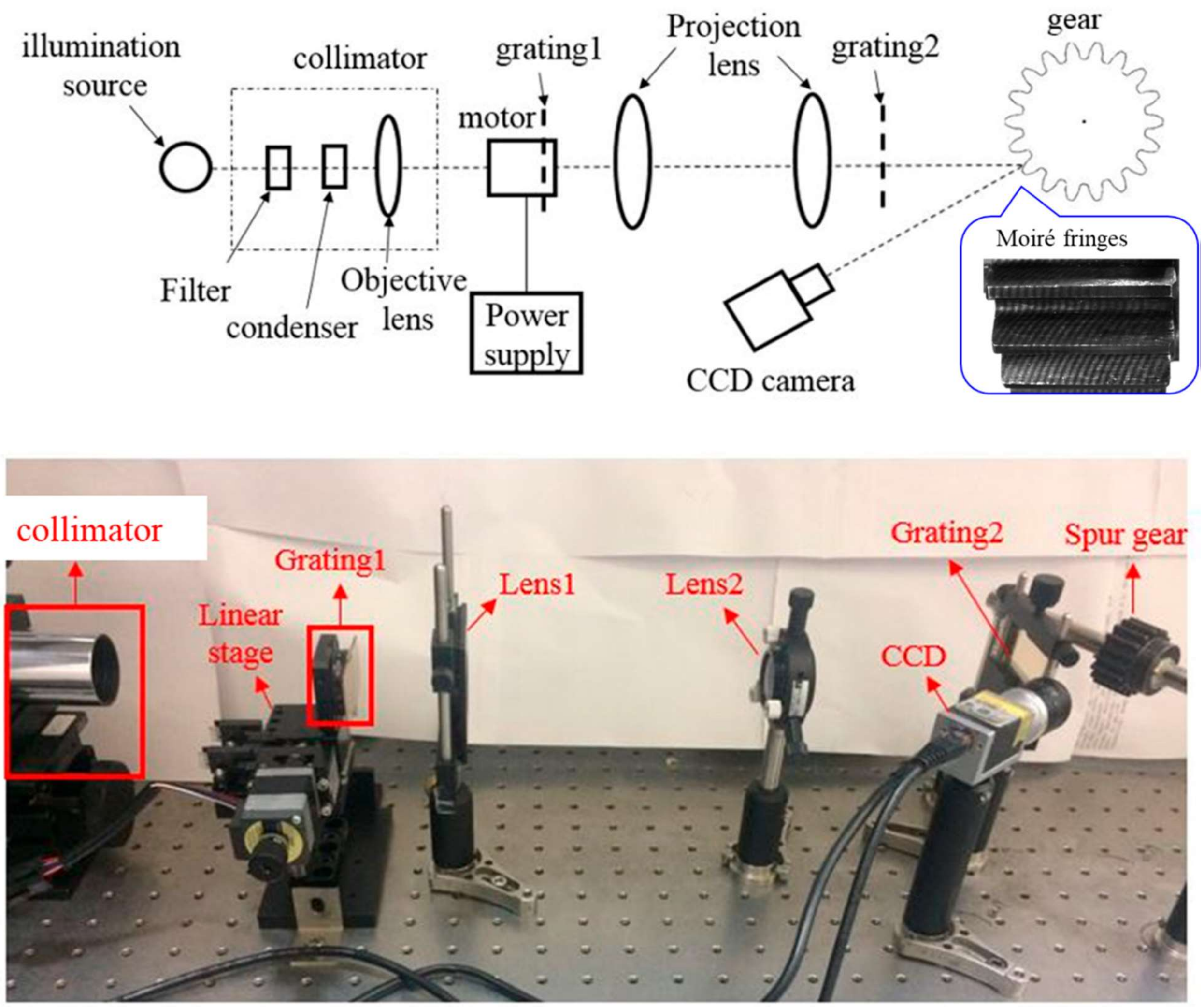

Figure 1.15: Conceptual framework and experimental setup of the projection moiré system [after 24]

An unambiguous definition of a 3D involute coordinate system for helical cylindrical gears was presented by Hartig et al., which was in reasonable agreement with conventional evaluation cross sections [25]. The presented involute coordinate system could facilitate the performance of gear evaluation. They also showed that the gear deviations in pitch, profile, and helix directions could be correlated with one another if the gear is modeled in one workpiece coordinate system, although that correlation is unknown in the current flank evaluation strategy. Compared to cartesian-based models, this can better describe the dynamic behaviors of the mating gears as well. They did not, however, include an appropriate measuring technique. Despite the multitude of optical techniques reviewed, no gear deviation parameters were offered.

1.3 Commercial Systems

Alternatively, since 2015, numerous commercial devices with various opto-mechanical setups have been developed due to state-of-the-art laser triangulation technology. MS3D [27], Nikon [28], and Gleason [29], for example, provided instruments that can collect dense areal data over the entire flank surface in a few seconds.

Hexagon designed a structured light-based point cloud measuring machine. The instrument measures a gear flank with four structured light sensors facing the target flank and an inner bore with a separate line structured light sensor mounted above the upper face. However, areal gear measurement with such a commercial instrument is still under experimental investigation.

Figure 1.16: Commercial optical measuring instruments: a) MS3D [27] b) Nikon HN-C3030 [28] c) Gleason 300GMSL [29] [after 26]

Nikon also developed the HN-C3030, a high-speed, high-precision flank topography measurement instrument that can be applied for gear inspection of a variety of gears with diameters of less than 300 mm. The contactless HN-C3030 3D measuring instrument is designed for precision and fast measurement of sophisticated components such as gears, impellers, turbine blades, etc. Nikon has made a big step ahead in ultra-fast shape evaluation compared to conventional tactile measurement techniques with the HN-C3030, which has an innovative laser scanner. Customers can gain superior insights into product compliance by inspecting and correlating the measured surface to the original CAD file, resulting in rapid problem-solving.

Gear vibration and noise cause lots of problems for power transmission systems of automotive and wind turbines. A critical consideration in gear vibration and noise is the micrometer-order form deviations [16,34]. On the other hand, the presence of speckles and other types of scattered light in optical inspection is an inevitability according to the physics of optical measurement. As a result, when triangulation sensors are used, the scattered-based light deflection might cause unexpected, large form deviations. It has always been challenging to compare optical evaluation results with reference results, i.e., acquired by tactile measurement since large form deviations increase measurement uncertainty.

Aside from that, it is essential to detect and remedy or avoid multiple light reflections, which might lead to inaccurate point clouds evaluated from an optical measurement of the flank surface [34]. In order to be recognized by the automotive industry, the holistic areal evaluation will also have to be consistent with the present conventional line-oriented evaluation within a few microns.

This dissertation contributes toward addressing the problem of large, evaluated form deviations and multiple light reflection. An optical instrument equipped with a light section triangulation sensor is used to measure certain reference geometries, i.e., flat surface, cylinder, and sphere, as well as certain commercial gears to investigate and improve the fidelity of triangulation sensor measurements in optical inspections.

1.4 Dissertation layout

Chapter 1 has provided an overview of this study's background, motivation, and importance. The measurement and evaluation aspects of modern gear metrology technologies have been discussed. Classical gear inspection, based on a line-oriented tactile measurement, must be replaced with a faster, areal inspection that can capture complex modern gear modifications to adapt to the current needs of new applications. New requirements for gear metrology, including sufficient speed and accuracy, can be met through triangulation-based optical instruments. Since speckles and scattered light are inevitable during an optical inspection, they can cause large form deviations in the reconstructed geometry. This large, evaluated form deviation imposes a severe technical gap for further adapting optical areal measurement systems in the industry.

Chapter 2 describes the triangulation principle and peak detection algorithm and how the current embedded (OEM) algorithm can lead to large, evaluated form deviation. Then an improved mathematical approach is introduced for peak detection in each sensor frame to detect the peak position of that frame even more accurately. A MATLAB algorithm is developed based on the current mathematical approach. The impact of this algorithm on point clouds derived from surface measurements is analyzed in comparison to that of the embedded algorithm by measuring four reference geometries.

Chapter 3 focuses on assessing the algorithm on various sets of simulated data. Each actual sensor frame consists of 1024 rows. The data is simulated based on the both exponential and quadratic distribution of light intensities over each row for both quadratic and elliptical ridge line profiles, which is the line in the x-y sensor domain with the highest light intensity.

Chapter 4 studies the structure of actual sensor data to perform preprocessing on individual frames. Depending on the measured geometry, the ridge line profile that appears on the sensor varies. Four reference geometries are measured in this dissertation whose ridge line profiles are either quadratic or elliptical. Then the preprocessed frame is fed into the algorithm for the peak detection purpose for two types of ridge line profiles. The ridge line detected by the UNCC algorithm is compared with that by the Nikon algorithm to illustrate peak detection improvement. Then a rough correlation between the sensor coordinate system and the workpiece coordinate system is derived by performing an experimental measurement. This correlation offers a rough estimation of how implementing the UNCC algorithm can improve the evaluated form deviations.

Chapter 5 gives the experimental verification of applying the UNCC algorithm in the measurement process of four reference geometries. The instrument creates two sets of information from any surface measurement; the sensor data and the lin file, including all the measurement information, which later forms the point clouds. This chapter uses the sensor data exported from the instrument to find the modified peak positions.

First, the sensor data, including several successive sensor frames, is used as the algorithm input. Then the peak detection algorithm is applied on every frame to find the modified peak positions of all frames. Then the original peak positions in the lin file are replaced with the modified ones to create the modified lin file. Finally, the modified lin file is converted to modified point clouds. The entire process is performed for four measured reference geometries to show the fidelity improvement of triangulation sensor measurement.

Chapter 6 presents the conclusion of this dissertation and suggests several future works.

2 CHAPTER 2: METHODOLOGY

The use of laser triangulation sensors is one methodology for precisely measuring the distance between a single point or line of points and the sensor reference. A light section triangulation sensor is widely adopted in optical instruments to enable the acquisition of extensive point clouds in a fair period of time in order to obtain surface topography. After a laser beam passes through a focusing lens to project onto the surface to be measured, the scattered light reflected from the surface passes through a collecting lens and is focused onto a photosensitive detector to create a spot image. As the target's relative distance varies, the spot's absolute position in the detector's coordinate system varies correspondingly. Hence, the spot's location on the detector is then processed to evaluate the target's distance from the light section. The approach is referred to as triangulation because the sensor, the emitted laser, and the reflected laser together resemble a triangle when seen from different perspectives. To speed up the measurement process, a laser spot is usually replaced with a laser stripe to swipe the target surface. This can be accomplished by passing the beam through a cylindrical lens or a Powell lens.

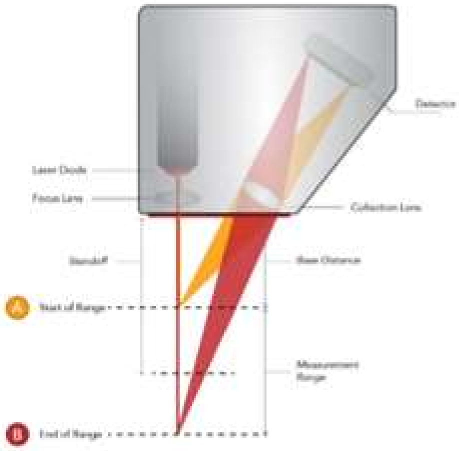

Figure 2.1: Schematic principles of laser triangulation sensor [after 19]

Since the triangulation principle used to measure a target surface is based on a laser light source, speckles and other scattered light phenomena may appear on the sensor detector as a result of the deflected laser stripe. The reflected stripe on the CCD camera would be detected as a series of bright successive rows with an uneven intensity distribution in one sensor frame as depicted in Figure 2.2. Depending on the machine capturing frequency, which will be covered in detail in section 2.2, the result of the scanned surface consists of multiple consecutive sensor image frames. In each bright row, the light intensities form a bell-shaped distribution. Meaning that the intensity values start at zero, rise to a major peak, then fall to zero in each nonzero intensity row. In a simplified manner, the position of the pixel with the highest intensity is referred to as the peak position value of each successive row. In the original evaluation method, a 2D profile connecting all successive peaks over the CCD camera, referred to as a *ridge line* in this dissertation, is used as the 2D profile of the reflected stripe. This profile on the detector is then used to evaluate the location in space of the physical measured profile on the target surface.

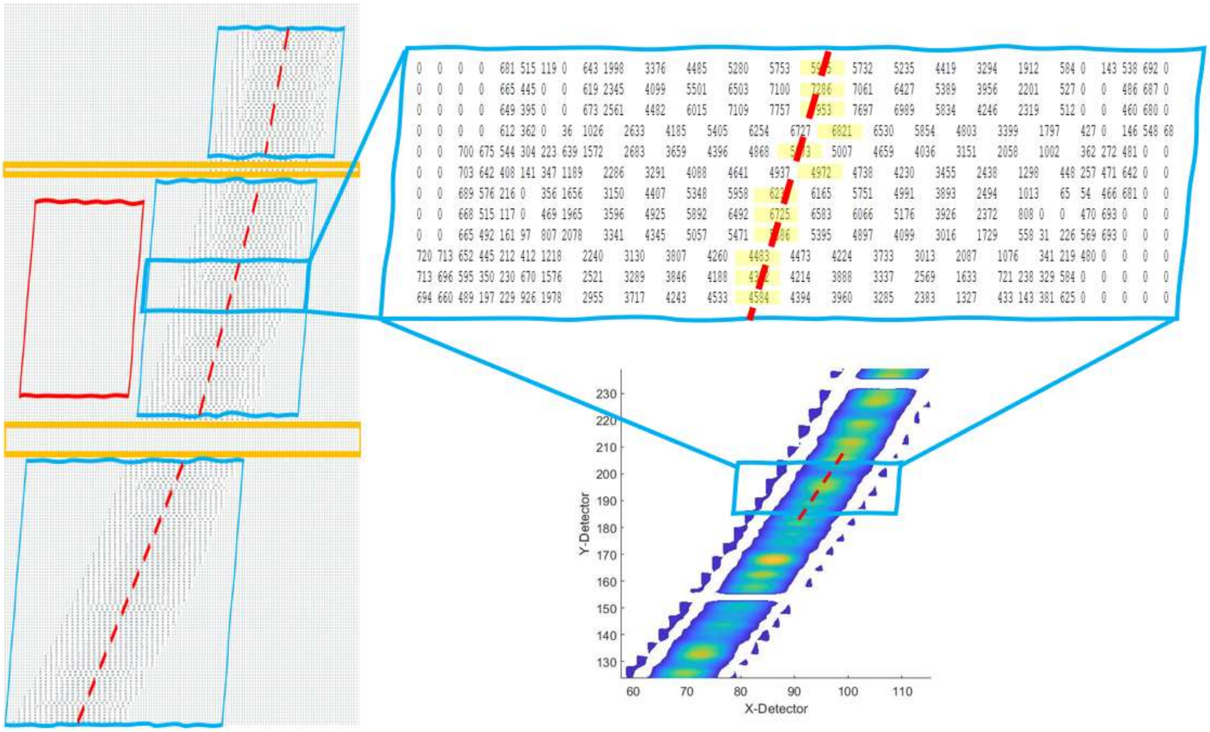

```
0   0   0   0   681 515 119 0   643 1998 3376 4485 5280 5753 [illegible] 5732 5235 4419 3294 1912 584 0 143 538 692 0
0   0   0   0   665 445 0   0   619 2345 4099 5501 6503 7100 7286 7061 6427 5389 3956 2201 527 0 0 486 687 0
0   0   0   0   649 395 0   0   673 2561 4482 6015 7109 7757 [illegible] 7697 6989 5834 4246 2319 512 0 0 460 680 0
0   0   0   0   612 362 0   36  1026 2633 4185 5405 6254 6727 6821 6530 5854 4803 3399 1797 427 0 146 548 68
0   0   700 675 544 304 223 639 1572 2683 3659 4396 4868 [illegible] 5007 4659 4036 3151 2058 1002 362 272 481 0 0
0   0   703 642 408 141 347 1189 2286 3291 4088 4641 4937 4972 4738 4230 3455 2438 1298 448 257 471 642 0 0
0   0   689 576 216 0   356 1656 3150 4407 5348 5958 [illegible] 6165 5751 4991 3893 2494 1013 65 54 466 681 0 0
0   0   668 515 117 0   469 1965 3596 4925 5892 6492 6725 6583 6066 5176 3926 2372 808 0 0 470 693 0 0 0
0   0   665 492 161 97  807 2078 3341 4345 5057 5471 [illegible] 5395 4897 4099 3016 1729 558 31 226 569 693 0 0 0
720 713 652 445 212 412 1218 2240 3130 3807 4260 4483 4473 4224 3733 3013 2087 1076 341 219 480 0 0 0 0
713 696 595 350 230 670 1576 2521 3289 3846 4188 [illegible] 4214 3888 3337 2569 1633 721 238 329 584 0 0 0 0 0
694 660 489 197 229 926 1978 2955 3717 4243 4533 4584 4394 3960 3285 2383 1327 433 143 381 625 0 0 0 0 0
```

Figure 2.2: Intensity distribution of reflected laser stripe on CCD camera in one sensor image frame

The above-mentioned light phenomena might cause some inaccurate peak position detection in the original evaluation method. The peak shift in sensor X-Y direction leads to a deviation in the evaluated distance, approximately perpendicular to the part surface. This is considered the main reason for the apparent form deviation in the measured results, which are not plausible in physical or technical terms since the measured references have finished surfaces with a form deviation in the single-digit micrometer range (e.g., 3-5 μm). The objective of the performed research is to develop a mathematical approach to improve the detection of the ridge line within each frame for all the consecutive frames. The ridge line is the line in the X-Y domain with the highest intensity, as illustrated in the contour plot in Figure 2.4 as a blue dashed line. Using information about the sensor position relative to the workpiece, each scanned ridge line is transformed to spatial XYZ coordinates. Combining the XYZ data from consecutive ridge lines will form a representation of the entire surface (referred to as measured points).

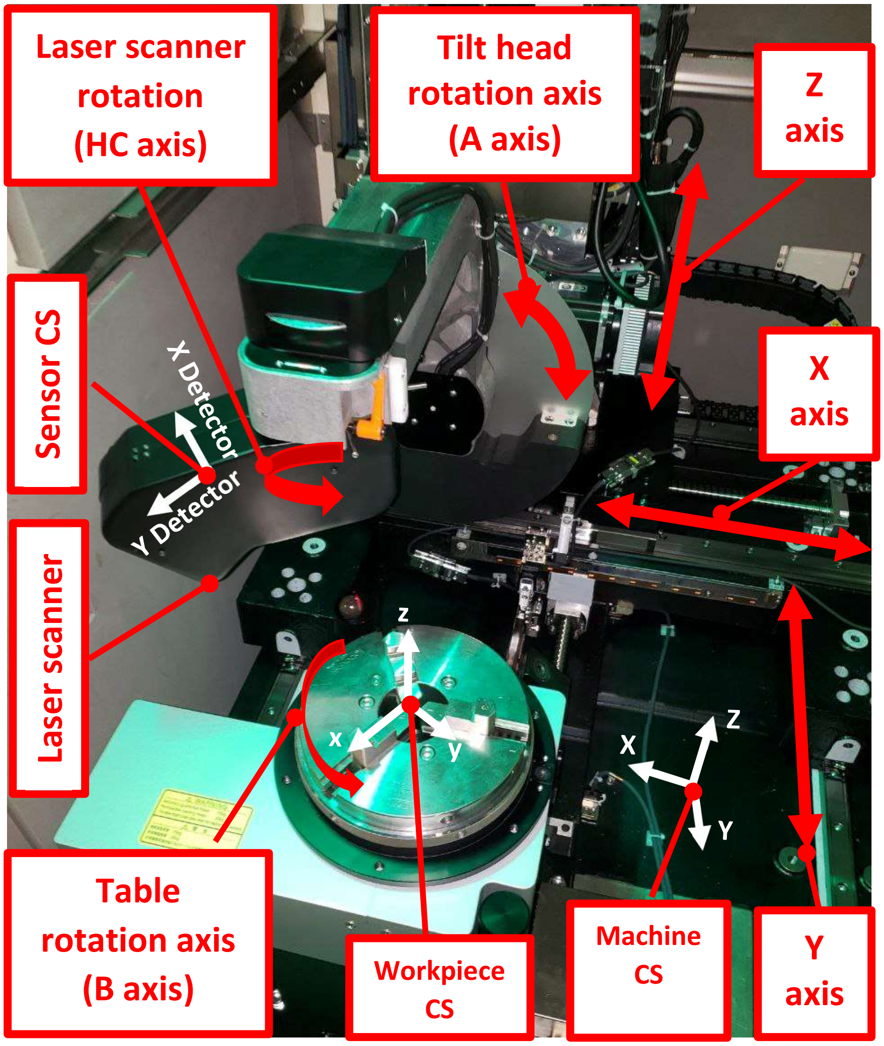

Figure 2.3: Nikon instrument’s coordinate systems

The advantage of the presented frame-by-frame approach to finding the ridge line compared to the original row-by-row approach is that in the original approach, the continuity of the measured profile is not considered when the peak detection of each row is independent of its adjacent rows. This makes the original method vulnerable to any dislocation of the intensity peaks due to environmental issues. In Contrast, the presented method follows a more global approach by enforcing continuity of the ridge line through the simultaneous evaluation of all the nonzero-intensity rows in a scanned frame. Some alternative mathematical approaches will be considered for the instrument to detect the peak position even more accurately.

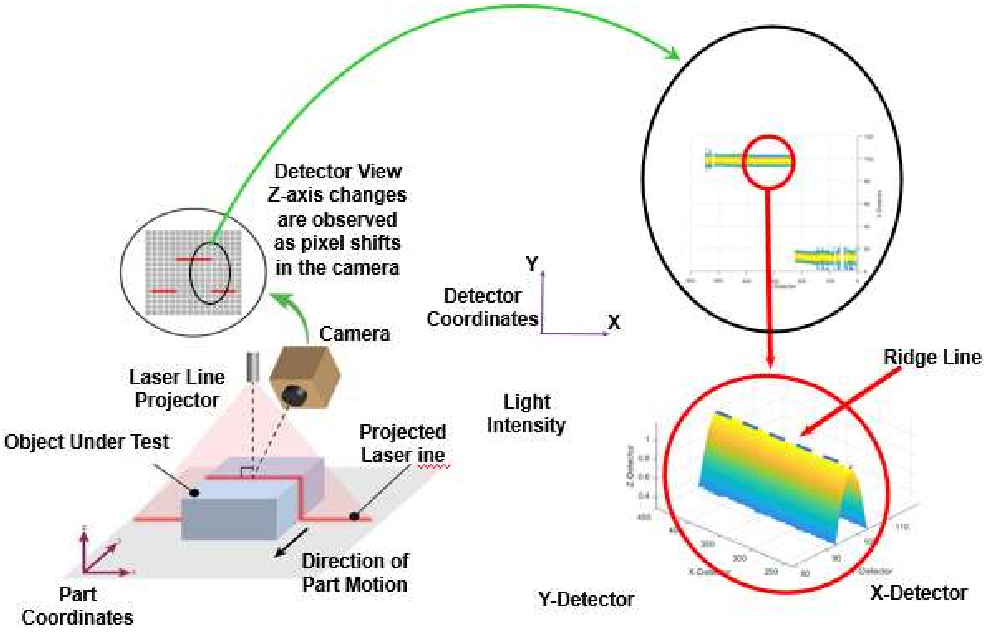

Figure 2.4: Intensity distribution of the sensor image frame vs. the ridge line in triangulation sensor [after 1]

2.1 Mathematical Description

Suppose the intensity at any given point, described by (x,y) coordinates in the sensor plane, can be found as an analytical function of x and y. The deviation between the measured and analytical model-based intensity can be calculated. To do so, a description of the intensity ridge line is needed depending on the geometry to be measured. According to the investigated geometries in this dissertation, i.e., flat surface, cylinder, sphere, and helical cylindrical gear, and based on the performed optimization that will be covered in detail later, the ridge line profile is considered a quadratic polynomial for all the references except for sphere whose ridge line can be modeled best with an ellipse.

Figure 2.5 illustrates the ridge lines in the cases of cylinder and sphere measurements. In both cases, the ridge line detected by the original evaluation method is shown in green and referred to as the rough solution. Different fitting methods are tested in each case to determine which can best fit the rough solution; in other words, which profile can better describe the rough solution.

In the case of the cylinder measurement, a circle fit, an ellipse fit, and a quadratic polynomial fit are examined, among which the quadratic polynomial profile can interestingly fit the rough solution. Similarly, a quadratic polynomial can best model the ridge line profile of flat surfaces and cylindrical gears as shown in chapter 4. In the case of the sphere measurement, on the other hand, the ellipse fit offers a better match with the rough solution compared to the circle fit.

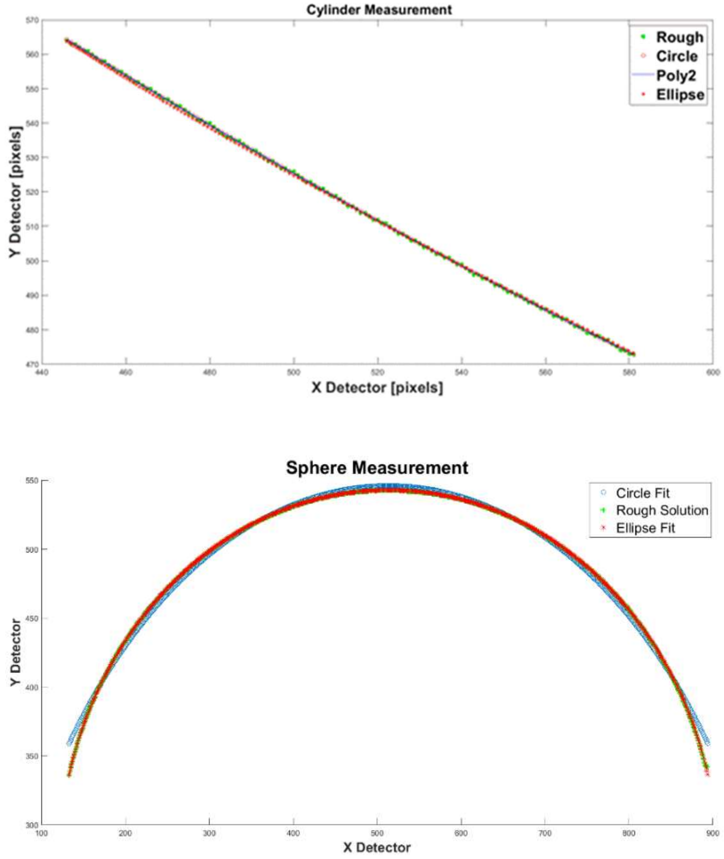

Figure 2.5: Best fit to the ridge line profile for cylinder and sphere measurement

2.1.1 Quadratic Ridge Line

Following the results given in the current dissertation, a quadratic polynomial can best represent the ridge line profile of the flat surface, cylinder, and helical cylindrical gear on the sensor plane. Then the local coordinate (ξ) on the ridge line can be defined in any of the three following directions, as demonstrated in Figure 2.6.

A) Perpendicular to the ridge line

B) Along the x direction

C) Along the y direction

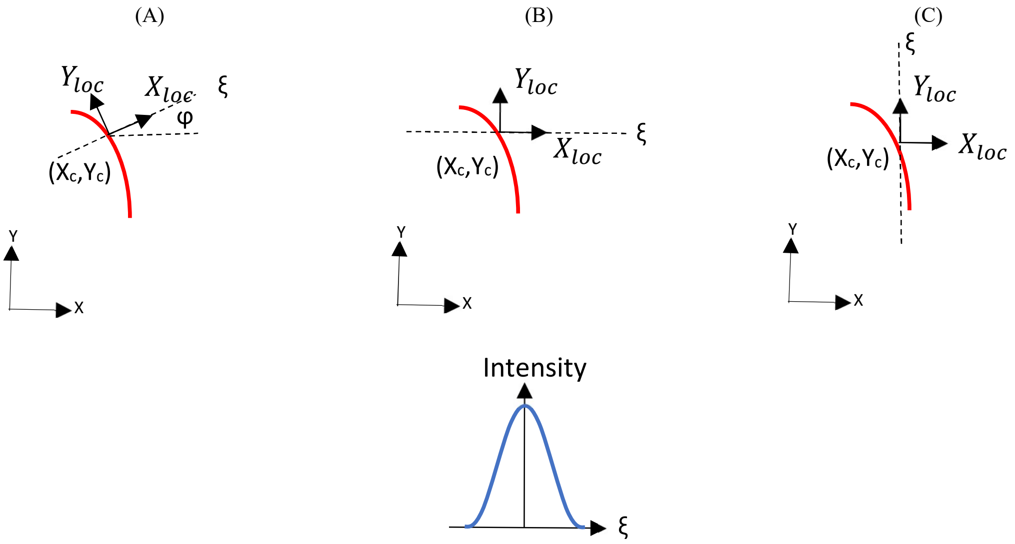

Figure 2.6: Illustration of ridge line profile in the sensor's X-Y-plane and intensity distribution along one local coordinate (ξ)

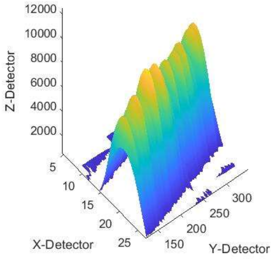

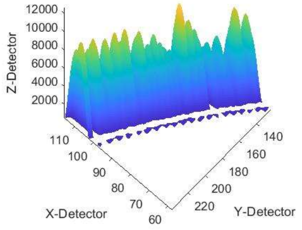

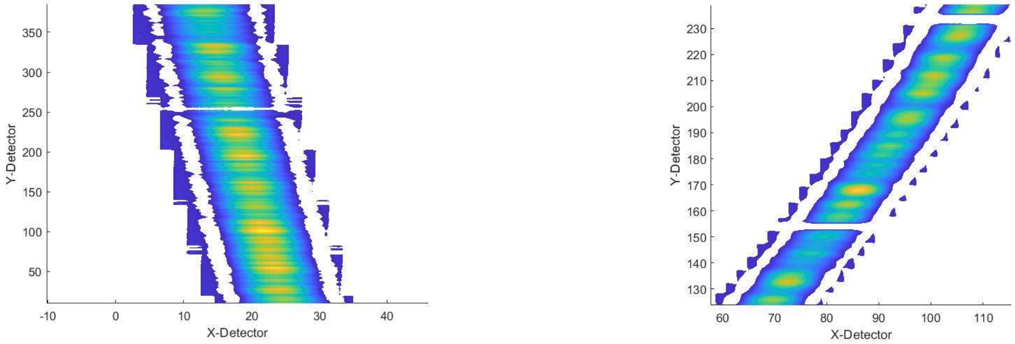

Figure 2.7: 3D and 2D plotted sensor image frame for linear (left) and quadratic (right) polynomials as the ridge line

This section aims to find a 3D analytical model for the Intensity distribution across the 2D sensor plane. Three possible cases mentioned above will be described depending on how the orientation of the local coordinate is defined with respect to the projected ridge line profile on the sensor plane.

2.1.1.1 Local Coordinate Perpendicular to Ridge Line

In the first case, the local x coordinate is perpendicular to the ridge line profile ($\xi = X_{loc}$), and the ridge line is considered a quadratic curve where y_c is a function of x_c.

$$y_c(x) = a_0 + a_1 x_c + a_2 {x_c}^2$$

(2.1) (*ref* A. a. 1)[1]

$$\begin{pmatrix} x_{loc} \\ y_{loc} \end{pmatrix} = \begin{pmatrix} \cos\varphi & \sin\varphi \\ -\sin\varphi & \cos\varphi \end{pmatrix} \begin{pmatrix} x - x_c \\ y - y_c \end{pmatrix}$$

(2.2) (*ref* A. a. 3)

$$I(\xi, x_c, y_c) = b_0(x_c, y_c) - b_2(x_c, y_c)\xi^2$$

(2.3) (*ref* A. a. 4)

[1] The *ref* equation numbers relate to the full derivation in Appendix A.

Since the slope of the perpendicular line (φ) can be calculated having the slope of the tangent line to the ridge line ($\frac{dy_c}{dx_c}$), which is known for any point along $y_c(x_c)$, and X_{loc} is equal to ξ, then the intensity distribution can be determined as the function of x and y coordinates of the ridge line (I(x_c, y_c)). The straight line perpendicular to the ridge line passing through (x_c, y_c) is described by equation (2.4). Then, combining equations (2.1) to (2.4), ξ can be found to be substituted in equation (2.3). It is also assumed that b_0 and b_2 are constant over the ridge line. This means that the height of the intensity peaks along the ridge line and the width of the intensity stripe are both assumed to be constant. Plugging equation (2.5) into (2.3) gives equation (2.6):

$$y - y_c = \frac{-1}{\frac{dy_c}{dx_c}}(x - x_c)$$

(2.4)
(*ref* A.a.10)

$$\xi = (x - x_c)\sqrt{1 + \left(\frac{1}{\frac{dy_c}{dx_c}}\right)^2}$$

(2.5)
(*ref* A.a.13)

$$I(\xi, x_c, y_c) = b_0 - b_2(x - x_c)^2\left(1 + \left(\frac{1}{a_1 + 2a_2x_c}\right)^2\right)$$

(2.6)
(*ref* A.a.15)

Equations (2.1) and (2.4) are combined to remove y_c and obtain equation (2.7) for x_c . Considering the known values for x and y, which are the locations of any given pixel in the sensor coordinate system, equation (2.7) can be solved for x_c. Since x_c is a non-linear function of the a_i coefficients leading to a highly non-linear distance function, the other two directions for x_{loc} are going to be assessed, hoping to reach a more linear distance function in terms of a_i and b_i coefficients.

$$(x + a_1y - a_1a_0) + (2a_2y - a_1{}^2 - 2a_2a_0 - 1)x_c + (-3a_2a_1)x_c{}^2 + (-2a_2{}^2)x_c{}^3 = 0$$

(2.7)
(*ref* A.a.17)

$$x_c = f(x, y)$$

(2.8)
(*ref* A.a.18)

2.1.1.2 Local Coordinate Along with X Direction

In the second case, the local x coordinate is along with the sensor x direction ($\xi = x - x_c$) and $y = y_c$. Therefore, the local coordinates can be determined by equation (2.10). Solving the equation (2.9) for x_c and put that in (2.3), equation (2.11) can be derived. Similar to what was done in the previous case and having an analytical-based model for the intensity distribution, the distance function, which is the residual between the measured and the model-based intensity (I_m and I_a respectively), can be found for any given pixel (x, y) on the sensor. The distance function is defined in equation (2.12) in terms of a_i and b_i coefficients which are named as the solution and denoted by s and defined by $\vec{s} = (a_0, a_1, a_2, b_0, b_2\ )$ so that s_1 is a_0 and s_5 is b_2. Then the solution changes, denoted by Δs and defined by $\overrightarrow{\Delta s} = (\Delta a_0, \Delta a_1, \Delta a_2, \Delta b_0, \Delta b_2\ )$, are added up to the solution in the distance function. Then the objective function (Q) shown in equation (2.13), which is the root square of the sum of the squares of the distance function values for all the sensor pixels, is optimized with respect to the solution changes iteratively.

Since equation (2.14) leads to an extremely complicated non-linear equation in terms of Δs_j the last direction is going to be assessed.

$$y_c(x) = a_0 + a_1 x_c + a_2 {x_c}^2 \qquad (2.9)\ (\mathit{ref}\ \mathrm{A.b.1})$$

$$\begin{pmatrix} x_{loc} \\ y_{loc} \end{pmatrix} = \begin{pmatrix} x - x_c \\ y_c \end{pmatrix} \qquad (2.10)\ (\mathit{ref}\ \mathrm{A.b.4})$$

$$I_a(x,y) = b_0 - b_2 \left(x - \left(\frac{-a_1 \pm \sqrt{{a_1}^2 - 4a_2(a_0 - y)}}{2a_2} \right) \right)^2 \qquad (2.11)\ (\mathit{ref}\ \mathrm{A.b.8})$$

$$d_i = I_i(s_j + \Delta s_j) - I_{m,i} \qquad (2.12)\ (\mathit{ref}\ \mathrm{A.b.11})$$

$$Q = \sqrt{\sum_{i=1}^{n} {d_i}^2} \qquad (2.13)\ (\mathit{ref}\ \mathrm{A.b.13})$$

$$\sum_{i=1}^{n} \left(s_4 + \Delta s_4 - I_{m,i} - (s_5 + \Delta s_5) \left(x_i + \left(\frac{(s_1 + \Delta s_1) \pm \sqrt{(s_2 + \Delta s_2)^2 - 4(s_3 + \Delta s_3)(s_1 + \Delta s_1 - y_i)}}{2(s_1 + \Delta s_1)} \right) \right)^2 \frac{\partial d_i}{\partial \Delta s_j} \right) = 0 \qquad (2.14)\ (\mathit{ref}\ \mathrm{A.b.15})$$

2.1.1.3 Local Coordinate Along with Y Direction

In the last case, the local y coordinate is along with the sensor y direction $\xi = y - y_c$ and $x = x_c$. It is assumed that the ridge line $y_c(x_c)$ of the intensity distribution in the X-Y plane is known as a starting solution, i.e., a smooth line following the peaks of the intensity distributions over the successive rows. Plugging equation (2.15) into (2.3), the analytical model for the intensity of any arbitrary point (x, y) is found as $I_a(x, y)$.

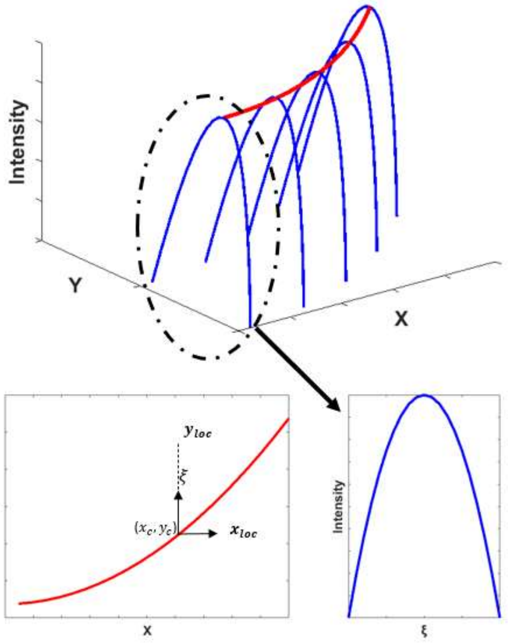

Figure 2.8: Illustration of the ridge line in the sensor's X-Y plane and intensity distribution along y_{loc} coordinate

$$y_c(x) = a_0 + a_1 x_c + a_2 {x_c}^2 \quad (2.15)\ (ref\,\mathrm{A.c.1})$$

$$\begin{pmatrix} x_{loc} \\ y_{loc} \end{pmatrix} = \begin{pmatrix} x_c \\ y - y_c \end{pmatrix} \quad (2.16)\ (ref\,\mathrm{A.c.2})$$

$$I_a(x, y) = b_0 - b_2(y - (a_0 + a_1 x + a_2 x^2))^2 \quad (2.17)\ (ref\,\mathrm{A.c.6})$$

As discussed earlier, the square root of the sum of the squares of the residuals between the measured and the model-based intensity (I_m and I_a respectively) for all the sensor pixels is called the objective function (Q). This objective function needs to be a minimum to find the best approximation for I_a. To do so, the intensity function should be written in terms of $s_j + \Delta s_j$ ($a_j + \Delta a_j$ and $b_j + \Delta b_j$). Then, Q should be iteratively minimized with respect to the five variable changes (Δs_j) as given in equation (2.20) [31]. In equation (2.19), *i* denotes the point number, and k denotes the number of iterations.

$$d_i = I_i(s_j + \Delta s_j) - I_{m,i} \quad (2.18)\ (ref\,\mathrm{A.c.7})$$

$$Q_k = \sqrt{\sum_{i=1}^{n} {d_{i,k}}^2} \quad (2.19)\ (ref\,\mathrm{A.c.9})$$

An initial solution $s_{j,0}$ ($\overrightarrow{s_0} = (a_{0,0}, a_{1,0}, a_{2,0}, b_{0,0}, b_{2,0})$) is needed to start the iterations. One approach to finding the initial solution which is used in this work is to find the positions of the arrays with maximum intensities in X-Y sensor coordinate and find a quadratic polynomial regression to find the initial ridge line coefficients ($a_{0,0}, a_{1,0}, a_{2,0}$) for each sensor frame. Then the 1st nonzero-intensity row of the same sensor frame is used to find the initial coefficients ($b_{0,0}, b_{2,0}$) for the quadratic intensity distribution using another quadratic polynomial regression. Considering the coefficient changes for the initial solution labeled as $\Delta s_{j,0}$ ($\overrightarrow{\Delta s_0} = (\Delta a_{0,0}, \Delta a_{1,0}, \Delta a_{2,0}, \Delta b_{0,0}, \Delta b_{2,0})$), the initial solution can be improved and used as the first solution for the next iteration.

$$Q_{min} \rightarrow \frac{\partial Q_0}{\partial \Delta s_{j,0}} = 0, \quad \begin{cases} \dfrac{\partial Q_0}{\partial \Delta a_{0,0}} = 0 \\ \dfrac{\partial Q_0}{\partial \Delta a_{1,0}} = 0 \\ \dfrac{\partial Q_0}{\partial \Delta a_{2,0}} = 0 \\ \dfrac{\partial Q_0}{\partial \Delta b_{0,0}} = 0 \\ \dfrac{\partial Q_k}{\partial \Delta b_{2,0}} = 0 \end{cases} \rightarrow \begin{cases} \dfrac{1}{2\sqrt{\sum_{i=1}^{n} {d_{i,0}}^2}} \sum_{i=1}^{n} \left(2d_{i,0} \dfrac{\partial d_{i,0}}{\partial \Delta a_{0,0}} \right) = 0 \\ \dfrac{1}{2\sqrt{\sum_{i=1}^{n} {d_{i,0}}^2}} \sum_{i=1}^{n} \left(2d_{i,0} \dfrac{\partial d_{i,0}}{\partial \Delta a_{1,0}} \right) = 0 \\ \dfrac{1}{2\sqrt{\sum_{i=1}^{n} {d_{i,0}}^2}} \sum_{i=1}^{n} \left(2d_{i,0} \dfrac{\partial d_{i,0}}{\partial \Delta a_{2,0}} \right) = 0 \\ \dfrac{1}{2\sqrt{\sum_{i=1}^{n} {d_{i,0}}^2}} \sum_{i=1}^{n} \left(2d_{i,0} \dfrac{\partial d_{i,0}}{\partial \Delta b_{0,0}} \right) = 0 \\ \dfrac{1}{2\sqrt{\sum_{i=1}^{n} {d_{i,0}}^2}} \sum_{i=1}^{n} \left(2d_{i,0} \dfrac{\partial d_{i,0}}{\partial \Delta b_{2,0}} \right) = 0 \end{cases} \tag{2.20}$$

(ref A.c.12)

The square roots in the denominators of the five equations in equation (2.20) must be positive and different from zero in the non-trivial case. Therefore, only the numerators must be considered. However, the highly non-linear term in the nominator, $f_{j,0} = \sum_{i=1}^{n} \left(d_{i,0} \frac{\partial d_{i,0}}{\partial \Delta s_{j,0}} \right)$, is linearized with respect to $\Delta s_{j,0}$ to find a linear equation $g_{j,0}$. Performing the same linearization for all five non-linear equations and setting them to zero ends up with a system of five linear equations in equation (2.22).

$$\begin{aligned} f_{1,0} &= \sum_{i=1}^{n} \left(d_{i,0} \frac{\partial d_{i,0}}{\partial \Delta a_{0,0}} \right) \rightarrow g_{1,0}\text{: } linearized\ f_{1,0}\ with\ respect\ to\ \Delta s_{1,0} \\ f_{2,0} &= \sum_{i=1}^{n} \left(d_{i,0} \frac{\partial d_{i,0}}{\partial \Delta a_{1,0}} \right) \rightarrow g_{2,0}\text{: } linearized\ f_{2,0}\ with\ respect\ to\ \Delta s_{2,0} \\ f_{3,0} &= \sum_{i=1}^{n} \left(d_{i,0} \frac{\partial d_{i,0}}{\partial \Delta a_{2,0}} \right) \rightarrow g_{3,0}\text{: } linearized\ f_{3,0}\ with\ respect\ to\ \Delta s_{3,0} \\ f_{4,0} &= \sum_{i=1}^{n} \left(d_{i,0} \frac{\partial d_{i,0}}{\partial \Delta b_{0,0}} \right) \rightarrow g_{4,0}\text{: } linearized\ f_{4,0}\ with\ respect\ to\ \Delta s_{4,0} \\ f_{5,0} &= \sum_{i=1}^{n} \left(d_{i,0} \frac{\partial d_{i,0}}{\partial \Delta b_{2,0}} \right) \rightarrow g_{5,0}\text{: } linearized\ f_{5,0}\ with\ respect\ to\ \Delta s_{5,0} \end{aligned} \tag{2.21}$$

(ref A.c.13)

Rearranging the five linear equations in terms of the changes ($\overrightarrow{\Delta s} = (\Delta a_0, \Delta a_1, \Delta a_2, \Delta b_0, \Delta b_2)$), the following set of five linear equations is obtained.

$$[A]^1[\Delta s]^1 = [B]^1 \text{ or } \begin{bmatrix} A_{11}A_{12}A_{13}A_{14}A_{15} \\ A_{21}A_{22}A_{23}A_{24}A_{25} \\ A_{31}A_{32}A_{33}A_{34}A_{35} \\ A_{41}A_{42}A_{43}A_{44}A_{45} \\ A_{51}A_{52}A_{53}A_{54}A_{55} \end{bmatrix}^1 \cdot \begin{bmatrix} \Delta a_0 \\ \Delta a_1 \\ \Delta a_2 \\ \Delta b_0 \\ \Delta b_2 \end{bmatrix}^1 = \begin{bmatrix} B_1 \\ B_2 \\ B_3 \\ B_4 \\ B_5 \end{bmatrix}^1 \qquad \begin{matrix} (2.22) \\ (ref\,\mathrm{A.c.}14) \end{matrix}$$

where the definition of each of the A_{ij} coefficients is given in APPENDIX A, and superscript 1 refers to iteration 1. Solving the set of 5 linear equations, all the five coefficient changes are calculated at each iteration, then the updated coefficients are obtained. Equation (2.23) shows how the five coefficients' changes in iteration 1 ($\overrightarrow{\Delta s_1}$) is calculated first to update the initial coefficients ($\overrightarrow{s_0}$) to the coefficients in iteration 1 ($\overrightarrow{s_1}$).

$$[\Delta s]^1 = [[A]^1]^{-1}[B]^1 \rightarrow \overrightarrow{s_1} = \overrightarrow{s_0} + \overrightarrow{\Delta s_1} \qquad \begin{matrix} (2.23) \\ (ref\,\mathrm{A.c.}37) \end{matrix}$$

The new solution at each iteration $\overrightarrow{s_k}$ should be used to reduce the objective function Q_k to eventually find the minimum Q when the convergence criterion is satisfied. The maximum relative error of two consecutive solutions has been considered the predetermined convergence criterion to terminate the iteration loop. Although 1% is usually sufficient [31], 0.1 % is considered for this work as this has a minor effect on the computational expenses of the current algorithm. The optimization results given in chapter 4 along with the conformance between the results of proposed optimization and those of the fminsearch function illustrated in Figure 2.9, the considered convergence criterion looks sufficient. Then I_a as the best solution describes the intensity distribution can be found, and consequently, the ridge line can be achieved using already calculated a_i coefficients. The derivations of the analytic expression of the intensity distribution and the related equations can also be found in APPENDIX A.

2.1.2 Elliptical Ridge Line

In the case of sphere measurement, the ridge line profile is found to be an ellipse. The four first solution coefficients are defined by the ellipse parameters (center coordinates and diagonals), and the fifth and sixth coefficients are defined by the quadratic intensity coefficients as $\vec{s} = (x_0, y_0, a, b, b_0, b_2)$. In other words, the first four coefficients are determined using an elliptical fit to the initial solution of the ridge line, and the last two coefficients are determined using a quadratic fit to the initial solution of the intensity distribution of the first nonzero row. Plugging equation (2.24) into (2.3), the analytical model for the intensity of any arbitrary point (x, y) is found as $I_a(x, y)$ illustrated in equation (2.26). Following the same procedure as for the quadratic ridge lines, the distance function given in equation (2.27) is derived as a function of the solution coefficients (s_j) for any given point of sensor coordinates (x, y). Similarly, the objective function Q is defined to be optimized with respect to the six solution coefficients to achieve the best intensity distribution out of the measured sensor intensities. Having the best-fitted intensity distribution, the ridge line profile is then determined.

$$y_c(x) = s_2 + s_4\sqrt{1-\left(\frac{x_c - s_1}{s_3}\right)^2} \quad \begin{matrix}(2.24)\\ (ref\,\mathrm{A.d.1})\end{matrix}$$

$$\begin{pmatrix} x_{loc} \\ y_{loc} \end{pmatrix} = \begin{pmatrix} x_c \\ y - y_c \end{pmatrix} \quad \begin{matrix}(2.25)\\ (ref\,\mathrm{A.d.2})\end{matrix}$$

$$I_a(x, y) = s_5 - s_6\left(y - s_2 - s_4\sqrt{1-\left(\frac{x - s_1}{s_3}\right)^2}\right)^2 \quad \begin{matrix}(2.26)\\ (ref\,\mathrm{A.d.5})\end{matrix}$$

$$d_{i,k} = \left(s_{5,k-1} - I_{m,i}\right) - \left(s_{6,k-1}\right)\left(y_i - s_{2,k-1} - s_{4,k-1}\sqrt{1-\left(\frac{x_i - s_{1,k-1}}{s_{3,k-1}}\right)^2}\right)^2 \quad \begin{matrix}(2.27)\\ (ref\,\mathrm{A.d.7})\end{matrix}$$

$$Q_k = \sqrt{\sum_{i=1}^{n} {d_{i,k}}^2} \quad \begin{matrix}(2.28)\\ (ref\,\mathrm{A.d.8})\end{matrix}$$

Since Q in equation (2.28) is a non-linear function of the coefficients and the optimization process explained earlier, requiring the process of analytical expansion followed by a linearization process, is expensive in terms of potential numerical errors and computational time, another approach is taken in the case of sphere measurement. In this case, Q is numerically optimized using Matlab's "fminsearch" function to reach the best-fitted intensity distribution. To do this, Matlab code is developed to optimize the objective function and to obtain the s_j coefficients describing the ridge line profile. It is noteworthy to mention that in the earlier ridge line case, the results obtained from the already described optimization process are consistent with the results from the fminserach function, as shown in Figure 2.9, proving that the fminsearch function could be used as a powerful alternative in case of the complexity of the objective function.

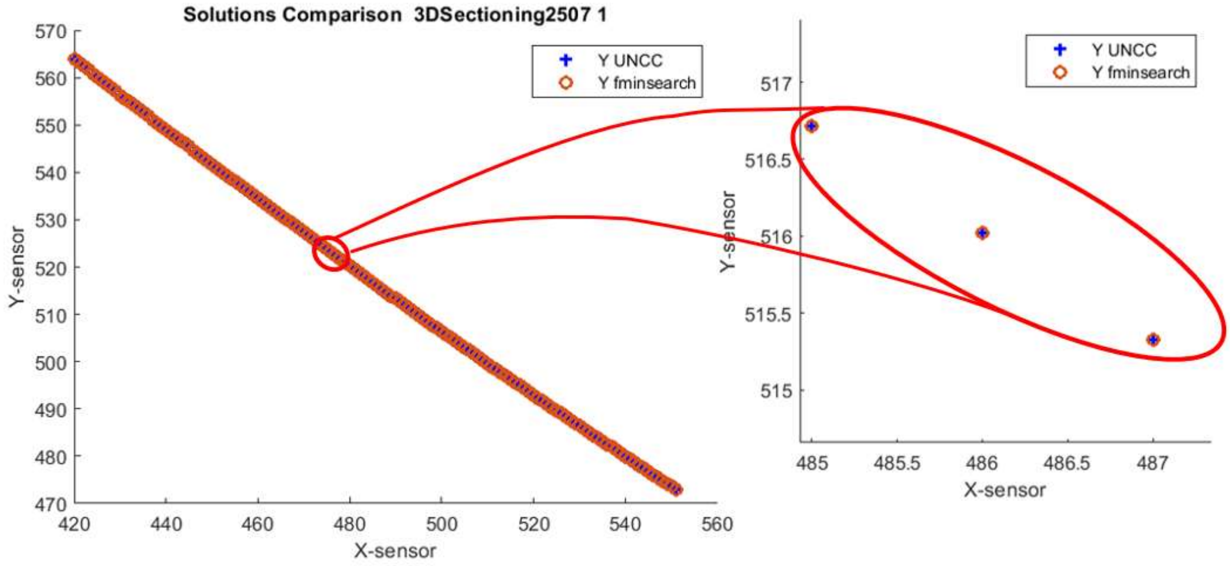

Figure 2.9: UNCC Optimization vs. fminsearch function for cylinder measurement

A MATLAB code comprised of several sections has been developed to take the sensor intensity matrix as the input and to perform the required calculations and the adjustments followed by the optimization process to achieve the optimized a_i coefficients describing the improved ridge line for every single frame.

2.2 Peak Detection Improvement

The method used to modify the peak detection position of the point cloud measured by the Nikon Instrument is explained below. Figure 2.10 depicts a high-level view of the process of modification. The steps involved in the process are outlined below. The machine generates two sets of information as the result of measuring a target profile; `dat` files, which include sensor image data, and a `lin` file which includes peak detection positions along with the corresponding addresses. The lin file includes the peak detection position of every line (row) in every scanned sensor frame in a binary form. Software provided by Nikon can convert the dat files into TIFF files for image processing. The converted TIFF files are then converted to text files; each text file includes the sensor image data of one scanned frame.

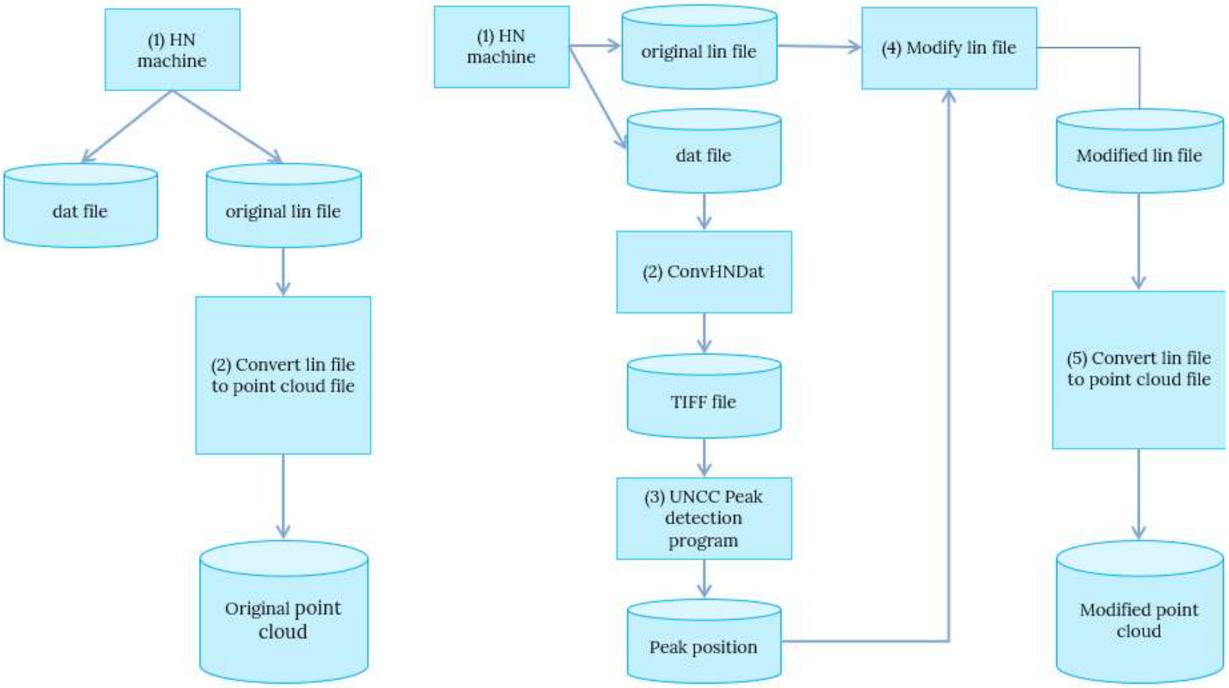

(a) Original Nikon process (b) Proposed process

Figure 2.10: Original and proposed peak detection process

The sensor image data in the text file format is then fed into the UNCC algorithm to find the modified peak positions. Based on the lin file structure, in which peak positions and the corresponding addresses are saved in a binary format, the algorithm also generates the corresponding addresses to be later used during the replacement process so that each original peak position is exactly replaced with the modified peak position belonging to the same address. The replacement is done by another software provided by Nikon to achieve a modified lin file. Eventually, the modified lin file is converted to the modified point clouds in the machine coordinate system through another Nikon software.

Depending on the length to be scanned, the number of frames generated by the Nikon instrument varies as the machine capturing frequency, the so-called "Pitch Value" in the supporting metrology software, is set by default to 20 microns per frame. For instance, 1000 frames would be generated by the instrument once a length of 20 millimeters is supposed to be scanned. Pitch value specifies the pitch value of the point cloud data to be obtained to change the scan speed. The smaller the pitch value is set in the metrology software, the slower the scan will be performed. A recommended pitch value ranges from 0.02mm to 0.05mm.

2.2.1 UNCC Algorithm for Peak Detection Improvement

In this section, the general outline of the UNCC algorithm is explained. The algorithm includes various parts, each of which is designed to add a capability to the algorithm. These parts are listed below.

1. Define unique measurement parameters
2. Import text files
3. Match the modified lin file with the original lin file
4. Remove multiple light reflection
5. Make segments and integrate them for optimization considering the intensity positions
6. Normalize over each row
7. Crop the window to remove initial minor peaks
8. Find the initial solution for optimization
9. Perform optimization
10. Calibrate the sensor to compensate for the sensor errors numerically
11. Generate the corresponding address for each peak position
12. Find the original Nikon solution and compare it with the algorithm's solution

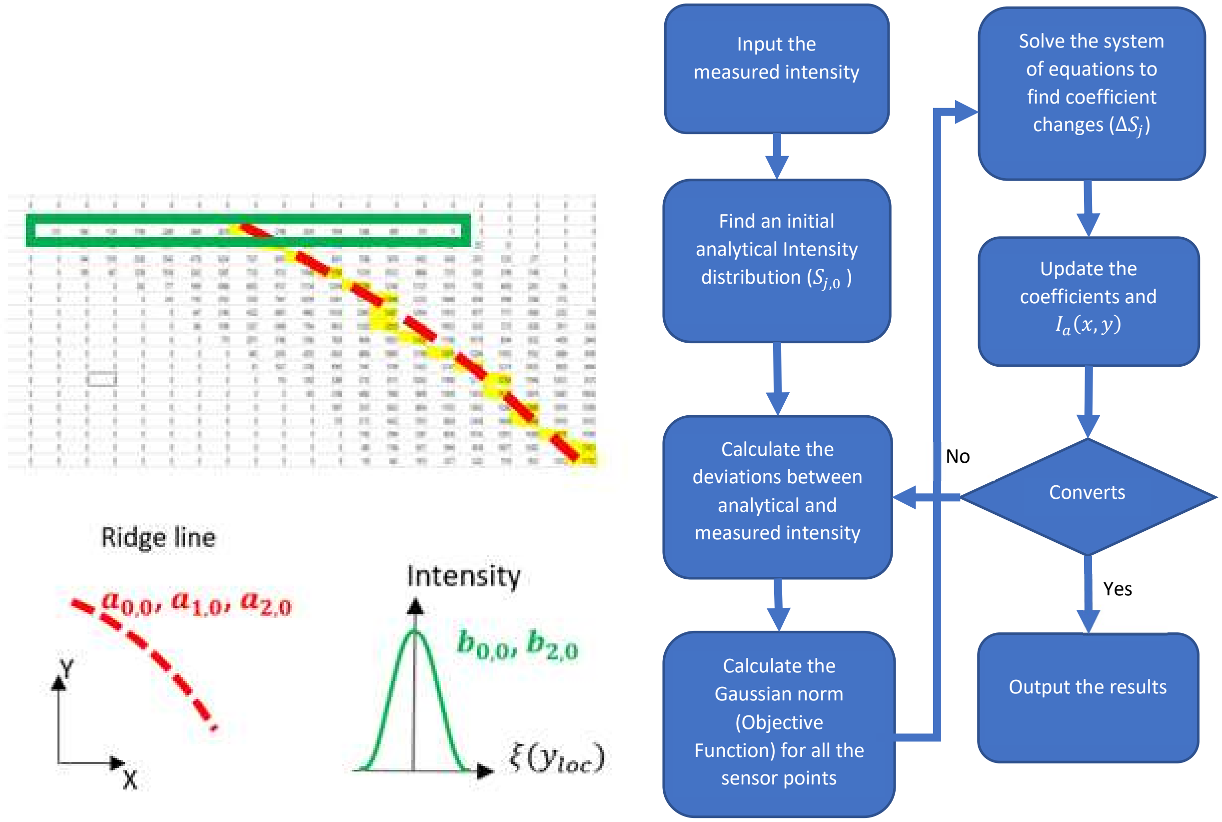

Figure 2.11: Algorithm for peak detection improvement

It is worth noting here the structure of sensor image data before discussing the different parts of the algorithm. As can be seen from Figure 2.12, there are zero intensity lines or void lines (depicted in orange) and nonzero intensity lines with a band of nonzero intensity elements (depicted in blue frame) surrounded by zero intensity elements (depicted in red frame) in each frame. One section of a converted text file, including light intensities, has been demonstrated in Figure 2.12. The maximum intensity of each line is highlighted in yellow. The highlighted profile across the entire sensor frame can represent a very rough estimation of the ridge line of this sensor frame illustrated in the dashed red line. Nikon follows a row-by-row approach to find the peak position. They go through every single line independent of the following line, find each line's individual peak position using a mathematical method, and consider each line and its peak position to generate measured points. That's why the measured profile by the original algorithm is non-uniform. Since the measured surface is a finished surface, a more or less uniform ridge line and therefore a uniform measured profile is expected.

In addition to the structure of sensor images, the general structure of lin files is essential to be discussed as the modified peak positions must sit exactly at their corresponding addresses in the original lin file to form the modified one. Every line of a sensor frame has a unique address in the lin file, which is attributed to its corresponding peak position value in a binary format, as illustrated in Figure 2.13.

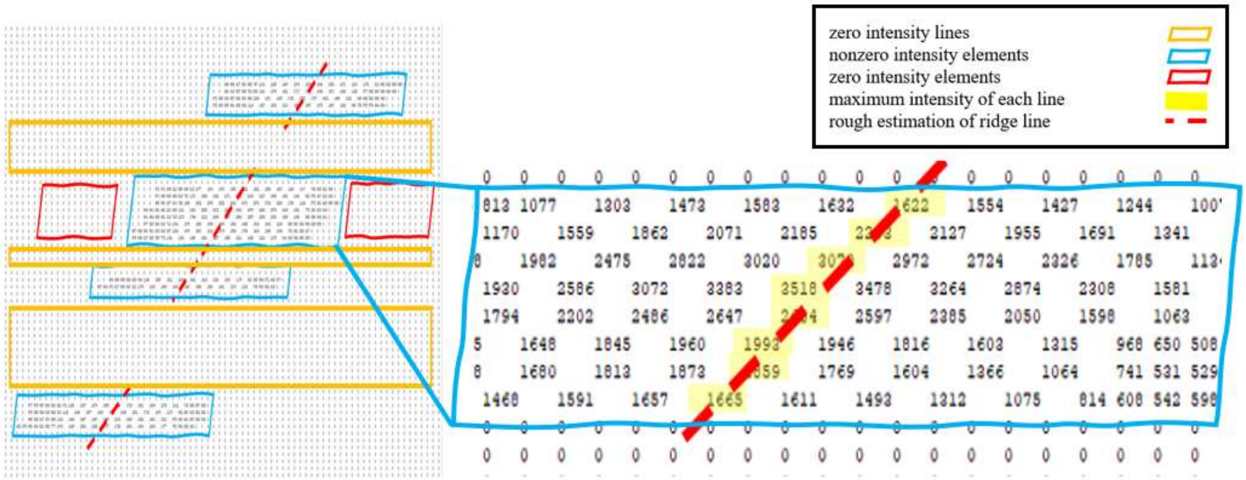

Figure 2.12: Sensor image data vs Ridge line

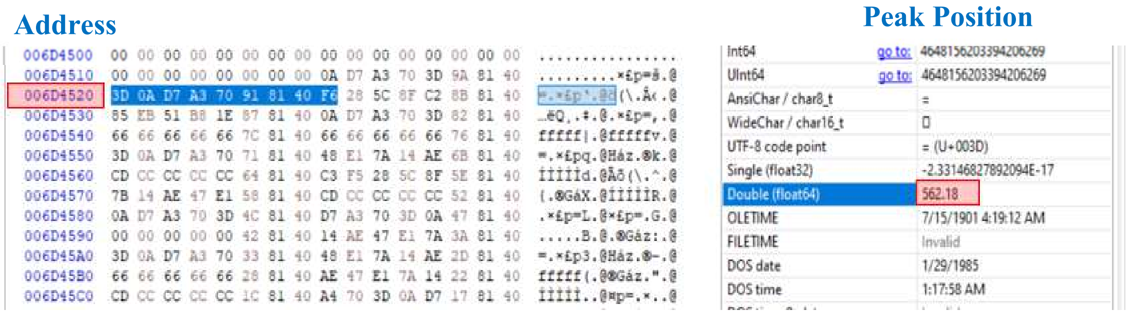

```
006D4500  00 00 00 00 00 00 00 00 00 00 00 00 00 00 00 00  ................
006D4510  00 00 00 00 00 00 00 00 0A D7 A3 70 3D 9A 81 40  .........×£p=š.@
006D4520  3D 0A D7 A3 70 91 81 40 F6 28 5C 8F C2 8B 81 40  =.×£p'.@ö(\.Â‹.@
006D4530  85 EB 51 B8 1E 87 81 40 0A D7 A3 70 3D 82 81 40  …ëQ¸.‡.@.×£p=‚.@
006D4540  66 66 66 66 66 7C 81 40 66 66 66 66 66 76 81 40  fffff|.@fffffv.@
006D4550  3D 0A D7 A3 70 71 81 40 48 E1 7A 14 AE 6B 81 40  =.×£pq.@Ház.®k.@
006D4560  CD CC CC CC CC 64 81 40 C3 F5 28 5C 8F 5E 81 40  ÍÌÌÌÌd.@Ãõ(\.^.@
006D4570  7B 14 AE 47 E1 58 81 40 CD CC CC CC CC 52 81 40  {.®GáX.@ÍÌÌÌÌR.@
006D4580  0A D7 A3 70 3D 4C 81 40 D7 A3 70 3D 0A 47 81 40  .×£p=L.@×£p=.G.@
006D4590  00 00 00 00 00 42 81 40 14 AE 47 E1 7A 3A 81 40  .....B.@.®Gáz:.@
006D45A0  3D 0A D7 A3 70 33 81 40 48 E1 7A 14 AE 2D 81 40  =.×£p3.@Ház.®-.@
006D45B0  66 66 66 66 66 28 81 40 AE 47 E1 7A 14 22 81 40  fffff(.@®Gáz.".@
006D45C0  CD CC CC CC CC 1C 81 40 A4 70 3D 0A D7 17 81 40  ÍÌÌÌÌ..@¤p=.×..@
```

```
Int64                go to:  4648156203394206269
UInt64               go to:  4648156203394206269
AnsiChar / char8_t           =
WideChar / char16_t          ▯
UTF-8 code point             = (U+003D)
Single (float32)             -2.33146827892094E-17
Double (float64)             562.18
OLETIME                      7/15/1901 4:19:12 AM
FILETIME                     Invalid
DOS date                     1/29/1985
DOS time                     1:17:58 AM
```

Figure 2.13: Lin file structure

In the first part of the algorithm, the unique parameters of measurement, including the index of the essential input files (sensor files and the line file), are defined for the algorithm. This would help the algorithm to load and read the input files automatically.

The next section is designed to import the input files, and to save the associate data on the corresponding variables. Comparing the modified lin file with the original line file created by the instrument, there seems to be filtering performed by the company algorithm that excludes the peak position of some lines from the lin file. Since the eliminated lines are more related to the beginning and ending of nonzero lines of a frame, there might be a threshold defined for their algorithm to exclude the intensities below the predefined threshold that cannot form precise point clouds later.

In the third part, a list of peak positions of each frame is extracted from the original lin file, and the index of void lines is detected. Then lines with the same index are set to zero in the imported sensor file to match the sensor files with the original lin file in terms of the void lines. In other words, not removing those lines from the imported sensor file will later lead to extra peak positions in the modified lin file and, thus, extra points in the modified point clouds. Every nonzero-intensity line corresponds to a peak position value and a measured point in the XYZ coordinate system. If the modified lin file is not matched with the original one, it would significantly affect the total number of modified point clouds compared to the original ones.

Then, in the fourth part, intensities out of the primary band intensity, depicted in orange in Figure 2.14, are detected as multiple light reflection effects and are removed to avoid false surface detection. Multiple light reflection has always been a major challenge in optical metrology, especially in the case of shiny surfaces and small geometrical features such as tiny deep grooves or deep tooth gears. Access to the sensor file and detecting multiple light reflection effects in this dissertation offer one effective way to resolve this issue.

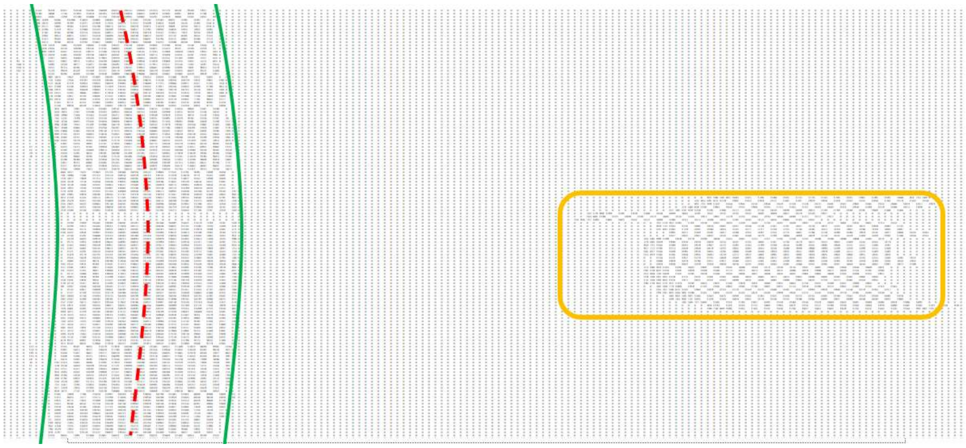

Figure 2.14: Multiple light reflections in sensor frame

As can be seen from Figure 2.12, the primary band intensity may include several segments of nonzero lines. They need to be separately detected to be considered in the optimization process to detect the ridge line. Although they are separated, they must be integrated and used in the optimization process. These all are performed in the fifth part of the algorithm.

As the algorithm's objective is to detect the ridge line, the peak position matters. In other words, the three a_i coefficients in the case of a quadratic ridge line, or the 1st four s_j coefficients in the case of an elliptical ridge line, which describe a ridge line profile, are the actual output of the optimization process and the b_i coefficients, which describe the intensity profile across each row (intensity peak values and the intensity base width) are just used to run the optimization. Having said that, the ridge line coefficients (a_i or the 1st four s_j coefficients) must be calculated independent of the intensity peak values and the optimization process must be isolated from the intensity peak values. Hence, the effect of various peak values across the sensor frame from line to line must be avoided. To do that, each frame is normalized by dividing the intensity values of each line by the maximum intensity value of that line so that the maximum intensity value of all lines is 1.

Another modification considered in the algorithm is the effect of minor peaks at each line's beginning and end. Looking at each nonzero intensity line, the intensity values often start from zero then rise to a minor peak and fall into a lower value followed by a sudden rise and reach a major peak. This approximately symmetric shape around the central peak can be observed in almost all lines. Minor peaks can cause a severe problem when the optimization falls into a local minimum instead of the global minimum, leading to false peak detection and, therefore, a wrong ridge line. In this section, the primary band intensity is cropped, and a tighter window excluding minor peaks is used for the optimization. Depending on the investigated geometries followed by the optimization results, a 15-pixel window is considered for the geometries with quadratic ridge line, i.e., flat surface, cylinder, and gear, and an 11-pixel window is considered for the geometries with the elliptical ridge line. The above-mentioned window's width is found based on the results of the optimization process for various sensor frames of each geometry measurement. Here, two criteria are considered for determining the width: a visual and numerical comparison using the objective function value. First, by visually comparing the shape of the optimized ridge line profile with the original ridge line profile. Second, by checking the objective function value. Since the number of the evaluated pixels varies as the window width varies, and the objective function values changes as the number of evaluated pixels changes, the objective function criterion alone does not suffice.

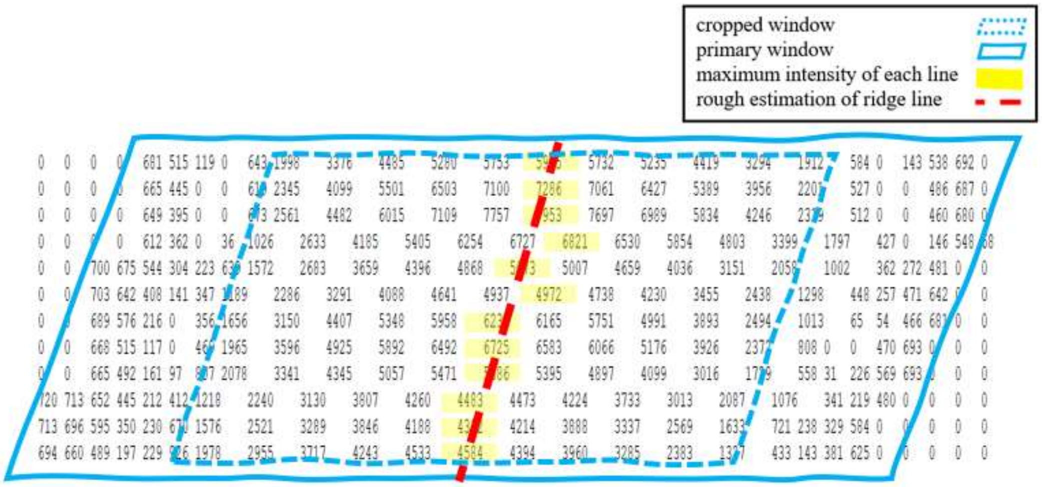

```
0 0 0 0 681 515 119 0 643 1998 3376 4485 5280 5753 [illegible] 5732 5235 4419 3294 1912 584 0 143 538 692 0
0 0 0 0 665 445 0 0 [illegible] 2345 4099 5501 6503 7100 7286 7061 6427 5389 3956 2201 527 0 0 486 687 0
0 0 0 0 649 395 0 0 673 2561 4482 6015 7109 7757 7953 7697 6989 5834 4246 2379 512 0 0 460 680 0
0 0 0 0 612 362 0 36 1026 2633 4185 5405 6254 6727 6821 6530 5854 4803 3399 1797 427 0 146 548 [illegible]
0 0 700 675 544 304 223 [illegible] 1572 2683 3659 4396 4868 [illegible] 5007 4659 4036 3151 [illegible] 1002 362 272 481 0 0
0 0 703 642 408 141 347 1189 2286 3291 4088 4641 4937 4972 4738 4230 3455 2438 1298 448 257 471 642 0 0
0 0 689 576 216 0 356 1656 3150 4407 5348 5958 [illegible] 6165 5751 4991 3893 2494 1013 65 54 466 681 0 0
0 0 668 515 117 0 469 1965 3596 4925 5892 6492 6725 6583 6066 5176 3926 2377 808 0 0 470 693 0 0 0
0 0 665 492 161 97 [illegible] 2078 3341 4345 5057 5471 [illegible] 5395 4897 4099 3016 1779 558 31 226 569 693 0 0 0
720 713 652 445 212 412 1218 2240 3130 3807 4260 4483 4473 4224 3733 3013 2087 1076 341 219 480 0 0 0 0 0
713 696 595 350 230 670 1576 2521 3289 3846 4188 [illegible] 4214 3888 3337 2569 1633 721 238 329 584 0 0 0 0 0
694 660 489 197 229 926 1978 2955 3717 4243 4533 4584 4394 3960 3285 2383 1377 433 143 381 625 0 0 0 0 0
```

Figure 2.15: Cropped sensor data for the optimization

The eighth part of the algorithm is devoted to finding an initial solution to start the optimization with. As mentioned earlier in sections 2.1.1 and 2.1.2, there are two sets of coefficients; one to describe the ridge line profile and one to describe the bell-shaped intensity distribution. An initial solution for the first set is obtained by developing a quadratic polynomial regression to find the initial ridge line coefficients for each sensor frame by finding the locations of the arrays with the highest intensities in the X-Y sensor coordinates, as shown in Figures 2.11 and 2.12. The second set's initial values are then found using another quadratic polynomial regression on the first nonzero-intensity row of the same sensor frame. Having an initial solution $s_{j,0}$, the iterations can then be started.

The next and most crucial part is the implementation of the optimization process, the mathematics of which is explained in detail in sections 2.1.1 and 2.1.2.

One of the advantages of the proposed algorithm is the calibration part which includes a 2-step process. First, the algorithm should run and drive the modified point clouds. In the second step, the modified point clouds are compared with the original point cloud to eventually find the numerical sensor calibration for the measured geometry. This calibration can later be used in the algorithm to compensate for the noncalibrated sensor effects. The deviations between the modified point clouds driven from the algorithm and the original point clouds are calculated in the calibration part. Then there is a common polynomial in the deviations of all frames when seen in the same plot. Subtracting the calculated deviation from the common term, residual deviations can be obtained that all follow a similar trend across various frames. The mean value of the residuals in the sensor coordinate system gives the calibration values in the sensor domain. As discussed in Chapter 4, the deviation in the sensor domain is linearly commensurate with the deviations in the point cloud coordinates system with a linear coefficient. Considering the linear conversion coefficients, the sensor calibration can be converted from the sensor domain into the machine coordinate system. The calibration of different geometries will be comprehensively discussed later in Chapter 5.

To be able to modify the original lin file, not only the modified peak positions should be identified, but also the corresponding addresses should be generated so that each original peak position can be replaced with the corresponding modified peak position belonging to the same address. The generation of the corresponding addresses and assigning each modified peak position to the correct address is performed in the next part of the algorithm.

In the algorithm’s last part, original peak positions are driven from an original lin file to allow the user to compare peak positions between modified and original values. This can give one an idea of what change the UNCC algorithm can make in the sensor domain compared to the original Nikon method, as illustrated in Figure 2.16. The comparison in the sensor domain will be discussed in detail in Chapter 4.

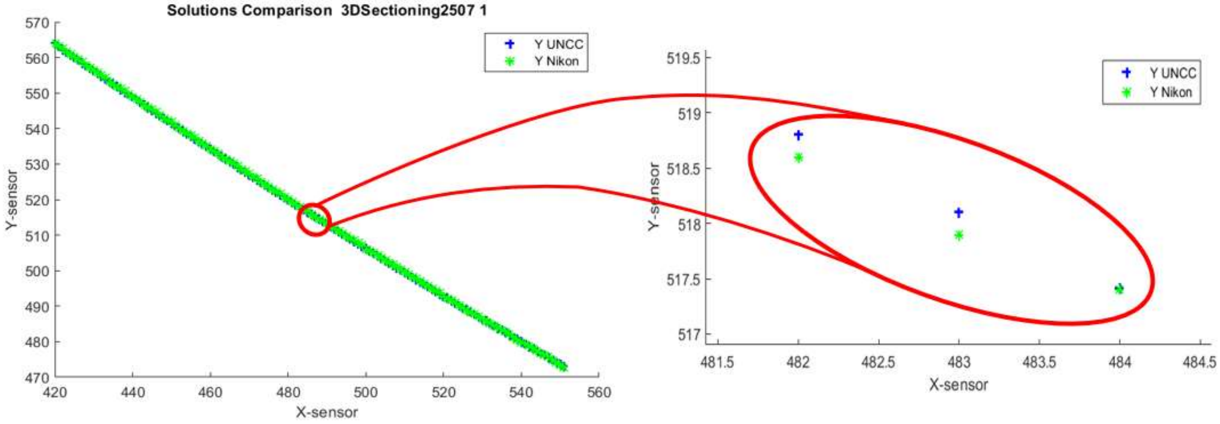

Figure 2.16: UNCC solution vs. Nikon solution in cylinder measurement

3 CHAPTER 3: EVALUATION WITH SIMULATED DATA

This chapter assesses the UNCC algorithm performance using four sets of simulated data. A 3D light intensity distribution of a sensor frame is simulated using a quadratic and an elliptical ridge line profile. For each ridge line profile, one quadratic and one exponential profile is considered to simulate the bell-shaped light intensity distribution over each line of a sensor frame. First, the 3D light intensity distribution is simulated using known coefficient values. The known coefficients are comprised of three a_i coefficients in the case of the quadratic ridge line, or the 1st four s_j coefficients in the case of the elliptical ridge line, to describe a ridge line profile and two b_i coefficients to describe the peak values and the bandwidth, as described earlier in Chapter 2. Then, the simulated light intensity is fed to the UNCC algorithm in each of the four cases to perform an optimization to iteratively find the corresponding ridge line profile. Then the simulation coefficients are compared to the UNCC solution to evaluate the UNCC algorithm.

3.1 Quadratic Ridge Line

An iterative optimization is developed based on the previously mentioned set of five linear equations and then tested for both the exponential and the quadratic simulated data, as seen in Figures 3.1 and 3.2. The algorithm can perfectly find the expected ridge line for both sets of simulation data.

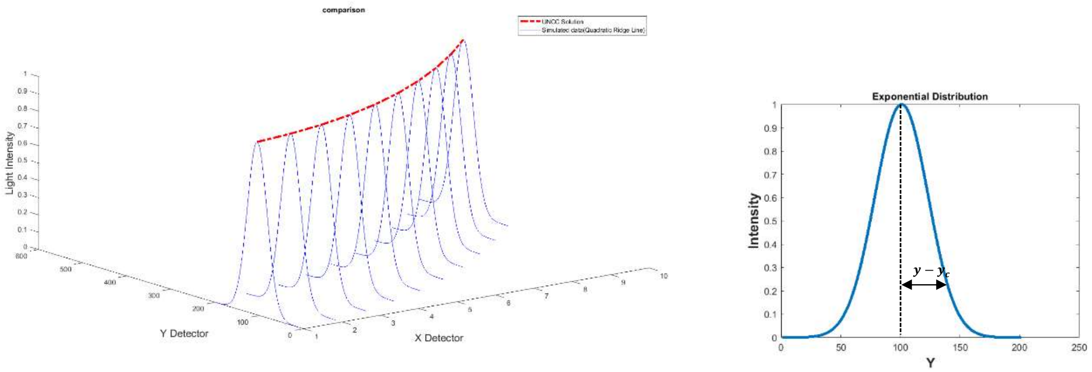

Figure 3.1: Simulation Data vs. the algorithm solution for exponential distribution

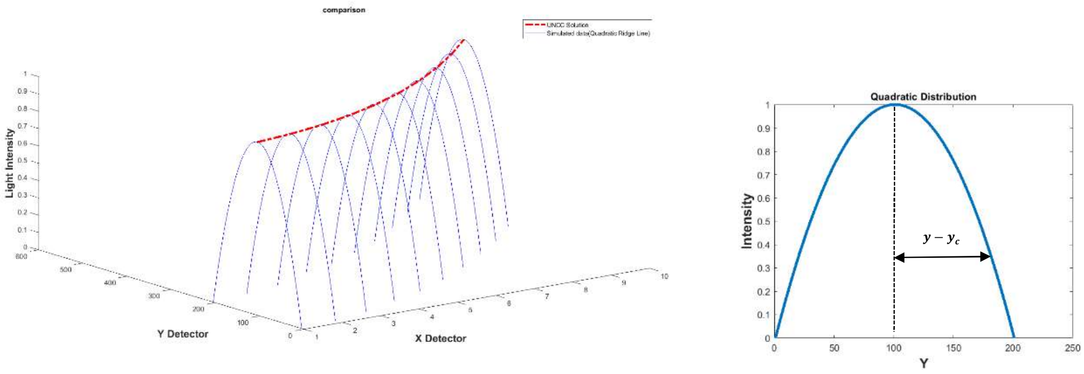

Figure 3.2: Simulation Data vs. the algorithm solution for quadratic distribution

Below, two examples of the simulated data and a comparison of the results are given to show how accurately the algorithm can converge to the a_i simulated coefficients. In the first example, the intensity along the y direction is simulated using an exponential function, while in the second one, a quadratic polynomial is used to simulate the intensities along the y direction. As seen from the simulation coefficients and the final solution, the algorithm would perfectly approach the same values for the three first simulation coefficients, which describe the ridge line (a_0, a_1, a_2).

3.1.1 Simulation Based on Exponential Distribution of the Intensities over Each Row

$$y_c(x) = a_0 + a_1 x_c + a_2 {x_c}^2 \qquad 14$$

$$I_a(x, y, x_c, y_c) = b_0 e^{-b_2 (y - y_c)^2} \qquad 15$$

Table 3.1: Coefficients describing exponential distribution of the intensities over each row for quadratic ridge line

Simulation Coefficients	$\overline{\boldsymbol{a_0}}$	$\overline{\boldsymbol{a_1}}$	$\overline{\boldsymbol{a_2}}$	$\overline{\boldsymbol{b_0}}$	$\overline{\boldsymbol{b_2}}$
	100	2	3	10	0.001
Start Solution	$\boldsymbol{a_{0,0}}$	$\boldsymbol{a_{1,0}}$	$\boldsymbol{a_{2,0}}$	$\boldsymbol{b_{0,0}}$	$\boldsymbol{b_{2,0}}$
	120	0	3.5	5	0.005
Final Solution	$\boldsymbol{a_{0,f}}$	$\boldsymbol{a_{1,f}}$	$\boldsymbol{a_{2,f}}$	$\boldsymbol{b_{0,f}}$	$\boldsymbol{b_{2,f}}$
	100.000	2.000	3.000	5.757	0.001

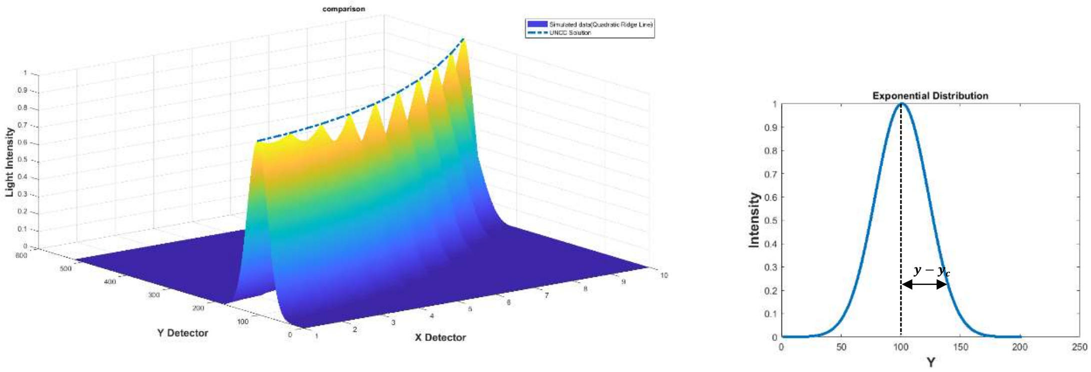

Figure 3.3: Simulation Data vs. the algorithm solution

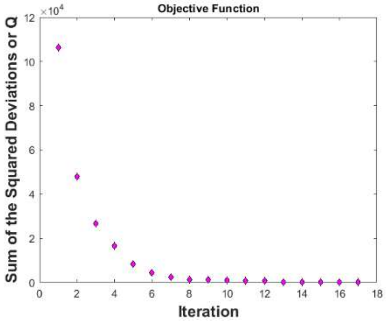

Figure 3.4: Objective function vs. iteration number

3.1.2 Simulation Based on Quadratic Distribution of the Intensities over Each Row

$$y_c(x) = a_0 + a_1 x_c + a_2 {x_c}^2 \tag{16}$$

$$I_a(x, y, x_c, y_c) = b_0 - b_2 (y - y_c)^2 \tag{17}$$

Table 3.2: Coefficients describing quadratic distribution of the intensities over each row for quadratic ridge line

Simulation Coefficients	$\overline{a_0}$	$\overline{a_1}$	$\overline{a_2}$	$\overline{b_0}$	$\overline{b_2}$
	100	2	3	10	0.001
Start Solution	$a_{0,0}$	$a_{1,0}$	$a_{2,0}$	$b_{0,0}$	$b_{2,0}$
	120	0	3.5	9	0.005
Final Solution	$a_{0,f}$	$a_{1,f}$	$a_{2,f}$	$b_{0,f}$	$b_{2,f}$
	100.0000	2.0000	3.0000	10.0000	0.0010

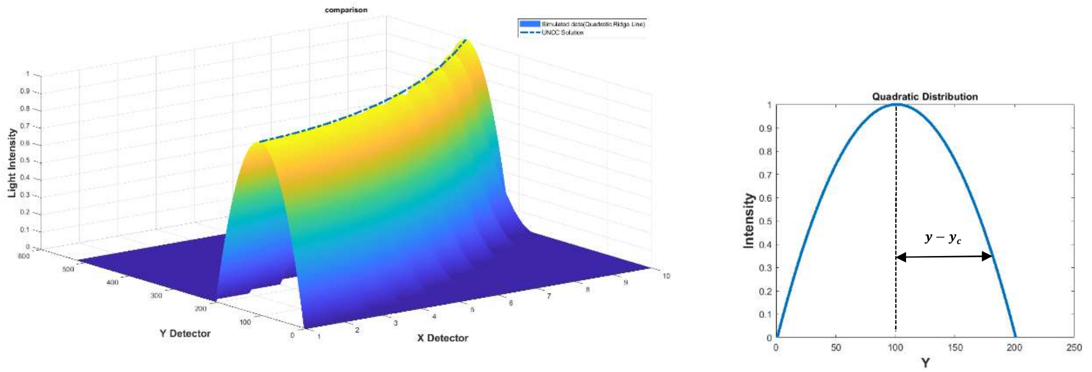

Figure 3.5: Simulation Data vs. the algorithm solution

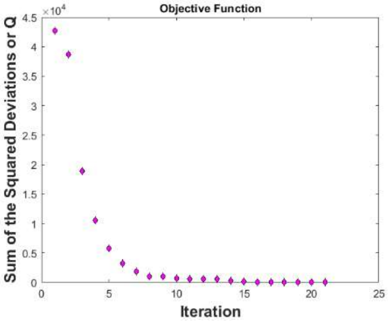

Figure 3.6: Objective function vs. iteration number

3.2 Elliptical Ridge Line

In the optimization stage of elliptical ridge line simulation, due to the highly nonlinear nature of the intensity equations caused by complicated elliptical equation, the MATLAB fminsearch function is used for both the exponential and the quadratic simulated data. Again, the algorithm can perfectly find the expected ridge line for both sets of simulation data, as shown in Figures 3.7 and 3.8.

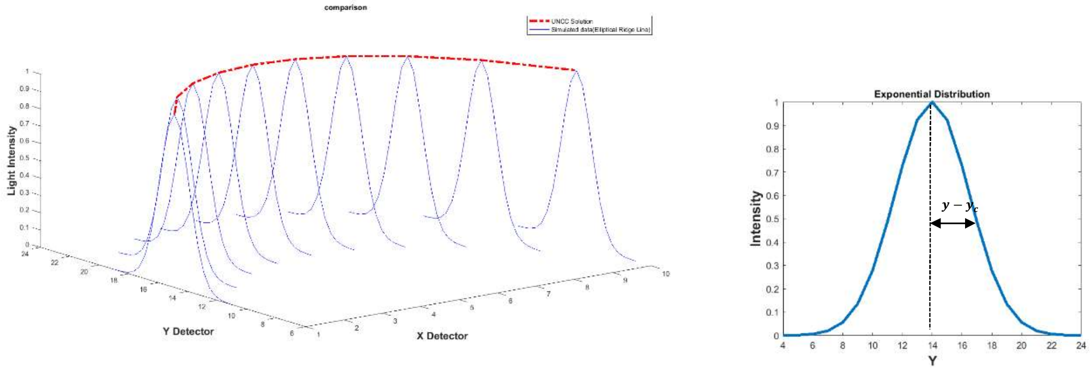

Figure 3.7: Simulation Data vs. the algorithm solution for exponential distribution

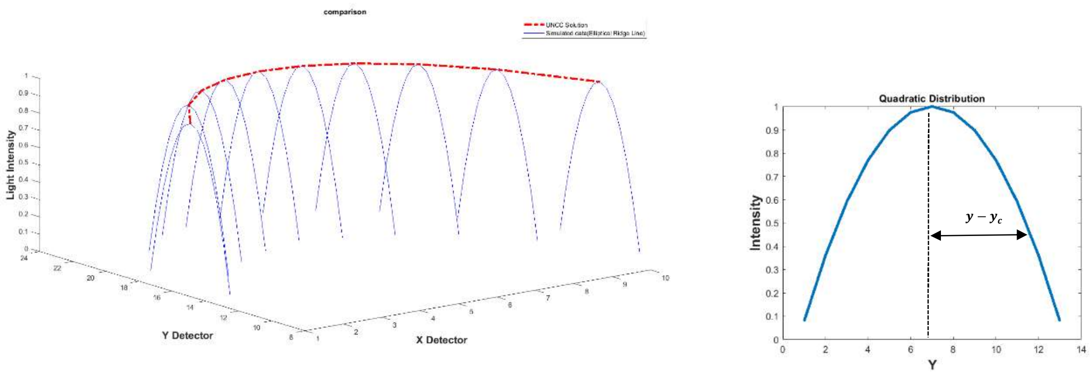

Figure 3.8: Simulation Data vs. the algorithm solution for quadratic distribution

3.2.1 Simulation Based on Exponential Distribution of the Intensities over Each Row

$$y_c(x) = s_2 + s_4\sqrt{1 - \left(\frac{x_c - s_1}{s_3}\right)^2} \tag{18}$$

$$I_a(x, y, x_c, y_c) = s_5\, e^{-s_6(y-y_c)^2} \tag{19}$$

Table 3.3: Coefficients describing exponential distribution of the intensities over each row for elliptical ridge line

Simulation Coefficients	$\overline{x_0}$	$\overline{y_0}$	$\overline{a}$	$\overline{b}$	$\overline{b_0}$	$\overline{b_2}$
	5.0	0.0	6.0	20.0	10.0	0.5
Start Solution	$x_{0,0}$	$y_{0,0}$	a_0	b_0	$b_{0,0}$	$b_{2,0}$
	4.0	0.0	10	17.0	-10	0.1
Final Solution	$x_{0,f}$	$y_{0,f}$	a_f	b_f	$b_{0,f}$	$b_{2,f}$
	5.000	-0.004	6.001	20.005	6.100	0.531

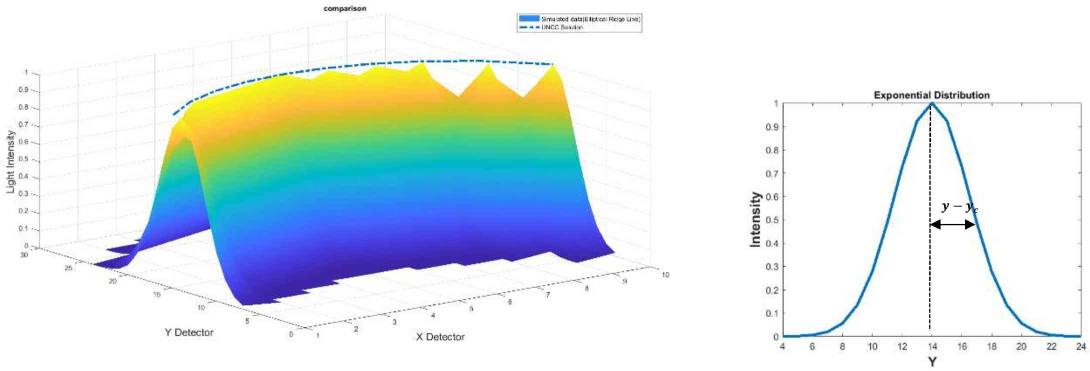

Figure 3.9: Simulation Data vs. the algorithm solution

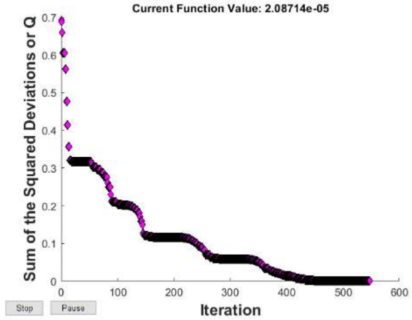

Figure 3.10: Objective function vs. iteration number

3.2.2 Simulation Based on Quadratic Distribution of the Intensities over Each Row

$$y_c(x) = s_2 + s_4\sqrt{1-\left(\frac{x_c - s_1}{s_3}\right)^2} \tag{20}$$

$$I_a(x, y, x_c, y_c) = s_5 - s_6(y - y_c)^2 \tag{21}$$

Table 3.4: Coefficients describing quadratic distribution of the intensities over each row for elliptical ridge line

Simulation Coefficients	$\overline{x_0}$	$\overline{y_0}$	$\overline{a}$	$\overline{b}$	$\overline{b_0}$	$\overline{b_2}$
	5.0	0.0	6.0	20.0	10.0	1.6
Start Solution	$x_{0,0}$	$y_{0,0}$	a_0	b_0	$b_{0,0}$	$b_{2,0}$
	4.0	0.0	10	19.0	-10	1.3
Final Solution	$x_{0,f}$	$y_{0,f}$	a_f	b_f	$b_{0,f}$	$b_{2,f}$
	5.0	0.0	6.0	20.0	10.0	1.6

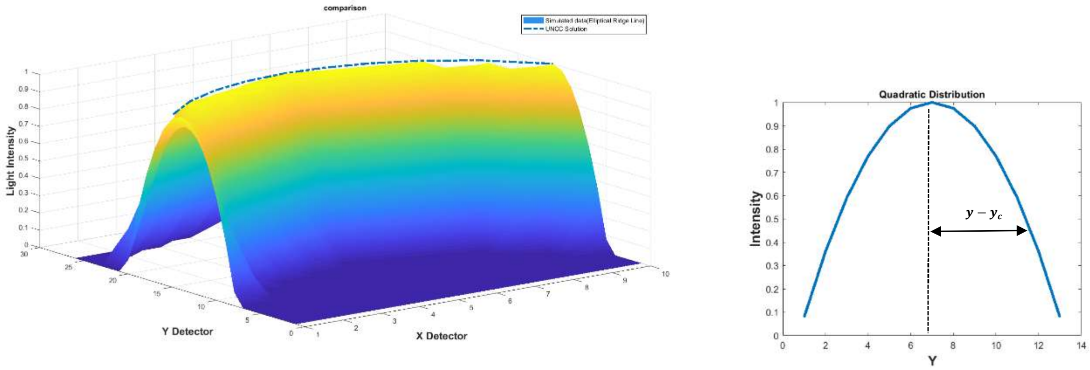

Figure 3.11: Simulation Data vs. the algorithm solution

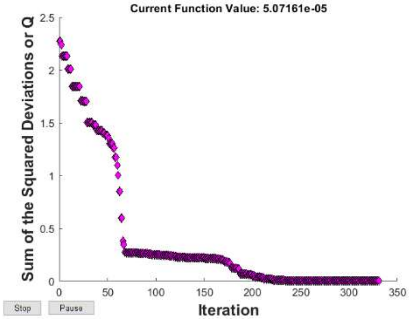

Figure 3.12: Objective function vs. iteration number

The above results show that the algorithm can converge the simulated data in both the exponential and the quadratic cases. Since working with the quadratic polynomial can save computational time, as shown in Figures 3.10 and 3.12, while not affecting the algorithm convergence, the quadratic polynomial will be used for the actual sensor data.

4 CHAPTER 4: IMPLEMENTATION OF ALGORITHM ON ACTUAL SENSOR DATA

Following the successful algorithm's performance on the simulated data shown in Chapter 3, the current chapter explains how the peak detection algorithm is applied to the actual sensor data for all the measured references in this dissertation, i.e., flat surface, cylinder, sphere, and helical cylindrical gear. The modified peak positions are then calculated to be compared with the peak positions extracted from the original Nikon peak detection algorithm. Since the triangulation method is used in the measurement process, any peak position deflection in the sensor X-Y direction leads to a deviation in the evaluated distance and, therefore, an inaccurate measured points cloud. To establish a correlation between the deviations in the sensor coordinate system and the machine XYZ coordinate system, a measurement is performed and the data in both coordinate systems are compared. This correlation can give one a rough estimation of how the peak detection modifications in the sensor domain can improve the measurement accuracy in the YXZ coordinate system. In the last section, a numerical comparison is performed between the UNCC and the Nikon peak detection algorithms for the same input sensor frame.

4.1 Preprocessing for Actual Sensor Data

Recalling from Chapter 2, sensor data includes multiple sensor frames, each of which consists of 1024 rows (lines), each of which consists of 1024 elements. Therefore, the intensities of each sensor frame form a 1024×1024 matrix, as the machine laser scanner is equipped with a 1024×1024-pixel CCD camera. As explained in section 2.2.1 and shown in Figures 2.12 and 2.15, there can exist a primary intensity band of nonzero-intensity lines, serval zero-intensity lines, and zero-intensity elements around the primary band in each sensor frame. The primary band may include several segments of nonzero-intensity lines. Furthermore, since the transposed intensity matrix of sensor frames is used in this chapter, zero-intensity lines are referred to as void columns.

Initially, the raw sensor frame needs to be preprocessed to be used as the input of the proposed peak detection algorithm. First, the sensor frame is rearranged so the algorithm can be applied. In other words, the intensity values are not changed at all, but the primary intensity band is rearranged. Since there are some void columns in the sensor frame, as shown in Figure 4.1, the capability to find the location of the void columns is also added to the algorithm so that the sensor frame would be divided into several continuous segments, each of which has no void columns.

An effort is made to make simulation data very similar to the actual sensor frame (with many non-intensity arrays around the primary intensity band as the actual sensor frame looks like), and the algorithm is tested. The result shows that the solution does not always converge because of the non-intensity arrays. Then the actual sensor frame is modified so that the non-intensity arrays are removed and only an intensity band is kept. This way, the solution converges.

In the following, the above-mentioned method is used to rearrange the sensor frame and make the corresponding X and Y coordinates of the primary intensity band at each array, illustrated in Figures 4.1 to 4.3. It should be noted that the sensor frame is not changed at all; however, the primary intensity band is rearranged for the purpose of optimization convergence.

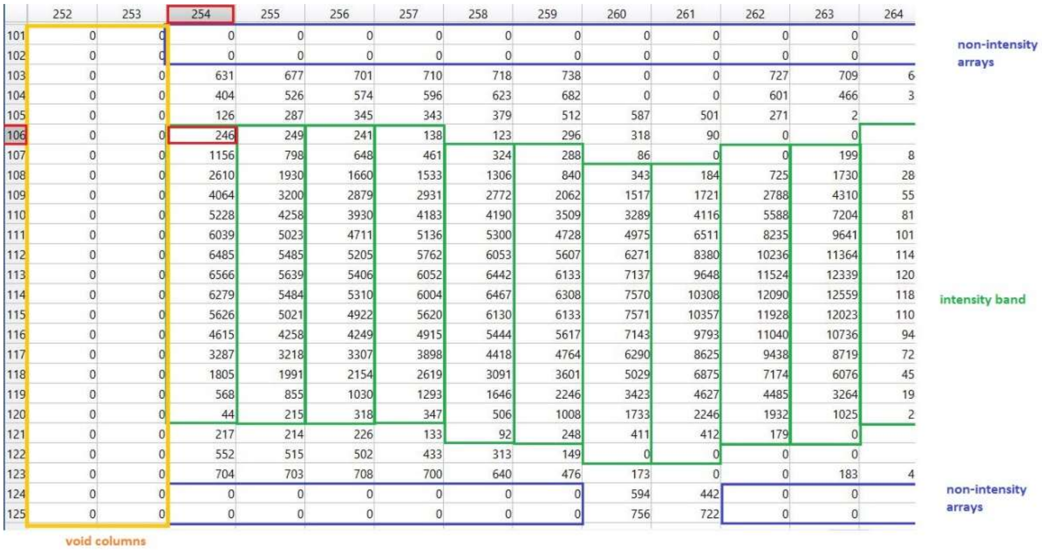

	252	253	254	255	256	257	258	259	260	261	262	263	264
101	0	0	0	0	0	0	0	0	0	0	0	0	
102	0	0	0	0	0	0	0	0	0	0	0	0	
103	0	0	631	677	701	710	718	738	0	0	727	709	6
104	0	0	404	526	574	596	623	682	0	0	601	466	3
105	0	0	126	287	345	343	379	512	587	501	271	2	
106	0	0	246	249	241	138	123	296	318	90	0	0	
107	0	0	1156	798	648	461	324	288	86	0	0	199	8
108	0	0	2610	1930	1660	1533	1306	840	343	184	725	1730	28
109	0	0	4064	3200	2879	2931	2772	2062	1517	1721	2788	4310	55
110	0	0	5228	4258	3930	4183	4190	3509	3289	4116	5588	7204	81
111	0	0	6039	5023	4711	5136	5300	4728	4975	6511	8235	9641	101
112	0	0	6485	5485	5205	5762	6053	5607	6271	8380	10236	11364	114
113	0	0	6566	5639	5406	6052	6442	6133	7137	9648	11524	12339	120
114	0	0	6279	5484	5310	6004	6467	6308	7570	10308	12090	12559	118
115	0	0	5626	5021	4922	5620	6130	6133	7571	10357	11928	12023	110
116	0	0	4615	4258	4249	4915	5444	5617	7143	9793	11040	10736	94
117	0	0	3287	3218	3307	3898	4418	4764	6290	8625	9438	8719	72
118	0	0	1805	1991	2154	2619	3091	3601	5029	6875	7174	6076	45
119	0	0	568	855	1030	1293	1646	2246	3423	4627	4485	3264	19
120	0	0	44	215	318	347	506	1008	1733	2246	1932	1025	2
121	0	0	217	214	226	133	92	248	411	412	179	0	
122	0	0	552	515	502	433	313	149	0	0	0	0	
123	0	0	704	703	708	700	640	476	173	0	0	183	4
124	0	0	0	0	0	0	0	0	594	442	0	0	
125	0	0	0	0	0	0	0	0	756	722	0	0	

Figure 4.1: Transposed sensor frame

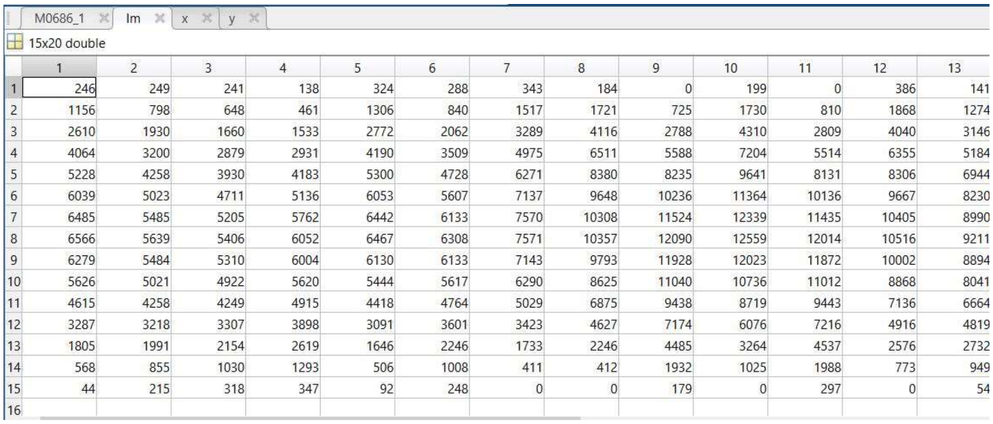

	1	2	3	4	5	6	7	8	9	10	11	12	13
1	246	249	241	138	324	288	343	184	0	199	0	386	141
2	1156	798	648	461	1306	840	1517	1721	725	1730	810	1868	1274
3	2610	1930	1660	1533	2772	2062	3289	4116	2788	4310	2809	4040	3146
4	4064	3200	2879	2931	4190	3509	4975	6511	5588	7204	5514	6355	5184
5	5228	4258	3930	4183	5300	4728	6271	8380	8235	9641	8131	8306	6944
6	6039	5023	4711	5136	6053	5607	7137	9648	10236	11364	10136	9667	8230
7	6485	5485	5205	5762	6442	6133	7570	10308	11524	12339	11435	10405	8990
8	6566	5639	5406	6052	6467	6308	7571	10357	12090	12559	12014	10516	9211
9	6279	5484	5310	6004	6130	6133	7143	9793	11928	12023	11872	10002	8894
10	5626	5021	4922	5620	5444	5617	6290	8625	11040	10736	11012	8868	8041
11	4615	4258	4249	4915	4418	4764	5029	6875	9438	8719	9443	7136	6664
12	3287	3218	3307	3898	3091	3601	3423	4627	7174	6076	7216	4916	4819
13	1805	1991	2154	2619	1646	2246	1733	2246	4485	3264	4537	2576	2732
14	568	855	1030	1293	506	1008	411	412	1932	1025	1988	773	949
15	44	215	318	347	92	248	0	0	179	0	297	0	54
16													

Figure 4.2: Rearranged intensity matrix

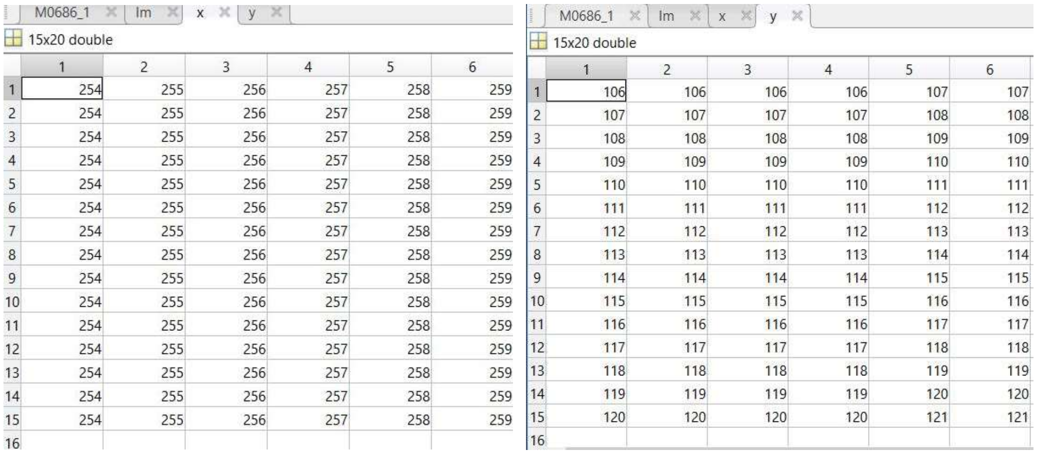

	1	2	3	4	5	6
1	254	255	256	257	258	259
2	254	255	256	257	258	259
3	254	255	256	257	258	259
4	254	255	256	257	258	259
5	254	255	256	257	258	259
6	254	255	256	257	258	259
7	254	255	256	257	258	259
8	254	255	256	257	258	259
9	254	255	256	257	258	259
10	254	255	256	257	258	259
11	254	255	256	257	258	259
12	254	255	256	257	258	259
13	254	255	256	257	258	259
14	254	255	256	257	258	259
15	254	255	256	257	258	259
16						

	1	2	3	4	5	6
1	106	106	106	106	107	107
2	107	107	107	107	108	108
3	108	108	108	108	109	109
4	109	109	109	109	110	110
5	110	110	110	110	111	111
6	111	111	111	111	112	112
7	112	112	112	112	113	113
8	113	113	113	113	114	114
9	114	114	114	114	115	115
10	115	115	115	115	116	116
11	116	116	116	116	117	117
12	117	117	117	117	118	118
13	118	118	118	118	119	119
14	119	119	119	119	120	120
15	120	120	120	120	121	121
16						

Figure 4.3: X and Y Coordinates of the primary intensity band

4.2 Postprocessing for Actual Sensor Data

Finally, the algorithm is applied to four actual sensor data from measuring a flat surface, a cylinder, a cylindrical involute gear, and a sphere. In every four cases, the normalized 3D light intensity distribution of a sensor frame is plotted along with the UNCC solution, which is the ridge line detected by the UNCC algorithm. In Figures 4.4, 4.7, 4.10, and 4.13, the blue dashed line represents the UNCC-detected ridge line. Figures 4.5, 4.8, 4.11, and 4.14 illustrate how the Nikon solution oscillates around the UNCC solution in the different measured geometries. In other words, the UNCC solution offers a more uniform solution than the current Nikon solution. This is what is expected from the measurement of a finished surface. The objective function values over the optimization process are given in each case to show the optimization convergence. The given results show that the UNCC solution converges only after a few iterations. The algorithm can perfectly find the ridge line of the sensor frames in various measured geometries, as demonstrated in Figures 4.4 to 4.15.

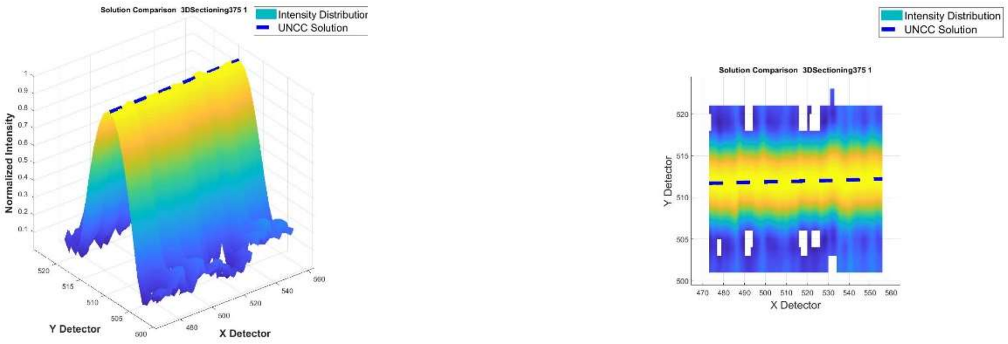

Figure 4.4: Light intensity distribution vs. UNCC solution for a straight ridge line in flat surface measurement

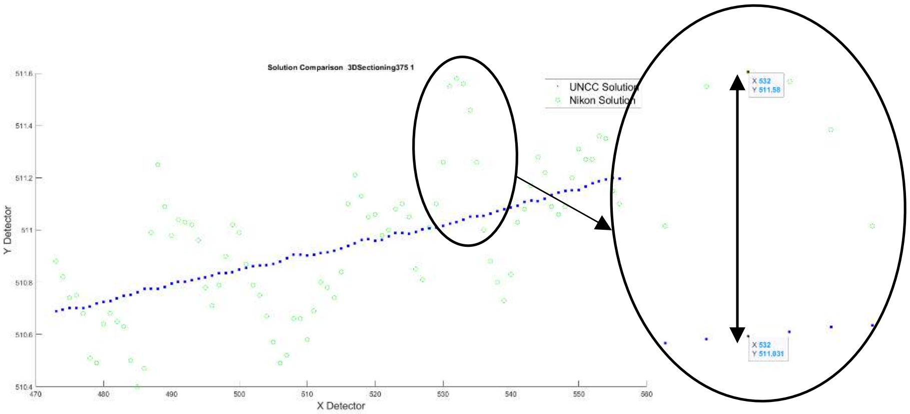

Figure 4.5: UNCC solution vs. Nikon solution for a straight ridge line

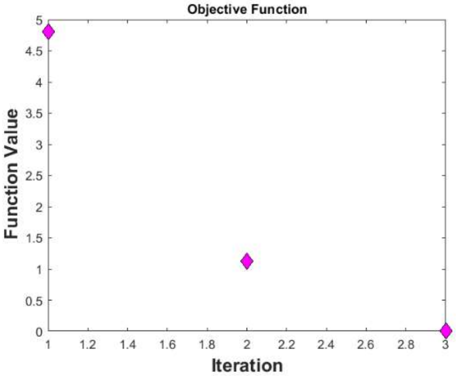

Figure 4.6: Objective function for a straight ridge line

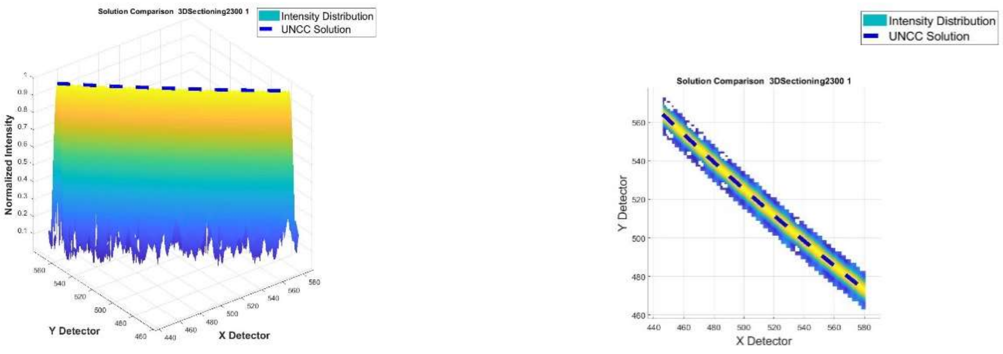

Figure 4.7: Light intensity distribution vs. UNCC solution for a quadratic ridge line in cylinder measurement

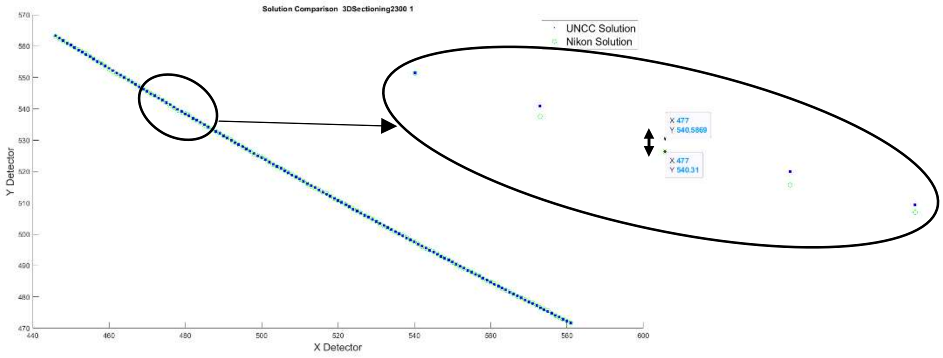

Figure 4.8: UNCC solution vs. Nikon solution for a quadratic ridge line

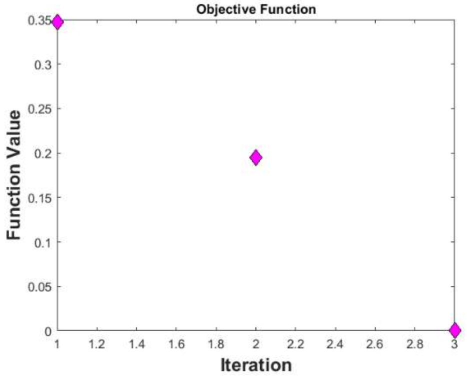

Figure 4.9: Objective function for a quadratic ridge line

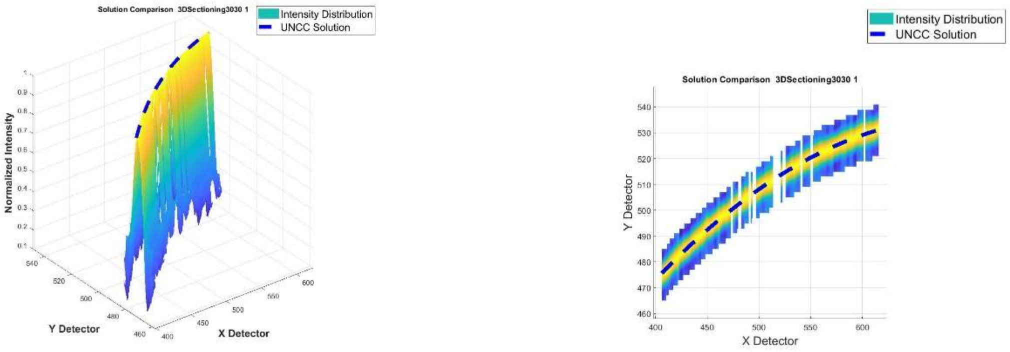

Figure 4.10: Light intensity distribution vs. UNCC solution for a quadratic ridge line in gear measurement

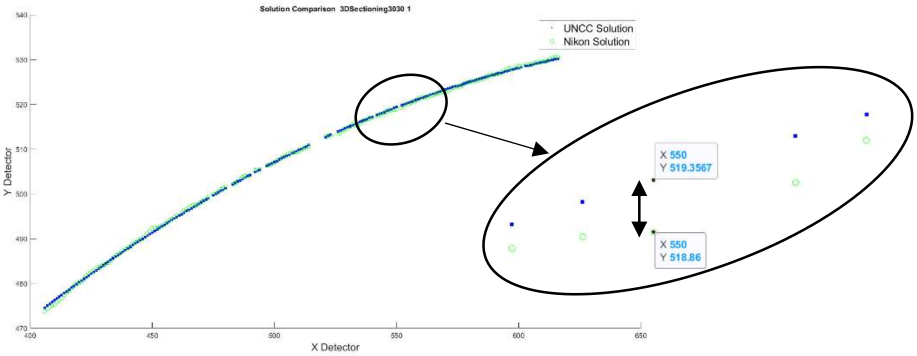

Figure 4.11: UNCC solution vs. Nikon solution for a quadratic ridge line

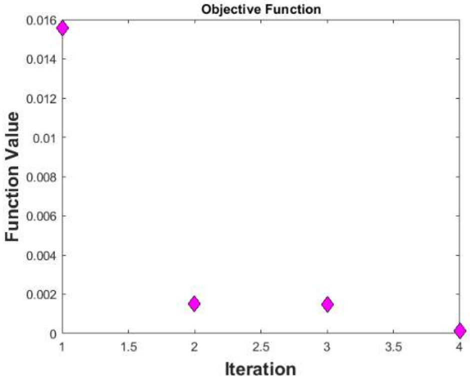

Figure 4.12: Objective function for a quadratic ridge line

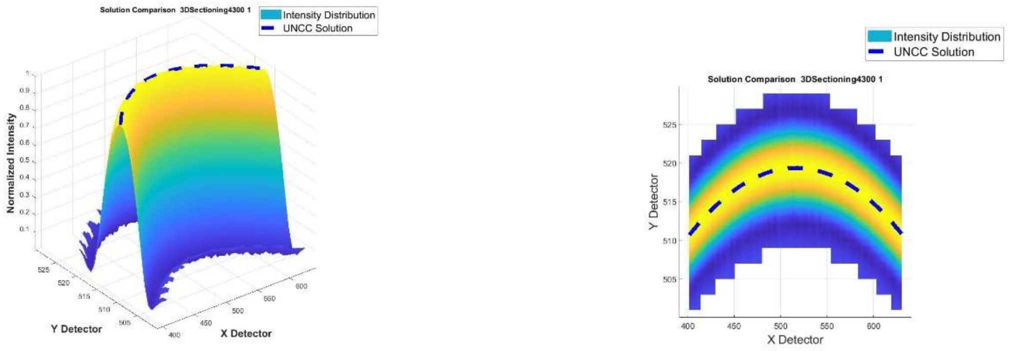

Figure 4.13: Light intensity distribution vs. UNCC solution for an elliptical ridge line in sphere measurement

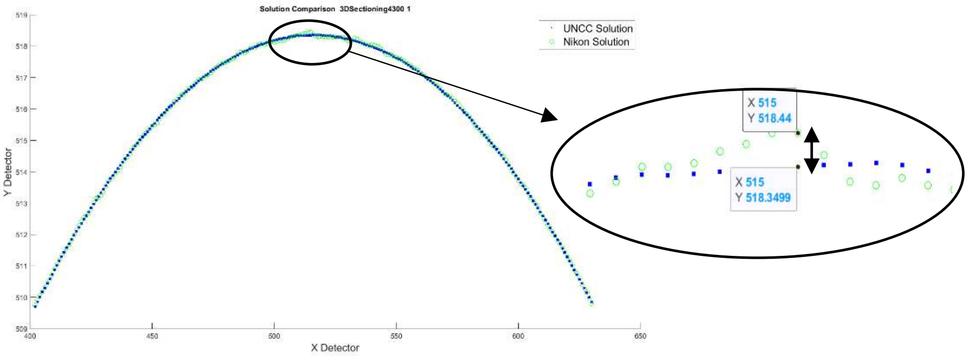

Figure 4.14: UNCC solution vs. Nikon solution for an elliptical ridge line

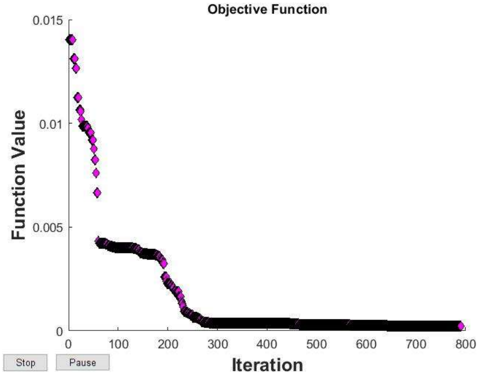

Figure 4.15: Objective function for an elliptical ridge line

4.3 Estimation of Rough Improvement

A rough estimation of the improvement of the implemented UNCC algorithm in terms of the evaluated form deviation of a ground surface is investigated in the next step. A correlation between the deviations in the sensor coordinate system and the machine XYZ coordinate system is essential to find an initial estimation for the improvement caused by modified peak detection compared to the current Nikon peak detection. In order to obtain the correlation, a reference geometry is scanned with the triangulation sensor. The measurement results in both sensor and XYZ coordinate systems are compared to find a correlation between the sensor and the XYZ coordinates. A laser stripe is illuminated to the surface, as shown in Figure 4.16-a or the red dash line in Figure 4.16-b, and the reflected light is captured on the detector, as shown in Figure 4.16-c. Comparing the measured height in two coordinate systems, a correlation is found.

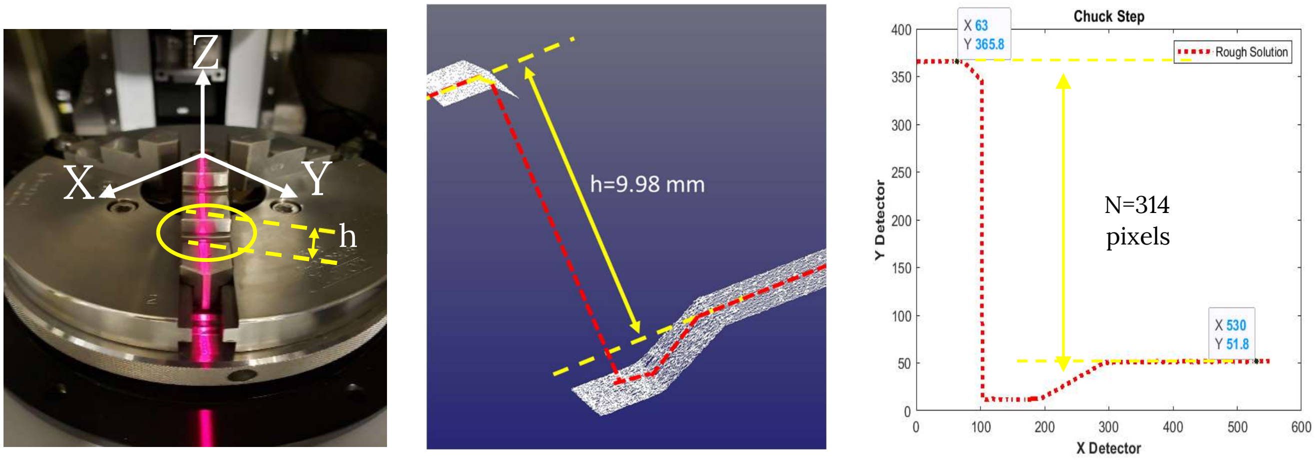

(a) (b) (c)

Figure 4.16: Measurement of machine chuck step using Nikon HN Machine
a) Machine XYZ CS b) Measured points cloud c) Ridge line of one sensor frame

Dividing the step height by the number of pixels ($=\frac{h}{\mathrm{N}}$), every pixel roughly corresponds to 32 microns in the XYZ spatial distance.

4.4 Comparison between UNCC and Nikon Peak Detection Algorithms

In this section, a method is used to compare the UNCC and Nikon solutions numerically. First, a sensor frame is considered the algorithm's input. Then, the UNCC peak detection algorithm is applied to the frame to detect the peak positions of the primary intensity band. After that, a circle is fitted to the positions on sensor coordinates using the least-squares criterion, and the residuals of every position from the fitted circle are calculated for all positions, as illustrated in Figure 4.17. Then, the RMS of the residuals is calculated. Next, the same calculations are performed on the same frame for the Nikon solution to find the residuals and RMS of the Nikon solution from its own fitted circle. Finally, the RMS of the UNCC solution is compared with that of the Nikon solution, as shown in Figure 4.18.

Comparing Nikon and UNCC residuals for one sensor frame, the difference between Nikon and UNCC solution turns out to be in the range of 0.7 pixel, which would correspond to roughly 22 microns. This is a rough comparison in which the effect of combining all successive ridge lines, which may also lead to more reduction in total evaluated form deviation, has not been taken into account.

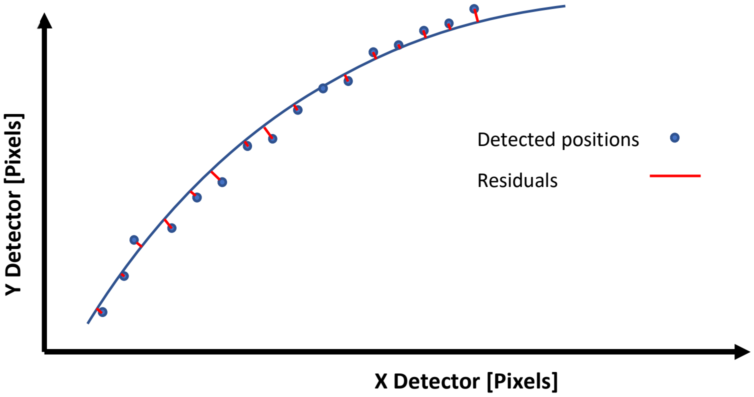

Figure 4.17: Fitted circle and residuals for detected peak positions

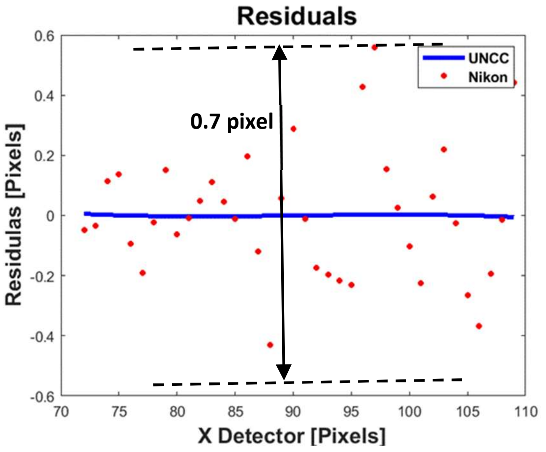

Nikon RMS =0.2075 pixels

Figure 4.18: Comparison between UNCC and Nikon residuals from a circle fit

5 CHAPTER 5: AREAL EVALUATION AND RESULTS

Following the successful peak detection results on an individual sensor frame for different investigated reference geometries discussed in Chapter 4, the proposed algorithm is used to determine the ridge line of every consecutive sensor frame. Then the determined ridge line is converted into the machine XYZ coordinate system as a line of points. Then the converted lines of points are combined to generate the reconstructed point clouds.

As explained in chapter 2, and depending on the instrument capturing frequency, the so-called "Pitch Value" in the supporting metrology software, each surface measurement may include hundreds of consecutive sensor frames. Each frame consists of 1024 rows, zero intensity and nonzero intensity rows. First, the sensor data is fed to the algorithm as the input data. The algorithm breaks the input data into separated frames. Then it modifies the peak position of nonzero intensity rows over one frame or modifies the detected ridge line in each frame. Then it devotes a unique address to each peak position of a row so that later any row of the frames has its unique peak position and address. Modifying the peak positions frame-by-frame for the entire sensor frames, the modified peak positions along with their corresponding addresses are exported from the algorithm.

As illustrated in the below flowchart in Figure 5.1, two sets of information are exported from the Nikon instrument after a surface is scanned: an original lin file and a set of dat files (sensor data). The overall strategy of the modification is to take the original lin file and to use the sensor data and the UNCC algorithm to find the modified peak positions. Having the modified peak positions and their corresponding addresses, the original peak positions in the original lin file can be replaced with the modified peak positions to create the modified lin file. The modified lin file in the next step is converted into the modified point clouds.

In this Chapter, the algorithm is used for the four scanned reference geometries: a flat surface, a cylinder, a sphere, and a commercial helical involute cylindrical gear. In each case, the modified point clouds produced are compared with the original point clouds to evaluate form deviations and offer a sensor calibration for that particular geometry. It should be noted that although the optical measurement results have not been compared with the results of an areal tactile measurement, the measured references have finished surfaces with a form deviation in the single-digit micrometer or sub-micrometer range.

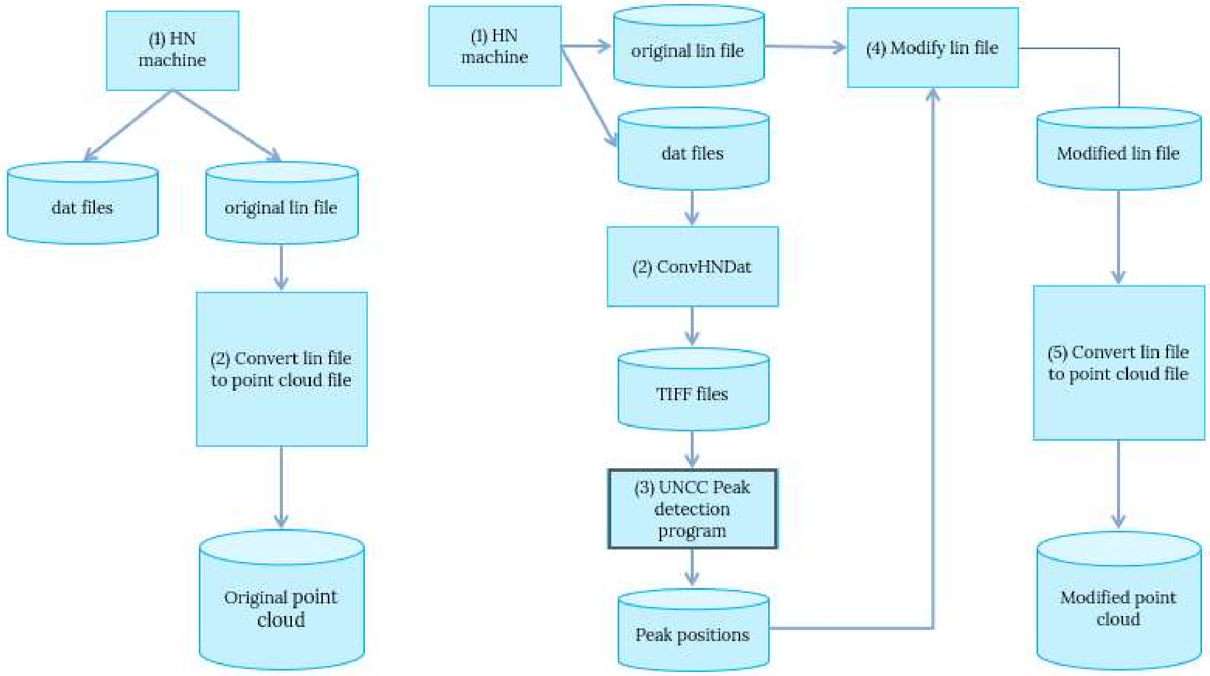

(a) Original Nikon process (b) Proposed process

Figure 5.1: Process of peak detection improvement

5.1 Flat Surface Measurement

The first section performs the above-mentioned process to find the modified point clouds for a nominally flat surface measurement. The original and the modified point clouds are plotted in the same plot as illustrated in Figure 5.2. A plane is fitted to each set of original and modified point clouds to find the deviations from the fitted plane in each case. A licensed MATLAB software is used in this section to determine the fitted plane using the least-squares criterion. Once the number of point clouds exceeds the limit of the fitting software, 19000 points, sampling with a specified sampling factor is used to reduce the number of point clouds.

Then each measured point is projected onto the plane. The normal distance of each measured point from the plane identifies the magnitude of the point's deviation. The deviation vector, on the other hand, is determined by the unit vector connecting the projected point to the measured point. Then magnified deviation magnitude in the deviation vector's direction from the fitted plane forms the magnified deviation. The magnified deviations can be computed using the point deviation's magnitude and vector for all the measured points. The magnified 3D deviations of the flat surface measurement with the magnifying factor of 50 are demonstrated in Figure 5.4. Similar to what was observed earlier in the sensor domain in chapter 4 and as expected, the points modified using the UNCC method represent more uniform point clouds than the scattered Nikon point clouds.

Each frame produces a line of points resembling the projected laser line on the measured geometry. In the case of a flat surface scan, the intersection of two tilted planes forms nominally a line in 3D. In practice, however, the actual data will not form a perfect line due to the measurement uncertainties and the surface features, as illustrated in Figure 5.3. Then all these lines with the predefined pitch value are combined to form a point cloud representing the surface.

The deviations of modified point clouds shown in green dots in Figure 5.4 follows a similar linear pattern over the consecutive frames. To better illustrate the deviation pattern over the consecutive frames, deviations are plotted in 2D. Figure 5.5 shows the 2D point cloud's deviations of the first frame for both the original and modified point clouds. Figure 5.6-a illustrates that if the 2D deviations of the consecutive frames are plotted in the same plot, they seem to follow a similar interesting linear pattern with different slopes and offsets. Suppose a straight line is fitted to the deviations of each frame, and the deviations are subtracted from the fitted line. In that case, the residuals from the fitted line can be derived. Plotting the residuals (transformed deviations) of all frames in the same plot shows that the residuals over the frames match each other, as shown in Figure 5.7.

This similar pattern offers a common term in the deviations of the frames. In other words, the deviations consist of a common term plus an uncommon (a remaining) term. Since the common term repeats for all the frames, it cannot come from the measurand instead comes from the measurement process. More investigations regarding the common term are also performed for other reference geometries. It is concluded that this common term comes from the sensor and needs to be numerically calibrated to improve measurement accuracy. The sensor calibration for different measured geometries is another capability of the UNCC algorithm. Considering the mean of the common term for all the frames in flat surface measurement, the flat surface calibration in machine XYZ coordinate system is derived. The logic of the calibration is to be used in the sensor domain so that later it causes the modification in the actual XYZ domain. The correlation derived in Chapter 4, so-called the correlation factor in this dissertation, is used to convert the calibration into the sensor domain. Due to the linear relation between the two domains, dividing the calibration of the XYZ domain by the calibration factor, the calibration of the sensor domain is calculated.

After the calibration in the sensor domain is calculated, it is used in the UNCC algorithm to find the modified point cloud after the calibration is used. Figures 5.5 and 5.6 show the effect of calibration in the point cloud deviations. As shown in Figure 5.5, after calibration is used, the deviations are smoother and better represent a straight line. These deviations are compatible with the expectation of a finished surface measurement in which the point clouds and the deviations in each frame are expected to represent a straight line.

Looking at the deviation of all the measured points, the flatness, which is the maximum deviation minus minimum deviation, can be calculated in both the original and the modified point cloud. The flatness of the original point cloud and the modified one is 73 and 46 microns, respectively. Looking more at Figure 5.6, the total form deviation considering only the first 20 frames is roughly 25 microns (15-(-10)), although the UNCC algorithm offers a smoother solution than the scattered Nikon solution. In other words, the total form deviation is more influenced by the uncommon term than the common term in each individual frame. Therefore, the large evaluated form deviation is due to the frame-by-frame approach. Although the UNCC algorithm improves the peak detection using a frame-by-frame approach instead of the current Nikon row-by-row approach, it cannot further improve the evaluated form deviation as long as the frame-by-frame approach is used.

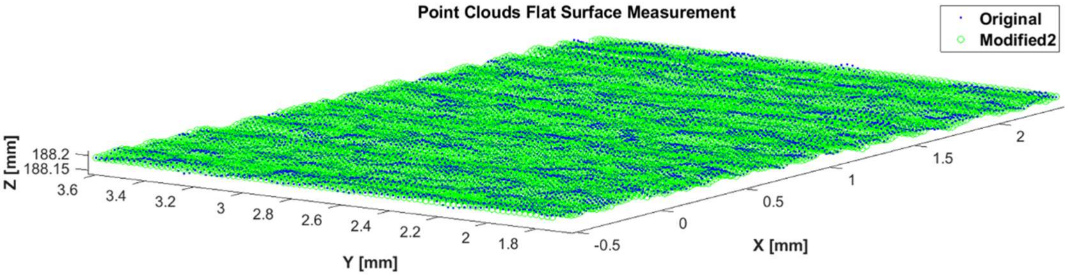

Figure 5.2: Original vs. modified point clouds in flat surface measurement

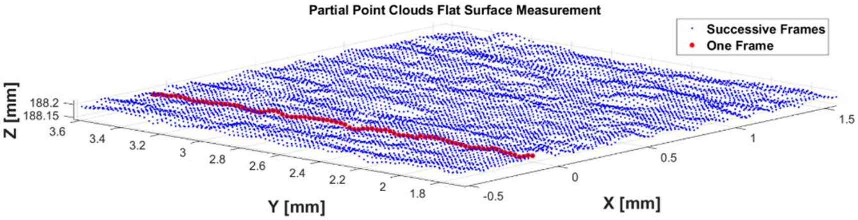

Figure 5.3: Reconstructed point clouds of consecutive frames vs. one individual frame in flat surface measurement

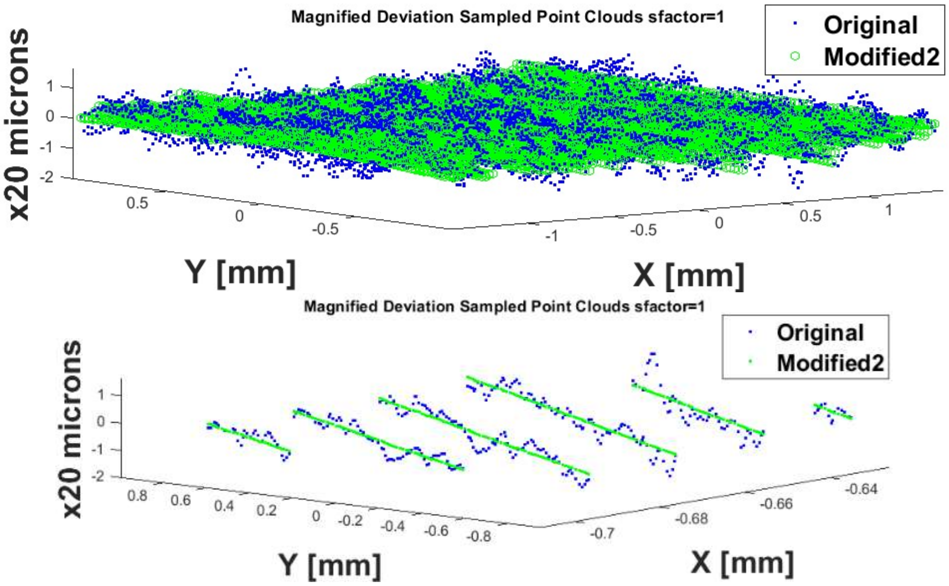

Figure 5.4: Magnified 3D deviations for sampled modified point clouds

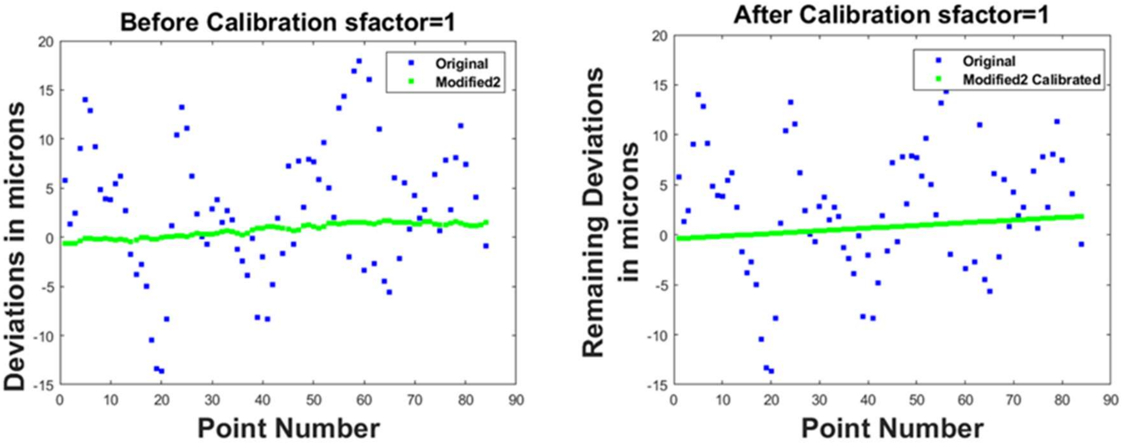

Figure 5.5: 2D deviations of the first frame from the fitted plane for original and modified point clouds

a. Before calibration b. After calibration

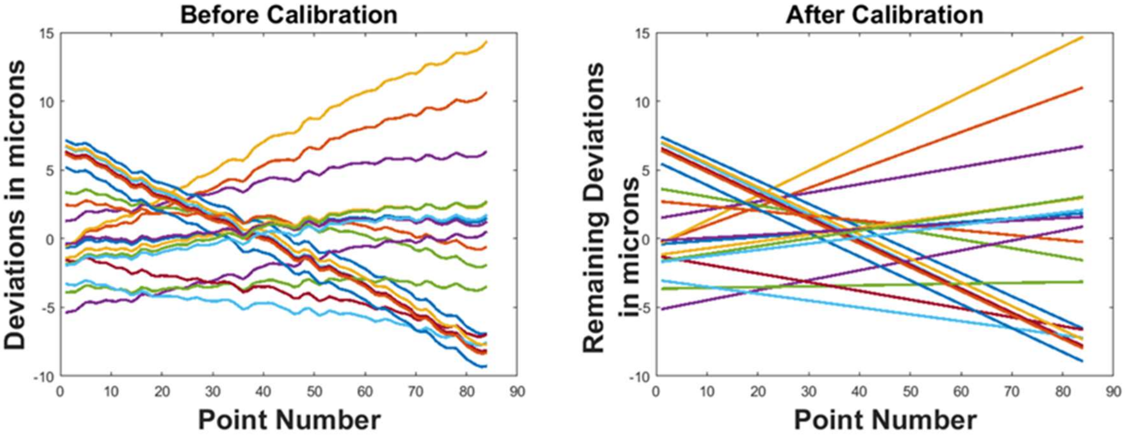

Figure 5.6: 2D deviations of the first 20 frames for the modified point clouds

a. Before calibration b. After calibration

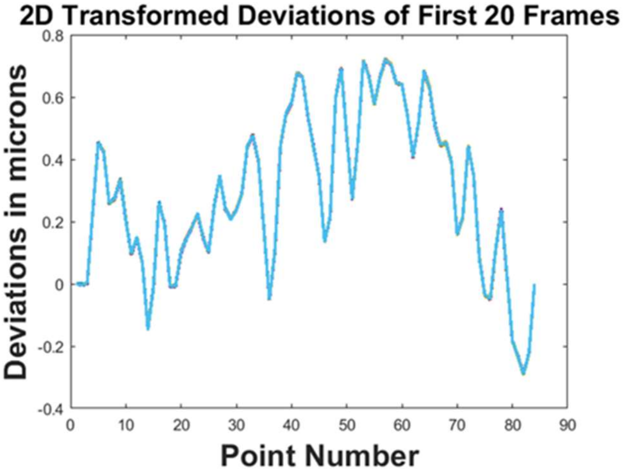

Figure 5.7: 2D transformed deviations of the first 20 frames for the modified point clouds

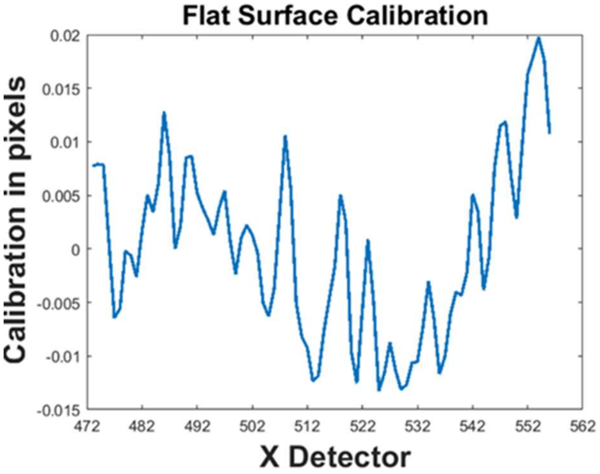

Figure 5.8: Flat surface calibration

5.2 Cylinder Measurement

This section implements modified peak detection on sensor data from a cylinder measurement. The original and modified point clouds are compared in Figure 5.9. A cylinder fit is used to find each case's fitted geometry and measurement deviations. As a result of cylinder fit to each set of data, the radius, height, and central axis of the fitted cylinder are calculated using licensed MATLAB software. A unit vector from the cylinder axes toward the point for every measured point is calculated to represent the deviation direction. The magnitude of the deviation, on the other hand, is calculated through the distance of the measured point from the fitted cylinder's axes minus the reference radius. Having the magnitude and the direction of a deviation, the magnified 3D deviation can be found whose magnitude and direction are the fitted cylinder's radius plus the magnified deviation magnitude and the deviation vector's direction, respectively. The magnified 3D deviations of the cylinder measurement with the magnifying factor of 500 are depicted in Figure 5.11.

As explained earlier, every sensor frame generates a line of points in the shape of the illuminated laser line on the measured geometry. In the current case, the intersection of a tilted plane and a cylinder nominally forms a 3D elliptical shape, as shown in a red line in Figure 5.10. Then all the consecutive generated lines with the predefined pitch value sit one after another to form the entire point clouds.

Again, a close look at the deviations of the modified point clouds shows a repetitive pattern over the consecutive frames. A 2D illustration of the deviations of the first 20 frames is used to investigate the pattern. As shown in Figure 5.12-a, the deviations calculated from the two strategies are compared. It is noted that the UNCC algorithm offers a uniform deviation map and so uniform solution in the case of cylinder measurement as well. Plotting the 2D deviations of the first 20 consecutive frames together in Figure 5.13-a, a similar pattern again can be observed. All the frames' deviations consist of different fourth-order polynomials (uncommon terms) and a common term on top of that. To extract the common term, each deviation map is subtracted from its fitted fourth-order polynomial. The residuals from the fitted polynomials of the first 20 frames are plotted in Figure 5.14. The extracted common residuals over the entire frames, the mean of the frames' residuals, nominates the calibration in the machine coordinate system for the cylinder measurement. Considering the correlation factor between the sensor and the actual XYZ domain introduced earlier, the sensor error correction for calibration in the sensor domain is derived and shown in Figure 5.15.

When the calibration in the sensor domain has been calculated, it is employed in the UNCC algorithm to identify the updated point cloud. The updated 2D deviations of the same frames are demonstrated in Figures 5.12-b and 5.13-b to highlight how sensor calibration affects cylinder measurement. The calibration removes the extra deviations generated due to the noncalibrated sensor. Consequently, the modified point clouds represent more coherent point clouds compared to the dispersed Nikon point clouds.

Evaluating the total cylindricity, which is the algebraic difference between the maximum and the minimum deviations from the best cylinder fit, the UNCC peak detection can improve the measured result from 50 to 29 microns. Looking at Figure 5.13, although the form deviation within one frame does not exceed roughly one micron, considering all 20 frames' deviations, the cylindricity of those frames reaches roughly 4 microns. This example clearly shows how the total evaluated cylindricity is more due to the uncommon term over different frames. Again, that is due to the frame-by-frame nature of the current approaches.

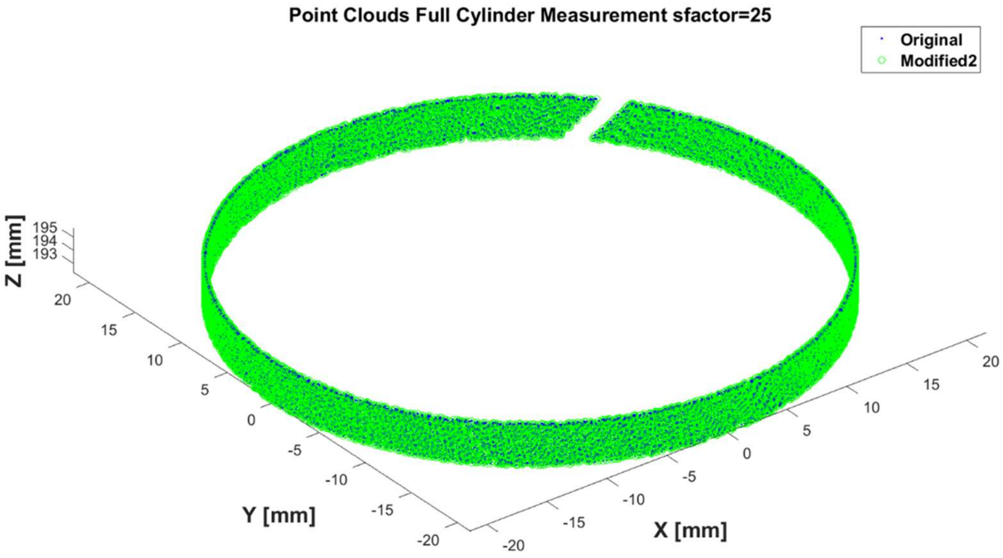

Figure 5.9: Original vs. modified point clouds in cylinder measurement

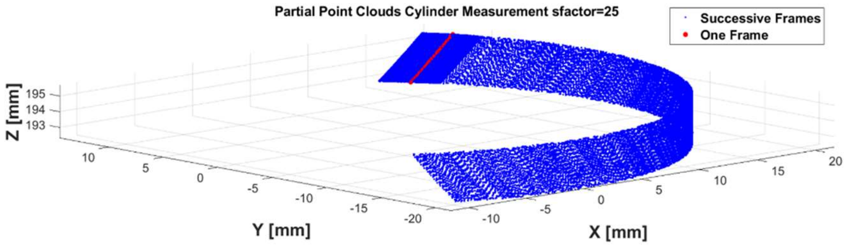

Figure 5.10: Reconstructed point clouds of consecutive frames vs. one individual frame in cylinder measurement

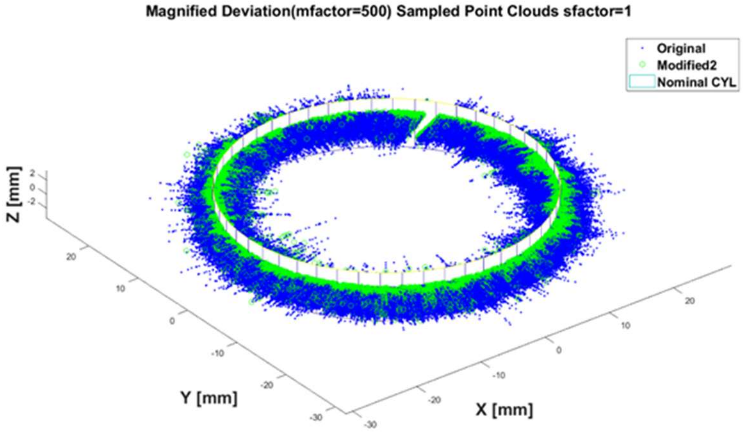

Figure 5.11: Magnified 3D deviations for sampled original and modified point clouds

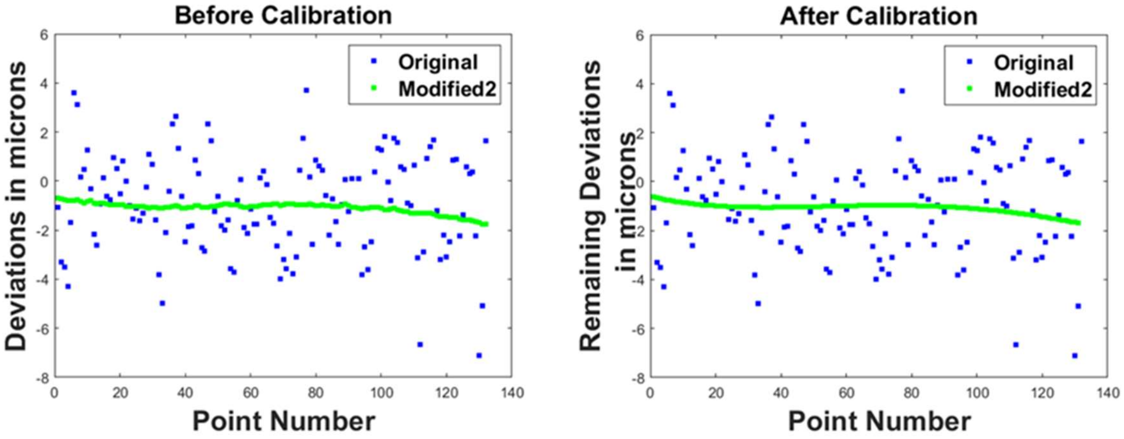

Figure 5.12: 2D deviations of the first frame from the fitted cylinder for original and modified point clouds

a. Before calibration b. After calibration

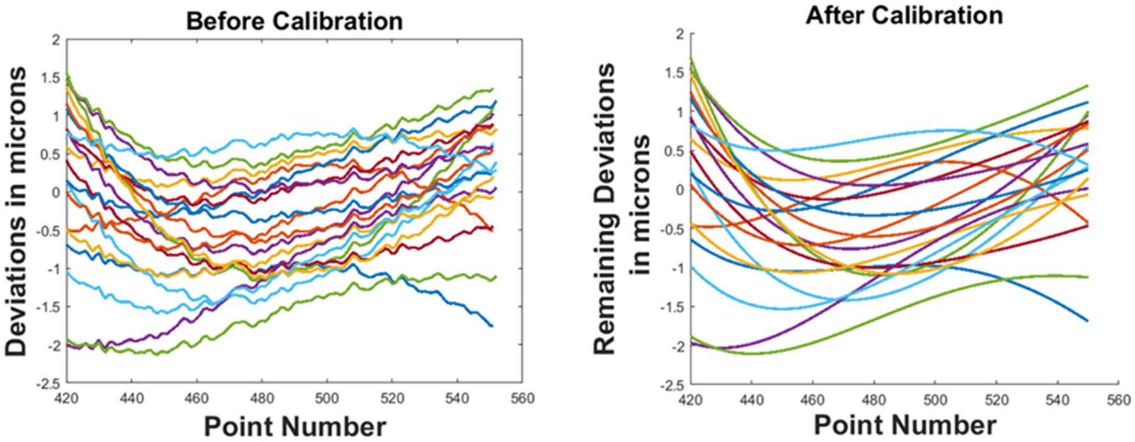

Figure 5.13: 2D deviations of the first 20 frames for the modified point clouds

a. Before calibration b. After calibration

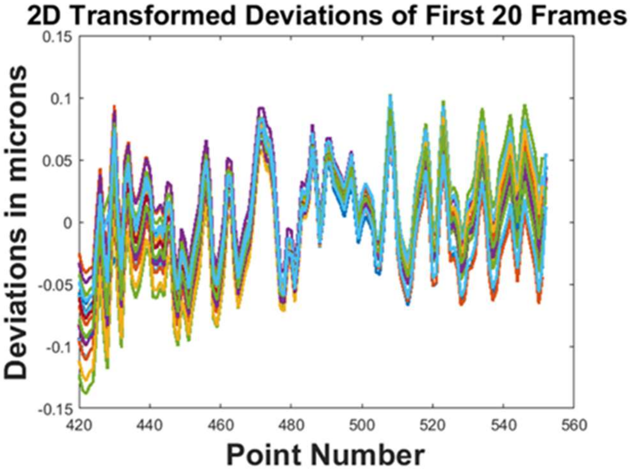

Figure 5.14: 2D transformed deviations of the first 20 frames for the modified point clouds

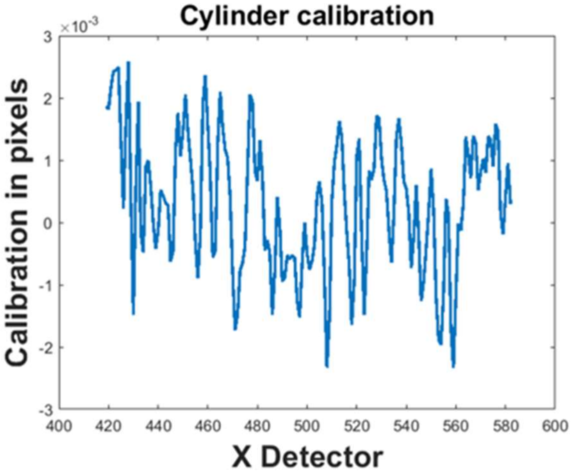

Figure 5.15: Cylinder calibration

5.3 Sphere Measurement

Similar to the flat surface and cylinder measurement sections, the UNCC algorithm helps to provide the modified point clouds out of a sphere measurement. The original and the modified point clouds are demonstrated in Figure 5.16. To find the point cloud deviations, a sphere fit is employed using another MATLAB software for both the original and modified sets. Sampling with a specified sampling factor is also used due to the high volume of the measured point clouds and the limit of the fitting software (19000 points).

A vector from the fitted Sphere's center to the measured point is used to calculate the deviation magnitude and vector. The magnitude of the vector deducted by the nominal sphere radius determines the deviation's magnitude and the unit vector's direction. Then magnified deviation magnitude in the deviation vector's direction from the fitted Sphere forms the magnified deviation. The magnified deviations can be calculated if the magnitude and vector of each point deviation are available. Figure 5.18 displays the amplified 3D deviations of the sphere measurement when the magnification factor is set to 500.

In the case of sphere measurement, every sensor frame produces a line of points in the shape of the intersection of a tilted plane and a sphere section which is nominally a partial circle in 3D, as shown in Figure 5.17. Combining all the produced lines, as the surface is scanned frame by frame, the entire point clouds are reconstructed.

Similar to the calibration section of the other two geometries, the deviation map of each frame is calculated to eventually find the calibration correction. The 2D deviation maps of the first frame are depicted in Figure 5.19-a. Comparing the deviation map of the original and the modified methods, again, the modified point clouds represent more continuous deviations than those of the original one. Figure 20-a shows a similar pattern in the deviation map of the first 20 frames. Each map comprises a fourth-order polynomial term superimposed with a repeated term. The repeated term can be extracted using fourth-order polynomial regression to each deviation map and subtracting the map from the 4th order term. Again, the residual term of the various frames resembles each other, as demonstrated in Figure 5.21.

The observed similar pattern can be used to extract the sensor error correction for calibration. Considering the mean of the common term for all the frames in sphere measurement, the sphere calibration in XYZ coordinate system is calculated. Then, the sphere calibration in the sensor domain illustrated in Figure 5.22 is calculated using the linear correlation factor.

Next, the calculated sphere calibration in the previous step is imported into the UNCC algorithm to improve the point clouds further. The improvement can be seen in Figures 5.19-b and 5.20-b, where the calibration eliminates the sensor error, which, in turn, generates a smoother measured profile in each frame and total.

The sphericity, defined as the maximum deviation minus the minimum deviation, can be obtained by evaluating the original and the modified point cloud's deviation values. Sphericity measures 44 microns for the original point cloud versus 7 microns for the modified version. Similar to what was discussed earlier and having a careful look at Figure 5.20, the origin of the smaller evaluated sphericity compared to the larger values for the evaluated flatness and cylindricity is the similar value of the uncommon terms over consecutive frames.

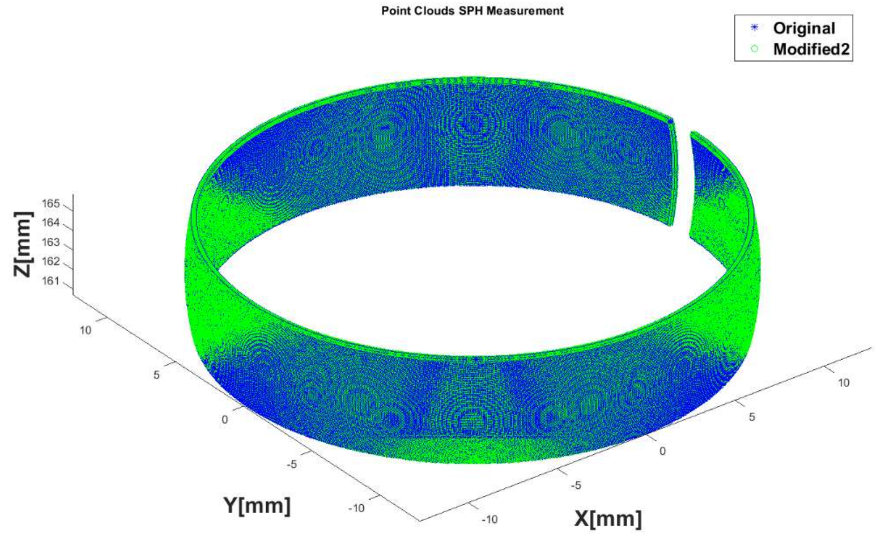

Figure 5.16: Original vs. modified point clouds in sphere measurement

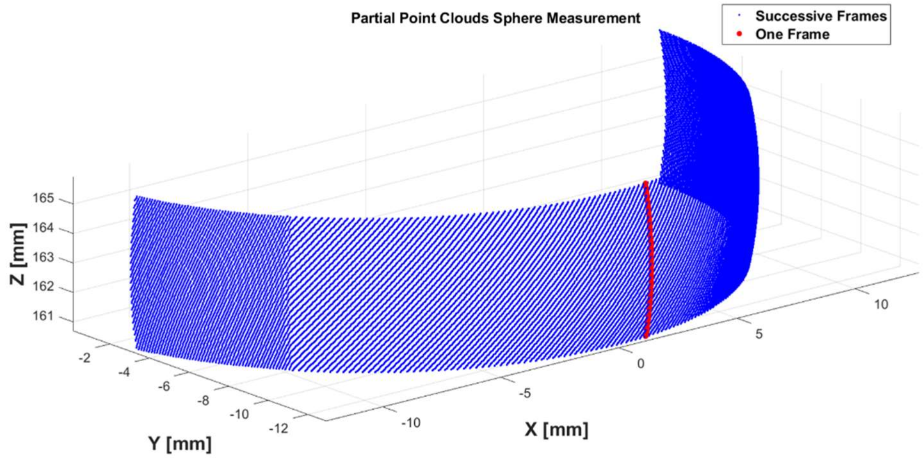

Figure 5.17: Reconstructed point clouds of consecutive frames vs. one individual frame in sphere measurement

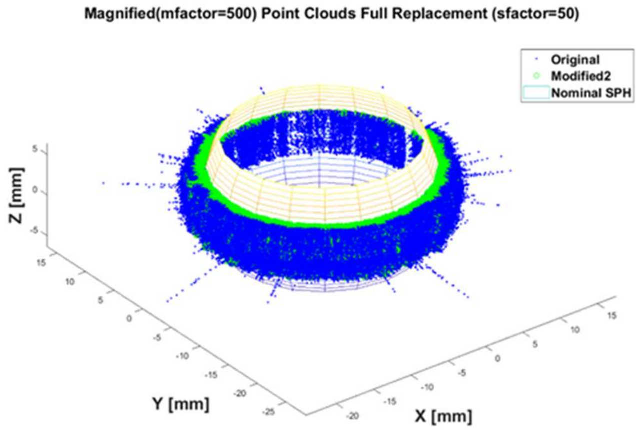

Figure 5.18: Magnified 3D deviations for sampled original and modified point clouds

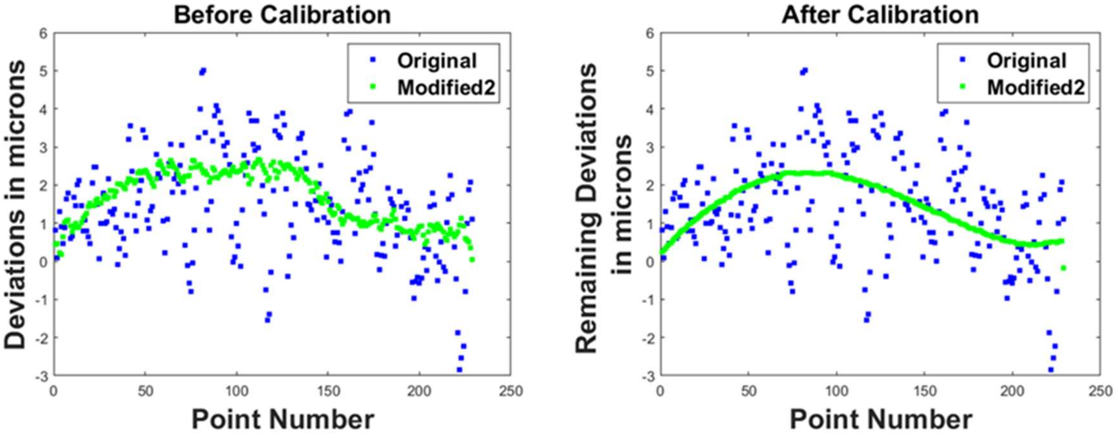

Figure 5.19: 2D deviations of the first frame from the fitted Sphere for original and modified point clouds

a. Before calibration b. After calibration

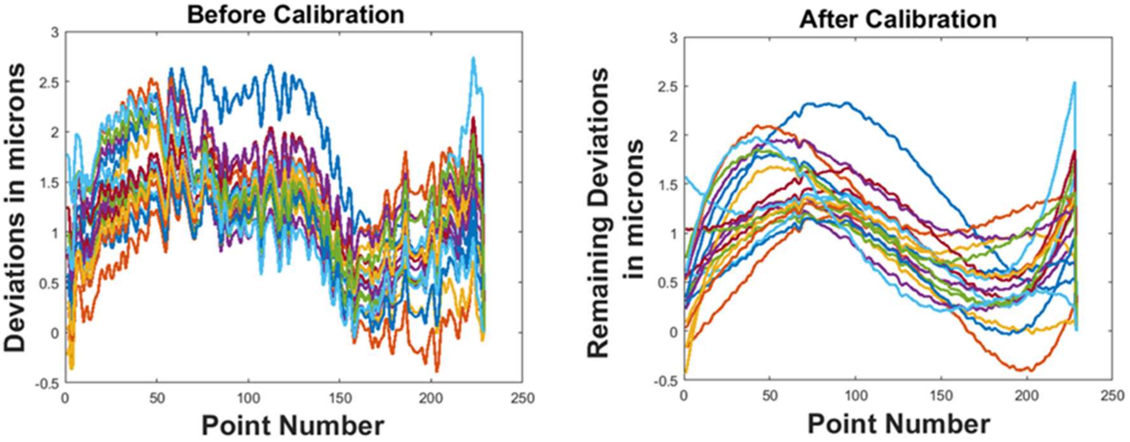

Figure 5.20: 2D deviations of the first 20 frames for the modified point clouds

a. Before calibration b. After calibration

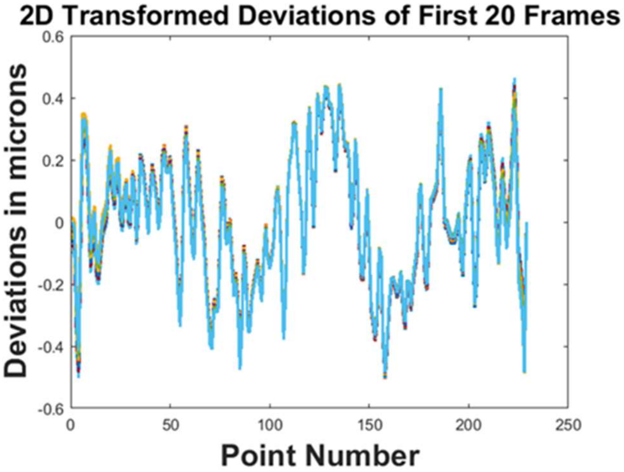

Figure 5.21: 2D transformed deviations of the first 20 frames for the modified point clouds

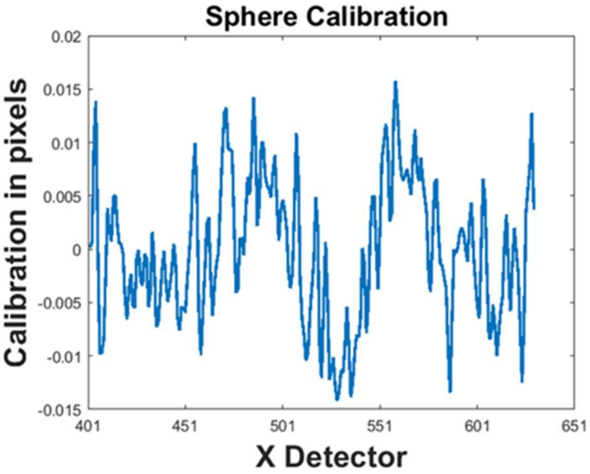

Figure 5.22: Sphere calibration

5.4 Helical Cylindrical Gear Measurement

Once the algorithm is tested on three reference geometries, i.e., flat surface, cylinder, and Sphere, it is implemented for gear evaluations in the current section. As discussed earlier in the literature review, using the Plumb line distance concept, an equation has been presented to describe the 3D geometry of a gear flank surface; based on that, an areal description of the flank surface named the areal distance map has been defined. An areal evaluation method [26] has been proposed in which gear deviation parameters can be extracted directly from an areal distance map. This method maps the nominal flank geometry and the deviations from the nominal geometry into a local uvd coordinate system, as illustrated in Figure 5.23. This coordinate system is an essential part of Ni's algorithm for areal gear evaluations. Hence, regarding gear measurement, first, the coordinate system and deviations are discussed to elaborate later on the effect of using peak detection modifications.

5.4.1 Areal Distance Map and Surface Decomposition

Figure 5.23 depicts a coordinate system on the flank surface that can be constructed using the direction of profile generation as one axis (labeled u), the direction of helix generation (labeled v) (which is the same as the z-axis), and the surface normal direction (labeled d). Probing in the v direction is equivalent to a helix measurement, and measuring in the u direction is the same as a profile measurement in the conventional gear measurement. At various points along the flank, the direction of the surface normal changes. Accordingly, this coordinate system varies with respect to the gear coordinate system at various measurement points. Each point's plumb line distance, denoted by the value d, is the height of the point in the uvd coordinate system. The nominal flank surface is transformed into the u-v plane with the plumb lines of zero. A distance map is constructed using the point's plumb line distances from the set of measured points. This distance map is identical to the deviation map (containing only undesirable deviations) in the absence of gear modification. In the case of modified gear, on the other hand, the distance map is a combination of undesired deviations and the desired modifications.

The distance map then incorporates all modifications. Figure 5.23 shows that all distances from the pure involute surface along the surface normal can be linearly combined and, conversely, removed from the distance map. Once the intended modifications to a measured gear are eliminated, eventual deviations from the nominal modified surface are either undesirable or should be kept to a minimum. Two-dimensional orthogonal Chebyshev polynomials are used for surface decomposition.

When an orthogonal series of polynomials on the [-1,1] domain is available, a linear combination of these features can decompose any function. This decomposition method is analogous to the Fourier series and the Zernike polynomials. Therefore, decomposing the deviation map into these features with certain coefficients would indicate the contribution of each on the surface. The coefficients in this method have the benefit of being orthogonal, meaning they do not interact with one another [32,33]. The polynomials also have a shape resembling the desired gear modifications. Figure 5.24 shows a comparison between six gear parameters and the Chebyshev term up to the second order.

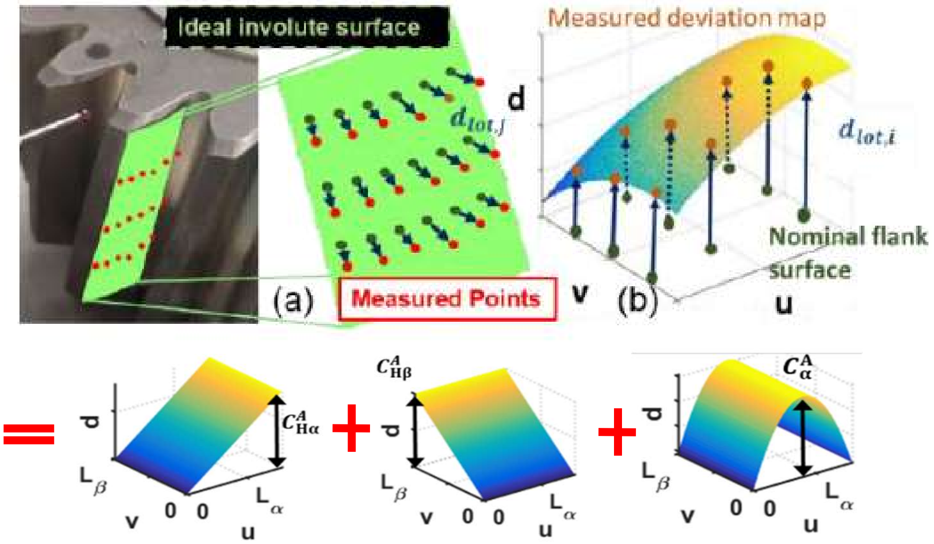

Figure 5.23: Mapping the measured points to the areal surface coordinate system (uvd), and surface decomposition [after 32]

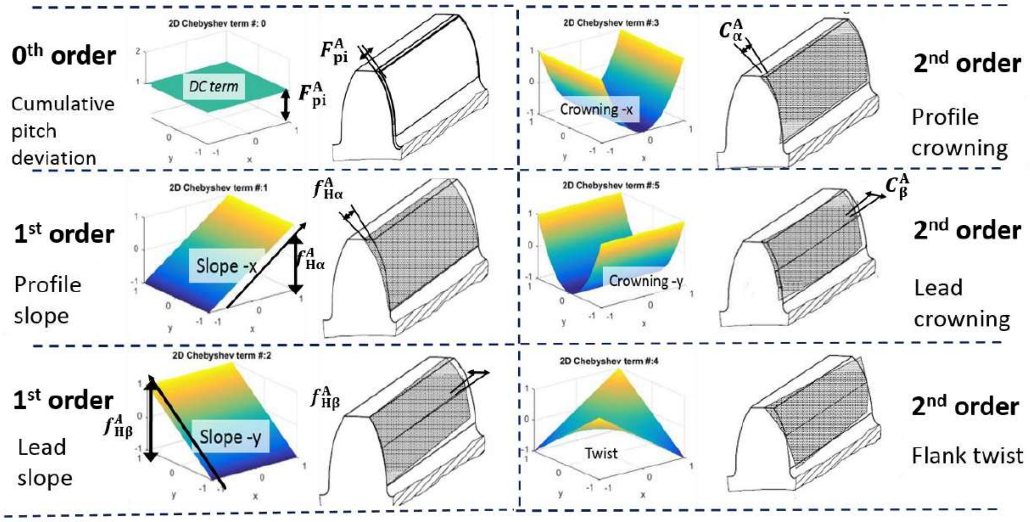

Figure 5.24: Geometric resemblance of areal flank modifications/deviations by low order 2D Chebyshev polynomials [after 6,32]

5.4.2 Evaluation Results

With this background in mind, commercial gear is measured by the Nikon Instrument, and the algorithm is implemented on a full flank measurement. Then an evaluation MATLAB software developed by Yue Peng is used to provide the gear evaluation results to investigate the effect of the peak detection algorithm on the generated point clouds. The input of the evaluation software is a CSV file, including the measured point clouds in gear coordinate system, which is the output of the peak detection algorithm.

The evaluation results are given below to see the new algorithm's improvement on the evaluated form deviation values.

Figure 5.25 shows the deviation map of one measured flank without applying the UNCC peak detection algorithm. The form deviation, the algebraic difference between the maximum and the minimum deviations from the nominal flank surface, turns out to be 43.8 microns.

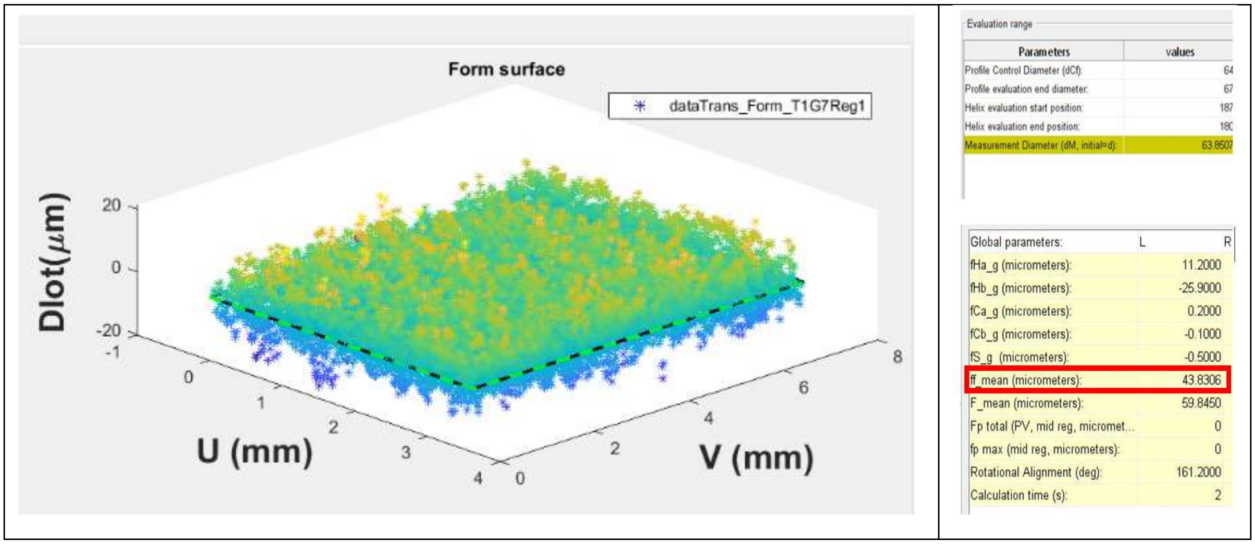

Evaluation range

Parameters	values
Profile Control Diameter (dCf):	64
Profile evaluation end diameter:	67
Helix evaluation start position:	187
Helix evaluation end position:	18
Measurement Diameter (dM, initial=d):	63.8507

Global parameters:	L	R
fHa_g (micrometers):	11.2000	
fHb_g (micrometers):	-25.9000	
fCa_g (micrometers):	0.2000	
fCb_g (micrometers):	-0.1000	
fS_g (micrometers):	-0.5000	
ff_mean (micrometers):	43.8306	
F_mean (micrometers):	59.8450	
Fp total (PV, mid reg, micromet...	0	
fp max (mid reg, micrometers):	0	
Rotational Alignment (deg):	161.2000	
Calculation time (s):	2	

Figure 5.25: Deviation map and evaluated results for the first flank of Gear T without peak detection improvement

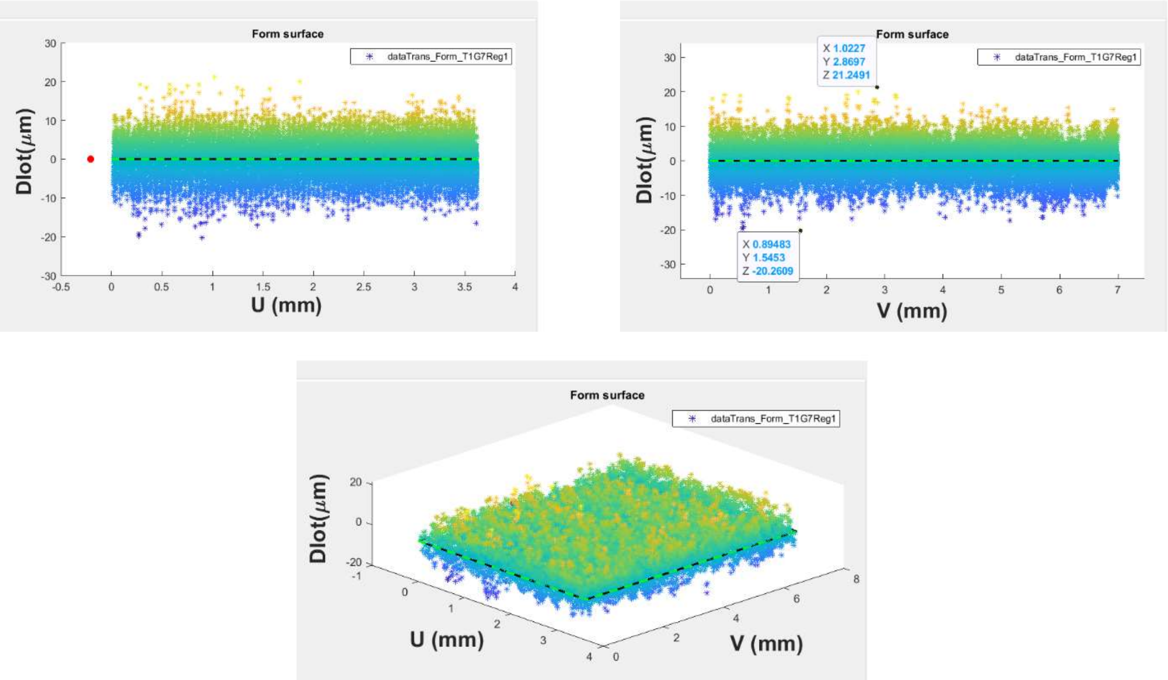

Figure 5.26: Deviation map of the first flank of Gear T without peak detection improvement in different views

Figure 5.27 shows the deviation map of the same flank after applying the UNCC peak detection algorithm. The evaluated form deviation is reduced to 9 microns over the same evaluation range. As can be seen from Figures 5.27 and 5.28, a higher-order term along the U direction can be observed from the form deviation map that repeats in the V direction. Similar to other reference geometries, this is due to the frame-by-frame nature of the algorithm. In the case of gear measurement, the calibration is not performed due to limited access to the evaluation software.

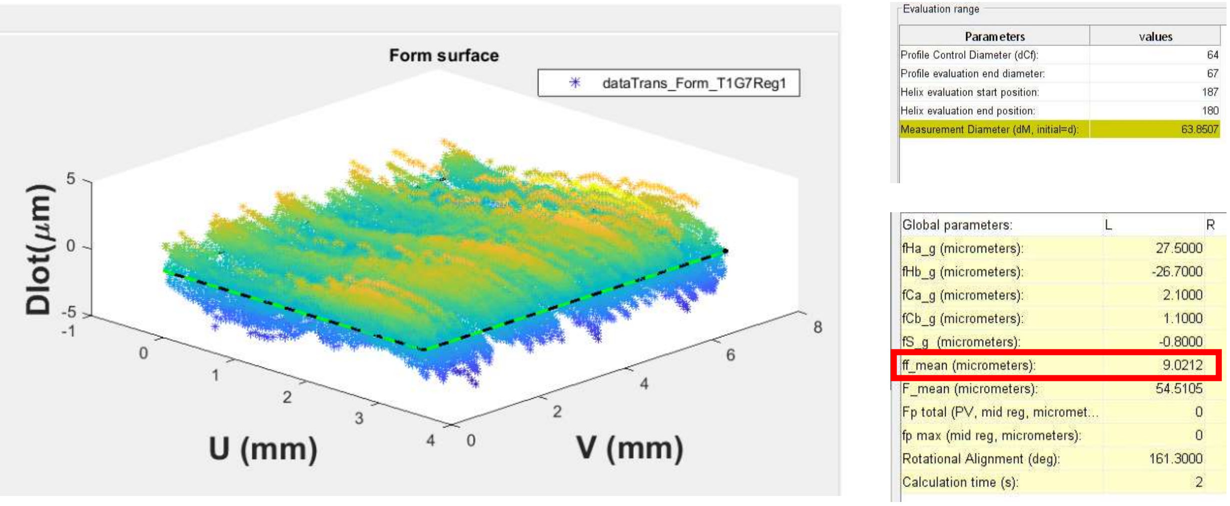

Parameters	values
Profile Control Diameter (dCf):	64
Profile evaluation end diameter:	67
Helix evaluation start position:	187
Helix evaluation end position:	180
Measurement Diameter (dM, initial=d):	63.8507

Global parameters:	L	R
fHa_g (micrometers):	27.5000	
fHb_g (micrometers):	-26.7000	
fCa_g (micrometers):	2.1000	
fCb_g (micrometers):	1.1000	
fS_g (micrometers):	-0.8000	
ff_mean (micrometers):	9.0212	
F_mean (micrometers):	54.5105	
Fp total (PV, mid reg, micromet...	0	
fp max (mid reg, micrometers):	0	
Rotational Alignment (deg):	161.3000	
Calculation time (s):	2	

Figure 5.27: Deviation map and evaluated results for the first flank of Gear T with peak detection improvement

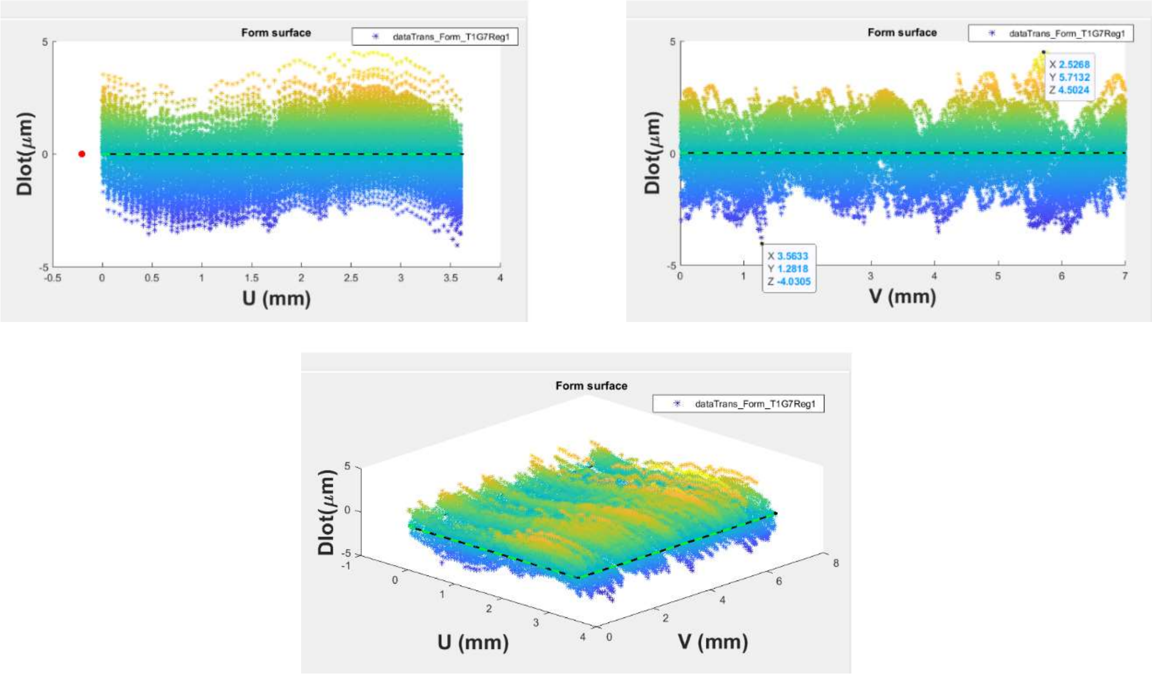

Figure 5.28: Deviation map of the first flank of Gear T with peak detection improvement in different views

Figure 5.29 shows the contribution of a ridge line of one sensor frame from gear measurement in different coordinate systems.

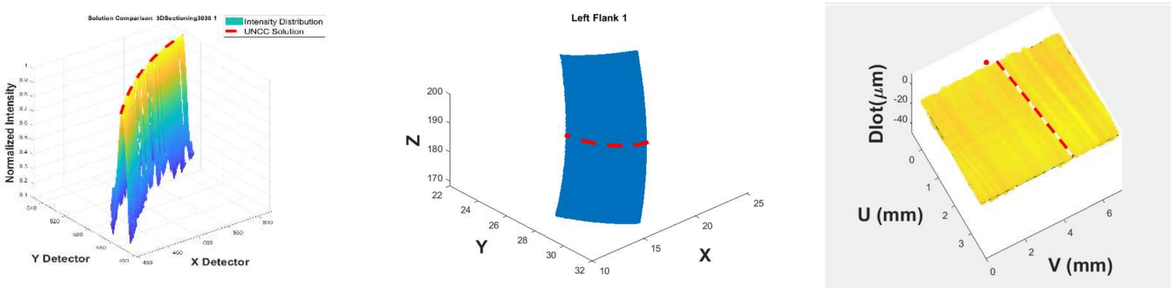

(a) Sensor CSY

(b) Workpiece CSY

(c) Evaluation CSY

Figure 5.29: One sensor frame in different CSYs

6 CHAPTER 6: CONCLUSION AND FUTURE WORK

6.1 Conclusion

In summary, this dissertation improves the profile fidelity of triangulation sensor measurement in optical inspection. An alternative mathematical approach to improving the ridge line detection at each sensor frame, which is the line in the x-y sensor domain with the highest light intensity, is proposed for the instrument to detect the peak position of that frame even more accurately. An analytical model of the sensor pixels' intensities is introduced to be compared with the measured intensities. The method uses three or four coefficients to model a ridge line profile across the sensor; depending on the investigated geometries, three coefficients are used for a quadratic ridge line, and four coefficients are used for an elliptical one. It also uses two additional coefficients to model the light intensity distribution over every sensor row. An iterative optimization is then proposed to find the best approximation for the model-based intensities out of the measured ones. Having the optimized solution for each frame, the modified ridge line can be detected.

A MATLAB algorithm that includes various sections, each designed to add a capability, is developed based on the proposed peak detection method. One algorithm's preprocessing section removes multiple light reflections from the input frames. The instrument capturing frequency, known as "pitch value," determines the total count of the scanning frames. Performing the same peak detection for all the scanning frames, all the modified ridge lines across the successive frames are found. The algorithm also devotes a unique address to every sensor row for all the sensor frames to be used later to replace the original (Nikon) ridge lines with the modified ridge lines. The modified ridge lines are replaced, and the modified point clouds are extracted.

The proposed algorithm uses numerical simulations on four sets of simulation data (based on various ridge line profiles and intensity distributions) to obtain the model-based ridge line from the simulated intensities in a sensor frame. Conformance between the optimized coefficients and the given simulated ones is obtained on four simulations. Then the actual sensor data of a single frame for various reference geometries, i.e., flat surface, cylinder, sphere, and gear, are fed to the algorithm to detect the improved ridge lines. The modified ridge line offered a smoother profile in each case compared to the current scattered original ridge line, which is compatible with the expectation of measuring a finished surface. Then a numerical correlation between the sensor coordinates system and the workpiece one is calculated to roughly estimate the improvement of the implemented proposed algorithm in terms of the evaluated form deviation of a ground surface. One pixel in the sensor coordinates system roughly corresponds to 32 microns in the coordinates system.

The algorithm is then used to measure the four above-mentioned reference geometries to find the modified evaluated point clouds out of the surface measurements. The deviation of each set of measured point clouds from its best fit after the algorithm is implemented is calculated to illustrate a common pattern in the deviations of the successive scanning frames for each geometry. Using the mean of the residuals between the deviations and the common deviation term for all the scanning frames in each geometry measurement, the sensor calibration for that measured reference geometry is offered.

The modified point clouds showed a smaller evaluated form deviation for all four reference geometries. Having a closer look at the above-mentioned deviations in a few successive frames, the total form deviation is more influenced by the start and the end deviations in each frame than the change of the deviations across each individual frame. Therefore, the large, evaluated form deviation is due to the frame-by-frame approach.

6.2 Future Work

Although there is promise in the proposed peak detection algorithm's potential applications, several significant issues still need to be researched in depth.

6.2.1 Calibration across the Entire Sensor Domain

As mentioned in Chapter 5, either the Nikon instrument or software adds a repeated pattern to the reconstructed point clouds when the modified peak detection process is used, or during the original Nikon process, they internally calibrate the sensor data that the modified process does not have access to. Therefore, an extra repeated pattern exists once the modified peak detection process is used that needs to be numerically removed through sensor calibration. The proposed calibration process does not cover the entire sensor domain; hence, a comprehensive calibration can be performed in the future. This calibration can be done either by using a longer artifact for the entire sensor to be covered or by performing a set of measurements so that the entire sensor is used.

6.2.2 Frame-by-Frame Approach

Although the proposed algorithm improves the peak detection using a frame-by-frame approach instead of the current original row-by-row approach, it cannot further improve the evaluated form deviation as long as the frame-by-frame approach is used.

6.2.3 Closed-Loop Control

The proposed algorithm can be used in the future closed-loop control process where the new gear production processes require fast-optical measurement and evaluation processes to trace back from the finally achieved gear geometry to its origins in the manufacturing process. This extension can be achieved by equipping the manufacturing machine with suitable optical measuring devices, an appropriate evaluation strategy, and an inline inspection.

REFERENCES

[1] Goch, G. "Gear metrology." CIRP Annals-Manufacturing Technology 52.2 (2003): 659-695.

[2] K. D. Bouzakis, E. Lili, N. Michailidis, and O. Friderikos, "Manufacturing of cylindrical gears by generating cutting processes: A critical synthesis of analysis methods," CIRP Annals - Manufacturing Technology, vol. 57, no. 2, pp. 676–696, 2008.

[3] B. Karpuschewski, H. J. Knoche, and M. Hipke, "Gear finishing by abrasive processes," CIRP Annals - Manufacturing Technology, vol. 57, no. 2, pp. 621–640, 2008.

[4] C. Heinzel and A. Wagner, "Fine finishing of gears with high shape accuracy," CIRP Annals - Manufacturing Technology, vol. 62, no. 1, pp. 359–362, 2013.

[5] K. Erkorkmaz, A. Katz, Y. Hosseinkhani, D. Plakhotnik, M. Stautner, and F. Ismail, "Chip geometry and cutting forces in gear shaping," CIRP Annals - Manufacturing Technology, vol. 65, no. 1, pp. 133–136, 2016.

[6] International Organization for Standardization. *ISO1328-1: Cylindrical Gears—ISO System of Flank Tolerance Classification—Part 1: Definitions and Allowable Values of Deviations Relevant to Flanks of Gear Teeth*; ISO: Geneva, Switzerland, 2013.

[7] Peggs, G.N.; Maropoulos, P.G.; Hughes, E.B.; Forbes, A.B.; Robson, S.; Ziebart, M.; Muralikrishnan, B. Recent developments in large-scale dimensional metrology. *Proc. Inst. Mech. Eng. B* 2009, *223*, 571–595, doi:10.1243/09544054JEM1284.

[8] Franceschini, F.; Galetto, M.; Maisano, D.; Mastrogiacomo, L. Large-scale dimensional metrology (LSDM): From tapes and theodolites to multi-sensor systems. *Int. J. Precis. Eng. Manuf.* **2014**, *15*, 1739–1758, doi:10.1007/s12541-014-0527-2.

[9] Lotze, W., Hartig, F., 2001, 3D gear measurement by CMM. Laser Metrology and Machine Performance "Lambdamap" in Birmingham, UK, p. 333. ISBN 1- 8531 2-890-2.

[10] Laser line triangulation for fast 3D measurements on large gears

[11] ISO/FDIS 21771, Gears – Cylindrical Involute Gears and Gear Pairs – Concepts and geometry; 2007(E).

[12] G. Goch, K. Ni, Y. Peng, and A. Guenther, "Future gear metrology based on areal measurements and improved holistic evaluations," CIRP Annals - Manufacturing Technology, vol. 66, no. 1, pp. 469–474, 2017.

[13] A. Guenther, "Flaechenhafte Beschreibung und Ausrichtung von Zylinderraedern mit Evolventenprofil," Universitaet Ulm, 1996.

[14] Goch, G., Gunther, A, 2002, Future Gear Metrology, Superficial Description and Inspection of Flanks, in:
International Conference on Gears Vol. 2, VDIBerichte 1665, p. 751-768.

[15] Gunther, A. et al., 2002, Austauschformat fur Verzahnungsdaten, VDI-Berichte 1673, p. 159-1 70.

[16] F. Takeoka et al., "Design of Laser Interferometric Measuring Device of Involute Profile," Journal of Mechanical Design, vol. 130, no. 5, p. 52602, 2008.

[17] S. Fang, L. Wang, M. Komori, and A. Kubo, "Simulation method for interference fringe patterns in measuring gear tooth flanks by laser interferometry. " Applied optics, vol. 49, no. 33, pp. 6409–15, 2010.

[18] G. Lu, S. Wu, N. Palmer, and H. Liu, "Application of Phase Shift Optical Triangulation to Precision Gear Gauging," vol. 3520, no. November, pp. 52–63, 1998.

[19] https://www.acuitylaser.com/sensor-resources/laser-triangulation-sensors/#01

[20] https://en.wikipedia.org/wiki/File:Laserprofilometer_EN.svg

[21] Peters J, Goch G, Günther A. Helical gear measurement using structured light. In: Proceedings of the XVI IMEKO world congress. Wien; 2000. p. 227–30.

[22] Leopold J, Günther H. Fast 3D measurement of gear wheels. In: Seventh international symposium on laser metrology applied to science, industry, and everyday life, vol. 4900. International Society for Optics and Photonics; 2002, p. 185–94.

[23] Kumar A, Jain P, Pathak P. Curve reconstruction of digitized surface using k-means algorithm. Procedia Eng 2014;69:544–9. http://dx.doi.org/10. 1016/j.proeng.2014.03.024, URL
http://www.sciencedirect.com/science/article/
pii/S1877705814002707.

[24] Chen Y, Chen J. Optical inspection system for gear tooth surfaces using a projection Moiré method. Sensors 2019;19(6):1450. http://dx.doi.org/10.3390/ s19061450.

[25] Härtig F, Stein M. 3D involute gear evaluation – Part I: Workpiece coordinates. Measurement 2019;134:569–73. http://dx.doi.org/10.1016/j. measurement.2018.10.088, URL
http://www.sciencedirect.com/science/article/
pii/S0263224118310315.

[26] Ni K. Areal gear metrology with modified flanks [Ph.D. thesis], The University of North Carolina at Charlotte; 2017.

[27] MS3D, "3D INSPECTION OF GEAR." [Online]. Available: http://www.ms3d.eu/en/our-machines/3d-inspection-of-gear-gearinspection/.
http://www.manufacturing-technologies.com/libo/files/pdfuk/fiche_soc-1029.pdf

[28] Nikon HN-C3030, Non-contact sensor 3D measuring system, Product information, Nikon Metrology NV
, Apr 21, 2016. Accessed on Apr 22, 2022. [Online].
Available: https://www.nikonmetrology.com/en-gb/about-us/latest-news/the-hn-c3030-delivers-high-speed,-high-precision,-non-contact-gear-inspection

[29] Gleason, "300GMSL Multi-Sensor Inspection Machine." [Online]. Available:
http://www.gleason.com/en/news/472/300gmsl-multi-sensor-inspection-machine.
https://www.gleason.com/en/facts-and-news/news-room/want-quiet-go-nano-sub-micron-gear-inspection-control-2022

[30] Gear Shape Measurement Potential of Laser Triangulation and Confocal-Chromatic Distance Sensors

[31] G. Goch and K. Luebke, "Tschebyscheff approximation for the calculation of maximum inscribed/minimum circumscribed geometry elements and form deviations," CIRP Annals - Manufacturing Technology, vol. 57, no. 1, pp. 517–520, 2008.

[32] G. Goch, Y. Peng, K. Ni, A. Guenther, "Optical and areal measurement and evaluations of cylindrical gears," In: 17th international VDI congress, Bonn, 2017.

[33] Y. Peng, K. Ni, G. Goch, "Areal evaluation of involute gear flanks with three-dimensional surface data," AGMA FTM, 2017, 15.

[34] A. Hosseinpour, Y. Peng, G. Goch, K. Ni, A. Guenther "Optical gear inspection using a triangulation sensor and an areal evaluation," 35th American Society for Precision Engineering Annual Meeting (ASPE), 2020, 166-169.

APPENDIX A: PEAK DETECTION ALGORITHM OR DERIVATION OF ANALYTICAL DESCRIPTION OF RIDGE LINE

a. Quadratic ridge line- Local coordinate perpendicular to the ridge line

b. Quadratic ridge line- Local coordinate along with the x direction

c. Quadratic ridge line- Local coordinate along with the y direction

d. Elliptical ridge line- Local coordinate along with the y direction

a. Quadratic ridge line and $\xi = x_{loc}$

$$y_c(x) = a_0 + a_1 x_c + a_2 {x_c}^2 \tag{A.a.1}$$

$$\frac{dy_c}{dx_c} = a_1 + 2a_2 x_c \tag{A.a.2}$$

$$\begin{pmatrix} x_{loc} \\ y_{loc} \end{pmatrix} = \begin{pmatrix} \cos\varphi & \sin\varphi \\ -\sin\varphi & \cos\varphi \end{pmatrix} \begin{pmatrix} x - x_c \\ y - y_c \end{pmatrix} \tag{A.a.3}$$

$$I(\xi, x_c, y_c) = b_0(x_c, y_c) - b_2(x_c, y_c)\xi^2 \tag{A.a.4}$$

where y_c is a function of x_c. Since φ can be calculated as having $\frac{dy_c}{dx_c}$ which is known for any point along $y_c(x_c)$, and x_{loc} is equal to ξ, then I($x_c.y_c$) can be calculated.

$$\tan\varphi = \frac{-1}{\frac{dy_c}{dx_c}} \tag{A.a.5}$$

$$\sin\varphi = -\frac{\pm 1}{\sqrt{1 + \frac{dy_c}{dx_c}^2}} \tag{A.a.6}$$

$$\cos\varphi = \frac{\pm\frac{dy}{dx}}{\sqrt{1 + \frac{dy_c}{dx_c}^2}} \tag{A.a.7}$$

$$\cos\varphi = -\frac{dy_c}{dx_c} . \sin\varphi \tag{A.a.8}$$

The straight line perpendicular to the ridge line passing through ($x_c.y_c$) is described by:

$$y - y_c = \tan\varphi\,(x - x_c) \tag{A.a.9}$$

$$y - y_c = \frac{-1}{\frac{dy_c}{dx_c}}(x - x_c) \tag{A.a.10}$$

Using equation $(A.a.3)$, x_{loc} and y_{loc} can be calculated as follows:

$$x_{loc} = (x - x_c)\cos\varphi + (y - y_c)\sin\varphi \ = \ \xi \tag{A.a.11}$$

$$y_{loc} = -(x - x_c)\sin\varphi \ + (y - y_c)\cos\varphi = 0 \tag{A.a.12}$$

From equations $(A.a.5)$, $(A.a.11)$ and $(A.a.12)$, ξ can be found as follows:

$$\xi = \ (x - x_c)\sqrt{1 + \left(\frac{1}{\frac{dy_c}{dx_c}}\right)^2} \tag{A.a.13}$$

It is also assumed that $b_0\ and\ b_2\ are\ const$ants over the ridge line. This means that the intensity peaks along the ridge line and the width of the intensity stripe are both assumed to be constant. Plugging equation $(A.a.13)$ into $(A.a.4)$ gives:

$$I(\xi, x_c, y_c) = b_0 - b_2(x - x_c)^2\left(1 + \left(\frac{1}{\frac{dy_c}{dx_c}}\right)^2\right) \tag{A.a.14}$$

$$I(\xi, x_c, y_c) = b_0 - b_2(x - x_c)^2\left(1 + \left(\frac{1}{a_1 + 2a_2x_c}\right)^2\right) \tag{A.a.15}$$

Equations $(A.a.1)$ and $(A.a.10)$ are combined to remove y_c in equation $(A.a.16)$.

$$y - (a_0 + a_1x_c + a_2{x_c}^2) = \frac{-1}{a_1 + 2a_2x}(x - x_c) \tag{A.a.16}$$

$$\begin{gathered}(x + a_1y - a_1a_0) + (2a_2y - {a_1}^2 - 2a_2a_0 - 1)x_c + (-3a_2a_1){x_c}^2 \\ + (-2{a_2}^2){x_c}^3 = 0\end{gathered} \tag{A.a.17}$$

Considering the known values for x and y which are the locations of any given pixel in the sensor coordinate system, equation $(A.a.17)$ can be solved for x_c.

$$x_c = f(x, y) \tag{A.a.18}$$

Since the x_c is a complicated non-linear function of x and y leading to a highly non-linear deviation function; the other two directions for x_{loc} will be assessed.

b. Quadratic ridge line and $\xi = x_{loc} = x - x_c\ and\ y = y_c$

$$y_c(x) = a_0 + a_1 x_c + a_2 {x_c}^2 \tag{A.b.1}$$

$$(a_0 - y_c) + a_1 x_c + a_2 {x_c}^2 = 0 \tag{A.b.2}$$

$$x_c = \frac{-a_1 \pm \sqrt{{a_1}^2 - 4a_2(a_0 - y_c)}}{2a_2} \tag{A.b.3}$$

$$\begin{pmatrix} x_{loc} \\ y_{loc} \end{pmatrix} = \begin{pmatrix} x - x_c \\ y_c \end{pmatrix} \tag{A.b.4}$$

$$x_{loc} = (x - x_c) = \xi \tag{A.b.5}$$

$$y_{loc} = y_c = y \tag{A.b.6}$$

$$I_a(x, y, x_c, y_c) = b_0 - b_2(x - x_c)^2 \tag{A.b.7}$$

$$I_a(x, y) = b_0 - b_2\left(x - \left(\frac{-a_1 \pm \sqrt{{a_1}^2 - 4a_2(a_0 - y)}}{2a_2}\right)\right)^2 \tag{A.b.8}$$

$$\text{Solution: } \vec{s} = (a_0, a_1, a_2, b_0, b_2\ ) \tag{A.b.9}$$

$$\text{coefficient change: } \overrightarrow{\Delta s} = (\Delta a_0, \Delta a_1, \Delta a_2, \Delta b_0, \Delta b_2\ ) \tag{A.b.10}$$

$$\text{Distance definition: } d_i = I_i(s_j + \Delta s_j) - I_{m,i} \tag{A.b.11}$$

$$\begin{aligned} d_i = {} & \left(b_0 + \Delta b_0 - I_{m,i}\right) - (b_2 + \Delta b_2). \\ & .\left(x_i - \left(\frac{-(a_1 + \Delta a_1) \pm \sqrt{(a_1 + \Delta a_1)^2 - 4(a_2 + \Delta a_2)(a_0 + \Delta a_0 - y_i)}}{2(a_2 + \Delta a_2)}\right)\right)^2 \end{aligned} \tag{A.b.12}$$

$$Q = \sqrt{\textstyle\sum_{i=1}^{n} {d_i}^2} \tag{A.b.13}$$

$$\sum\nolimits_{i=1}^{n} \left(d_i \frac{\partial d_i}{\partial \Delta s_j}\right) = 0 \tag{A.b.14}$$

$$\begin{aligned} & \sum\nolimits_{i=1}^{n} \left(\begin{array}{c} \left(b_0 + \Delta b_0 - I_{m,i}\right) - (b_2 + \Delta b_2). \\ \left(x_i - \left(\frac{-(a_1 + \Delta a_1) \pm \sqrt{(a_1 + \Delta a_1)^2 - 4(a_2 + \Delta a_2)(a_0 + \Delta a_0 - y_i)}}{2(a_2 + \Delta a_2)}\right)\right)^2 \dfrac{\partial d_i}{\partial \Delta s_j} \end{array} \right) \\ & = 0 \end{aligned} \tag{A.b.15}$$

Since equation $(A.b.15)$ leads to an extremely complicated non-linear equation in terms of Δs_j the last direction is going to be assessed.

c. Quadratic ridge line and $\xi = y_{loc} = y - y_c$ *and* $x = x_c$

It is assumed that the ridge line $y_c(x)$ of the intensity distribution in the X-Y plane is known as a starting solution, i.e., a smooth line following the peaks of the distribution.

$$y_c(x) = a_0 + a_1 x_c + a_2 {x_c}^2 \qquad (\mathrm{A.c.1})$$

$$\begin{pmatrix} x_{loc} \\ y_{loc} \end{pmatrix} = \begin{pmatrix} x_c \\ y - y_c \end{pmatrix} \qquad (\mathrm{A.c.2})$$

$$x_{loc} = (x_c) = \xi \qquad (\mathrm{A.c.3})$$

$$y_{loc} = y - y_c \qquad (\mathrm{A.c.4})$$

$$I_a(x, y, x_c, y_c) = b_0 - b_2(y - y_c)^2 \qquad (\mathrm{A.c.5})$$

Plugging equation $(A.c.1)$ into $(A.c.5)$, the analytical solution for the intensity of any arbitrary point (x, y) is found as $I_a(x, y)$.

$$I_a(x, y) = b_0 - b_2(y - (a_0 + a_1 x + a_2 x^2))^2 \qquad (\mathrm{A.c.6})$$

The sum of the squares of the residuals between the measured and the model-based intensity (I_m and I_a respectively) for all the sensor pixels is called the objective function (Q). This objective function needs to be a minimum to find the best approximation for I_a. To do so, the intensity function should be written in terms of $a_j + \Delta a_j$ and $b_j + \Delta b_j$. Then, Q should be iteratively minimized with respect to the five variable deviations $\Delta a_j and\ \Delta b_j$ (Δs_j) [3].

$$\text{Distance definition: } d_i = I_{a,i}(s_j + \Delta s_j) - I_{m,i} \qquad (\mathrm{A.c.7})$$

$$\begin{gathered} d_{i,k} = \left(b_{0,k-1} + \Delta b_{0,k} - I_{m,i}\right) - \left(b_{2,k-1} + \Delta b_{2,k}\right). \\ \left(y_i - \left(a_{0,k-1} + \Delta a_{0,k} + (a_{1,k-1} + \Delta a_{1,k})x_i + \left(a_{2,k-1} + \Delta a_{2,k}\right){x_i}^2\right)^2 \end{gathered} \qquad (\mathrm{A.c.8})$$

In equation $(A.c.8)$, *i* denotes the point number and k denotes the number of iterations.

$$\text{Objective function: } Q_k = \sqrt{\sum_{i=1}^{n} {d_{i,k}}^2} \qquad (\mathrm{A.c.9})$$

$$\text{Initial solution: } \vec{s_0} = \left(a_{0,0}, a_{1,0}, a_{2,0}, b_{0,0}, b_{2,0}\right) \qquad (\mathrm{A.c.10})$$

$$\text{Initial change: } \overrightarrow{\Delta s_0} = \left(\Delta a_{0,0}, \Delta a_{1,0}, \Delta a_{2,0}, \Delta b_{0,0}, \Delta b_{2,0}\right) \qquad (\mathrm{A.c.11})$$

An initial solution $s_{j,0}$ is needed to start the iterations. One approach to finding the initial solution which is used in this work is to find the positions of the arrays with max intensities in X-Y sensor coordinate and find a quadratic polynomial regression to find the initial ridge line coefficients $(a_{0,0}, a_{1,0}, a_{2,0})$ for each sensor frame. Then the 1st nonzero-intensity row of the same sensor frame is used to find the initial coefficients $(b_{0,0}, b_{2,0})$ for the quadratic intensity distribution using another quadratic polynomial regression. Considering the coefficient changes for the initial solution labeled as $\Delta s_{j,0}$, the initial solution can be improved and used as the first solution for the next iteration.

$$Q_{min} \rightarrow \frac{\partial Q_0}{\partial \Delta s_{j,0}} = 0, \quad \begin{cases} \frac{\partial Q_0}{\partial \Delta a_{0,0}} = 0 \\ \frac{\partial Q_0}{\partial \Delta a_{1,0}} = 0 \\ \frac{\partial Q_0}{\partial \Delta a_{2,0}} = 0 \\ \frac{\partial Q_0}{\partial \Delta b_{0,0}} = 0 \\ \frac{\partial Q_k}{\partial \Delta b_{2,0}} = 0 \end{cases} \rightarrow \begin{cases} \frac{1}{2\sqrt{\sum_{i=1}^{n} {d_{i,0}}^2}} \sum_{i=1}^{n} \left(2d_{i,0} \frac{\partial d_{i,0}}{\partial \Delta a_{0,0}}\right) = 0 \\ \frac{1}{2\sqrt{\sum_{i=1}^{n} {d_{i,0}}^2}} \sum_{i=1}^{n} \left(2d_{i,0} \frac{\partial d_{i,0}}{\partial \Delta a_{1,0}}\right) = 0 \\ \frac{1}{2\sqrt{\sum_{i=1}^{n} {d_{i,0}}^2}} \sum_{i=1}^{n} \left(2d_{i,0} \frac{\partial d_{i,0}}{\partial \Delta a_{2,0}}\right) = 0 \\ \frac{1}{2\sqrt{\sum_{i=1}^{n} {d_{i,0}}^2}} \sum_{i=1}^{n} \left(2d_{i,0} \frac{\partial d_{i,0}}{\partial \Delta b_{0,0}}\right) = 0 \\ \frac{1}{2\sqrt{\sum_{i=1}^{n} {d_{i,0}}^2}} \sum_{i=1}^{n} \left(2d_{i,0} \frac{\partial d_{i,0}}{\partial \Delta b_{2,0}}\right) = 0 \end{cases} \qquad (\mathrm{A.c.12})$$

The square roots in the denominators of the five equations in $(A.c.12)$ must be positive and different from zero in the non-trivial case. Therefore, only the numerators in equation $(A.c.12)$ must be considered. However, the term in the nominator, $d_{i,0}\frac{\partial d_{i,0}}{\partial \Delta s_{j,0}}$, which is highly non-linear, should be linearized to end up with a system of five linear equations.

$$\begin{aligned} f_{1,0} &= \sum_{i=1}^{n} \left(d_{i,0} \frac{\partial d_{i,0}}{\partial \Delta a_{0,0}}\right) \rightarrow g_{1,0}\text{: } linearized\ f_{1,0}\ with\ respect\ to\ \Delta s_{1,0} \\ f_{2,0} &= \sum_{i=1}^{n} \left(d_{i,0} \frac{\partial d_{i,0}}{\partial \Delta a_{1,0}}\right) \rightarrow g_{2,0}\text{: } linearized\ f_{2,0}\ with\ respect\ to\ \Delta s_{2,0} \\ f_{3,0} &= \sum_{i=1}^{n} \left(d_{i,0} \frac{\partial d_{i,0}}{\partial \Delta a_{2,0}}\right) \rightarrow g_{3,0}\text{: } linearized\ f_{3,0}\ with\ respect\ to\ \Delta s_{3,0} \\ f_{4,0} &= \sum_{i=1}^{n} \left(d_{i,0} \frac{\partial d_{i,0}}{\partial \Delta b_{0,0}}\right) \rightarrow g_{4,0}\text{: } linearized\ f_{4,0}\ with\ respect\ to\ \Delta s_{4,0} \\ f_{5,0} &= \sum_{i=1}^{n} \left(d_{i,0} \frac{\partial d_{i,0}}{\partial \Delta b_{2,0}}\right) \rightarrow g_{5,0}\text{: } linearized\ f_{5,0}\ with\ respect\ to\ \Delta s_{5,0} \end{aligned} \qquad (\mathrm{A.c.13})$$

After calculations for all the coefficient changes ($\overrightarrow{\Delta s} = (\Delta a_0, \Delta a_1, \Delta a_2, \Delta b_0, \Delta b_2\ )$) the following set of five linear equations is obtained, where superscript 1 refers to iteration 1.

$$[A]^1[\Delta s]^1 = [B]^1 \text{ or } \begin{bmatrix} A_{11}A_{12}A_{13}A_{14}A_{15} \\ A_{21}A_{22}A_{23}A_{24}A_{25} \\ A_{31}A_{32}A_{33}A_{34}A_{35} \\ A_{41}A_{42}A_{43}A_{44}A_{45} \\ A_{51}A_{52}A_{53}A_{54}A_{55} \end{bmatrix}^1 . \begin{bmatrix} \Delta a_0 \\ \Delta a_1 \\ \Delta a_2 \\ \Delta b_0 \\ \Delta b_2 \end{bmatrix}^1 = \begin{bmatrix} B_1 \\ B_2 \\ B_3 \\ B_4 \\ B_5 \end{bmatrix}^1 \tag{A.c.14}$$

in which:

$$M_i = -y_i + a_0 + a_1 x_i + a_2 {x_i}^2 \tag{A.c.15}$$

$$N_i = I_{m,i} - (b_0 - b_2 {M_i}^2) \tag{A.c.16}$$

$$A_{11} = \sum_{i=1}^{n}({b_2}^2 (2M_i)^2 + 2b_2 N_i) \tag{A.c.17}$$

$$A_{12} = A_{21} = \sum_{i=1}^{n} x_i({b_2}^2 (2M_i)^2 + 2b_2 N_i) \tag{A.c.18}$$

$$A_{13} = A_{31} = \sum_{i=1}^{n} {x_i}^2({b_2}^2 (2M_i)^2 + 2b_2 N_i) \tag{A.c.19}$$

$$A_{14} = A_{41} = \sum_{i=1}^{n}(-2b_2 M_i) \tag{A.c.20}$$

$$A_{15} = A_{51} = \sum_{i=1}^{n} 2M_i(I_{m,i} - b_0 + 2b_2\, {M_i}^2) \tag{A.c.21}$$

$$B_1 = \sum_{i=1}^{n}(-2b_2 M_i N_i) \tag{A.c.22}$$

$$A_{22} = \sum_{i=1}^{n} {x_i}^2({b_2}^2 (2M_i)^2 + 2b_2 N_i) \tag{A.c.23}$$

$$A_{23} = A_{32} = \sum_{i=1}^{n} {x_i}^3({b_2}^2 (2M_i)^2 + 2b_2 N_i) \tag{A.c.24}$$

$$A_{24} = A_{42} = \sum_{i=1}^{n} x_i(-2b_2 M_i) \tag{A.c.25}$$

$$A_{25} = A_{52} = \sum_{i=1}^{n} 2M_i x_i(N_i + b_2\, {M_i}^2) \tag{A.c.26}$$

$$B_2 = \sum_{i=1}^{n} x_i(-2b_2 M_i N_i) \tag{A.c.27}$$

$$A_{33} = \sum_{i=1}^{n} {x_i}^4({b_2}^2 (2M_i)^2 + 2b_2 N_i) \tag{A.c.28}$$

$$A_{34} = A_{43} = \sum_{i=1}^{n} {x_i}^2(-2b_2 M_i) \tag{A.c.29}$$

$$A_{35} = A_{53} = \sum_{i=1}^{n} 2M_i {x_i}^2(N_i + b_2\, {M_i}^2) \tag{A.c.30}$$

$$B_3 = \sum_{i=1}^{n} {x_i}^2(-2b_2 M_i N_i) \tag{A.c.31}$$

$$A_{44} = \sum_{i=1}^{n} 1 = n \tag{A.c.32}$$

$$A_{45} = A_{54} = \sum_{i=1}^{n} -{M_i}^2 \tag{A.c.33}$$

$$B_4 = \sum_{i=1}^{n} N_i \tag{A.c.34}$$

$$A_{55} = \sum_{i=1}^{n} {M_i}^4 \qquad (\mathrm{A.c.35})$$

$$B_5 = \sum_{i=1}^{n} -N_i {M_i}^2 \qquad (\mathrm{A.c.36})$$

Solving the set of 5 linear equations, all five coefficient changes can be calculated at each iteration.

$$[\Delta s]^1 = [[A]^1]^{-1}[B]^1 \rightarrow \overrightarrow{s_1} = \overrightarrow{s_0} + \overrightarrow{\Delta s_1} \qquad (\mathrm{A.c.37})$$

The new solution at each iteration $\overrightarrow{s_k}$ should be used to reduce the objective function Q_k to eventually find the minimum Q. Then I_a as the best solution describes the intensity distribution can be found, and consequently, the ridge line can be achieved using already calculated a_i coefficients.

d. Elliptical ridge line and $\xi = y_{loc} = y - y_c \; and \; x = x_c$

$$y_c(x) = y_0 + B\sqrt{1 - \left(\frac{x_c - x_0}{A}\right)^2} \qquad (\mathrm{A.d.1})$$

$$\begin{pmatrix} x_{loc} \\ y_{loc} \end{pmatrix} = \begin{pmatrix} x_c \\ y - y_c \end{pmatrix} \qquad (\mathrm{A.d.2})$$

$$x_{loc} = (x_c) = \xi \qquad (\mathrm{A.d.3})$$

$$y_{loc} = y - y_c \qquad (\mathrm{A.d.4})$$

$$I_a(x, y, x_c, y_c) = b_0 - b_2\left(y - y_0 - B\sqrt{1 - \left(\frac{x_c - x_0}{A}\right)^2}\right)^2 \qquad (\mathrm{A.d.5})$$

$$d_i = I_i(s_j) - I_{m,i} \qquad (\mathrm{A.d.6})$$

$$d_{i,k} = (b_{0,k-1} - I_{m,i}) - (b_{2,k-1})\left(y_i - y_{0,k-1} - B_{k-1}\sqrt{1 - \left(\frac{x_{c,k-1} - x_{0,k-1}}{A_{k-1}}\right)^2}\right)^2 \qquad (\mathrm{A.d.7})$$

$$\text{Objective function: } Q_k = \sqrt{\sum_{i=1}^{n} {d_{i,k}}^2} \qquad (\mathrm{A.d.8})$$